Local Dynamics and Atomic-level Structures in Metallic Liquids and Glasses

A Dissertation Presented for the

Doctor of Philosophy

Degree

The University of Tennessee, Knoxville

Zengquan Wang

May 2021

Dedication

To my wife, parents, sisters, and grandparents,

for their love, support, and inspiration.

Acknowledgements

First and foremost, I would like to thank my adviser, Dr. Takeshi Egami, and co-advisor, Dr. Wojciech Dmowski, for their invaluable guidance and instruction on the research, and generous care and support in the life during my Ph.D. candidacy in a foreign country. Their great wisdom, passion, perseverance, and motivation to explore new knowledge will always inspire and lead me through the difficulties in my life and career and will be always cherished in the future. I would also like to thank my committee members, Dr. Yanfei Gao and Dr. Cristian Batista, for their valuable time and instruction.

This work could not have been done without the great help of many people. I am sincerely grateful to many beamline specialists at the Spallation Neutron Source and the Advanced Photon Source for their assistance with the experiments, especially Dr. Douglas Abernathy at the ARCS beamline. Many thanks also go to my previous and current colleagues, Dr. Yang Tong, Dr. Takuya Iwashita, Dr. Bin Wu, Dr. Chae Woo Ryu, Dr. Yuya Shinohara, Mr. Yadu Sarathchandran and Mr. Leo Zella, and my collaborators, Dr. Adam Vogt, Dr. Dante Quirinale, Dr. Robert Ashcraft, and Dr. Kenneth Kelton for the meaningful discussions and help during the beamline experiments. Without their efforts, the experiments and thus this dissertation cannot be finished.

Last but not least, I thank my wife and colleague, Dr. Hui Wang, for her countless assistance, support and love. Without her, I cannot imagine how I could have overcome all the difficulties and frustrations in my life and research. Same gratitude also goes to my parents and sisters for their continuous support and love.

Abstract

Structure and dynamics at the atomic level in metallic glasses and liquids are poorly understood when compared to the crystalline solids. For instance, even though viscosity is the basic property of liquids, its atomistic origin is not well elucidated. Also, the physics of the fragility of liquids and the crossover phenomenon is far from full understanding. Earlier, through molecular dynamics (MD) simulations a direct connection was found between the timescale describing the macroscopic viscous behavior, the Maxwell relaxation time ($\tau_M = \eta/G_\infty$, η is the shear viscosity and G_∞ is the high-frequency shear modulus) and the timescale of microscopic atomic behavior, τ_{LC}, which is the time for an atom to lose or gain one nearest neighbor by cutting or creating a bond.

To verify this relationship experimentally and further the study of dynamics of liquid metals, we carried out the inelastic neutron scattering (INS) experiments at ARCS beamline at the Spallation Neutron Source (SNS) on metallic liquid droplets of $Zr_{50}Cu_{50}$ and $Zr_{80}Pt_{20}$, using an electro-static levitator (NESL), which provided a high vacuum containerless environment. This was the first experiment of this kind allowing us to determine the dynamic structure function $S(Q,E)$ over a large Q-E space with high statistics and low backgrounds. Time dependent Van Hove correlation function $G(r, t)$, including the self and the distinct part, was obtained with high reliability through a double Fourier transformation using the developed data analysis procedure and codes. Atomic-level relaxation times and diffusivity were determined by analyzing the time dependence of the $G(r, t)$ peak features, and were compared with the results of viscosity measurements and MD simulations. This research experimentally verifies conclusion of the previous MD simulation that viscosity is controlled by the local atomic connectivity change in metallic liquids above the crossover temperature T_A. Using the experimental and data processing

procedures developed by us, significant progress is made in the elucidation of local atomic dynamics in metallic liquids.

In addition, the thermal structural evolution of two Zr-based metallic glasses were studied by in-situ high energy X-ray diffraction experiment and MD simulations with the pair distribution function (PDF) analysis. The different phase transition behavior and thermal atomic structural evolution for $Zr_{65}Cu_{17}Ni_8Al_{10}$ and $Zr_{80}Pt_{20}$ are observed and attributed to the different topological and chemical effects of different atomic pairs.

Table of Contents

List of Tables

List of Figures

Chapter 1 Introduction

Amorphous matters, including glasses and liquids, are ubiquitous in the nature. Actually, they are more widespread than the crystalline materials which are just special cases of condensed matters, considering that water and earth mantle are both amorphous. However, the modern condensed matter physics is mainly focused on crystalline solids. The science of liquids and glasses is significantly underdeveloped when compared to that of crystalline solids[1].

Glasses and liquids are very complex many-body systems. The lack of the translational and rotational symmetry makes it difficult to use standard solid state physics methods to elucidate and understand their structure and dynamics. For example, viscosity is the most well-known and fundamental property of liquid, however, its atomic origin is still not well understood, and the nature of glass transition still remains a mysterious, complex and unanswered question of the 21st century, although much attention has been drawn to study them.[2-5].

Currently, the research on the structure and dynamics of the liquids is mainly focused on the supercooled liquid and glass transition regions[5-7]. For a long time, the high-temperature behavior of liquids has not been considered important due to perceived notion that high temperature liquid can be treated as a gas-like free motion. However, this is oversimplification since atoms in high-temperature liquids are still confined and strongly interacted with each other. The atomic density is high and similar to lower-temperature liquids, and atomic motions in the high-temperature liquids are still thermally activated. The structures of liquids and glasses are usually inherited from the high-temperature liquid, and the change in the instantaneous structure is very small. On the other hand, dynamics on the atomic scale determines the physical properties of liquids as well as the solidification and freezing behavior of metallic melts. The dynamics is

also of special importance for understanding the glass-forming ability and the nature of glass transition. Thus, we believe that structures and dynamics in high-temperature liquids are interesting topics to explore and have great scientific importance.

In this Dissertation:

A brief introduction of the metallic glasses and liquids, including the research backgrounds on viscosity, glass transition, and diffusion behavior will be reviewed in Chapter 2. The definition and importance of Van Hove function will also be introduced in this chapter.

Chapter 3 will present the experimental setups for the inelastic neutron scattering (INS) and high-energy X-ray diffraction. The techniques of inelastic neutron scattering, and Van Hove function will also be covered. Then the procedure and algorithm of calculating the Van Hove function from INS data will be presented in detail.

In Chapter 4, the local dynamics in the high temperature liquids of $Zr_{50}Cu_{50}$ and $Zr_{80}Pt_{20}$ will be analyzed based on the relaxation behavior of the first peak of distinct part of the Van Hove function. Also, the diffusion behavior of the metallic liquids will be discussed from the analysis of the self-part of the Van Hove function.

In situ high energy X-ray diffraction experiment and MD simulations for two Zr-based metallic glasses will be described in Chapter 5. The different phase transition behavior and thermal atomic structural evolution for $Zr_{65}Cu_{17}Ni_8Al_{10}$ and $Zr_{80}Pt_{20}$ are observed and attributed to the different topological and chemical effects of different atomic pairs.

Conclusions and potential questions in the course of this work are addressed in the Chapter 6.

Chapter 2 Literature Review

In addition to structure and thermodynamics, the dynamic behavior is also an important topic in the research of liquids. In this chapter, advances in several aspects of the liquid dynamics will be presented. First, the famous Angell plot, the kinetic fragility and the crossover phenomenon in liquids will be introduced. Then, the investigation of diffusion behavior in glass-forming metallic liquids will be discussed. Also, the progress in understanding the nature of shear viscosity and the crossover phenomenon based on the molecular dynamics (MD) simulation from our research group will be showed. The concept of Van Hove function and its recent development and advantages in analyzing the atomic-level dynamics in the current research will be enumerated. Finally, the unresolved problems and open questions that are resolved by this research will be presented.

2.1 Fragility of liquids and the crossover phenomenon

The concept of fragility of liquids was first proposed by C. A. Angell in order to universally describe the behavior of viscosity in liquids [8-10]. As shown in the typical Angell plot (as shown in Figure 2.1), the logarithm of shear viscosity is plotted against the reduced inverse temperature, T_g/T, where T_g is glass transition temperature at which viscosity reaches 10^{12} Pa·s. The kinetic fragility index of liquids is defined as

$$m = \left.\frac{\partial \log(\eta)}{\partial (T_g / T)}\right|_{T=T_g}, \tag{2.1}$$

where η is the shear viscosity. It is the slope of the viscosity curve in log scale at $T=T_g$ and describes how much the viscosity of the liquid deviates from the Arrhenius behavior. This parameter classifies the liquids in a scale from ‘strong’ to ‘fragile’. When m value is small, the liquid is strong

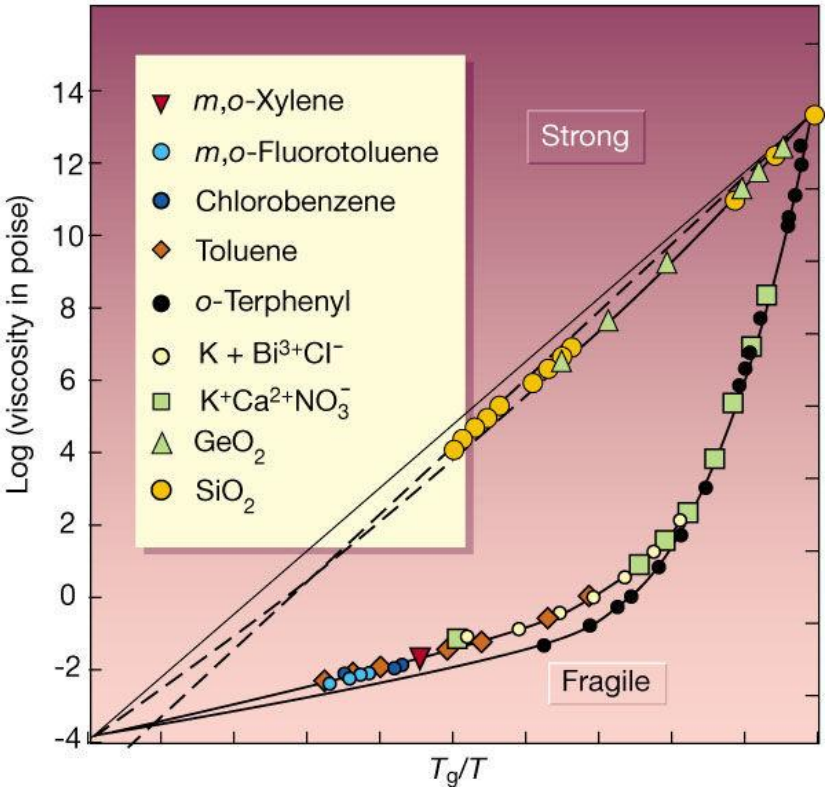

Figure 2.1 Typical Angell plot showing the logarithm of the viscosity as a function of reduced inverse temperature T_g/T.[11]

and nearly shows an Arrhenius behavior, while when *m* value is large, the liquid is fragile and shows significant deviation from the Arrhenius behavior. Network-forming liquids, such as silica (SiO_2), are usually the typical strong liquids, whereas molecular liquids, such as o-terphenyl (OTP), are the fragile glass-forming liquids. Most metallic glass-forming liquids are in between these two extremes and are relatively fragile. The fragile liquids show thermally activated Arrhenius behavior at high temperatures approaching to the infinite temperature but show super-Arrhenius behavior when the temperature is approaching the glass transition[3, 6, 12]. This transition of viscosity from Arrhenius to super-Arrhenius behavior is the so-called crossover phenomenon in liquids, and the vague transition temperature is called the crossover temperature, T_A. However, the physical nature of the crossover phenomenon and fragility remain unclear[13-15].

A distinct correlation between the fragility and crossover temperature for various liquids has been reported[16]. In particular, for glass-forming metallic liquids, the crossover temperature $T_A \approx 2T_g$, while the crossover occurs at about $1.4T_g$ for fragile molecular liquids. For different strong network-forming liquids, the crossover occurs at a wide temperature range above $2T_g$, as shown in Figure 2.2. The crossover temperature has been interpreted as the onset point of cooperative motions of particles and hence the slowdown of dynamics during cooling for various liquid systems including molecular liquids and multicomponent metallic liquids[10, 17-19].

In the Angell plot, the value of viscosity, η, at the glass transition temperature, Tg, is the same for all liquids, 10^{13} poise (or 10^{12} Pa·s), by definition. On the other hand, the viscosity amazingly converge to about 10^{-4} poise (or 10^{-5} Pa·s) at infinite temperature for any liquid systems[10]. The reason of this universal convergence is still unknown. However, this convergence and the Arrhenius behavior above T_A shows that the high-temperature behavior of liquids is interesting and deserve much more attention than it currently has.

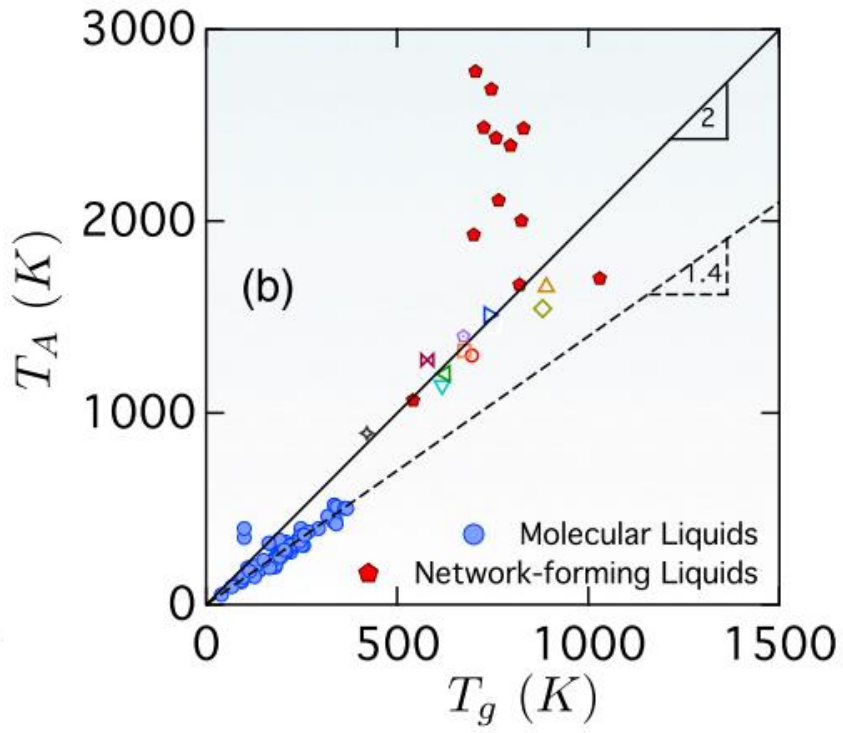

Figure 2.2 Correlation of the Arrhenius crossover temperature T_A with the glass transition temperature Tg for various liquid systems[16].

We believe that the exploration of the dynamic behavior of liquid around or above the crossover temperature will not only be beneficial to the understanding of high-temperature liquid itself, but also will help to understand the nature of glass transition and viscosity. Meanwhile, currently the research in liquids, especially glass-forming liquids, is mainly focused on the supercooled liquid or glass states to understand the behavior in these temperature ranges, as shown in Figure 2.3[20, 21]. It has been proposed that atoms have gas-like free diffusion behavior at high temperatures and thus this range is not scientifically interesting. This is not correct since atoms in high-temperature liquid are still highly confined due to the high atomic density and atomic motions in the high-temperature liquids are still thermally activated. Sometimes it is assumed that the phonon theory still works for the high-temperature metallic liquids, which is not likely since phonons are highly damped and heavily localized within the atomic shell distance at high temperature and cannot interact with each other.[22].

2.2 Diffusion behavior in metallic liquids

Diffusion is another important aspect in the dynamic behaviors of liquids[23]. According to Stokes-Einstein relationship, the diffusivity, D, and viscosity, η, are closely related to each other in the liquids, following the equation:

$$D = \frac{k_B T}{6\pi\eta r}. \tag{2.2}$$

However, for metallic systems, diffusivity is not easy to measure except for certain pure-metal diffusion couples. Commonly, the quasi-elastic neutron scattering (QENS) method is used to determine the self-diffusivity [24-30]. Usually, the low Q incoherent scattering is measured, and Lorentzian curve is used to fit the QENS peaks to obtain the full width at half maximum, Γ. Then the self-diffusivity is determined using the $\Gamma = 2\hbar DQ^2$ relationship, as shown in Figure 2.4.

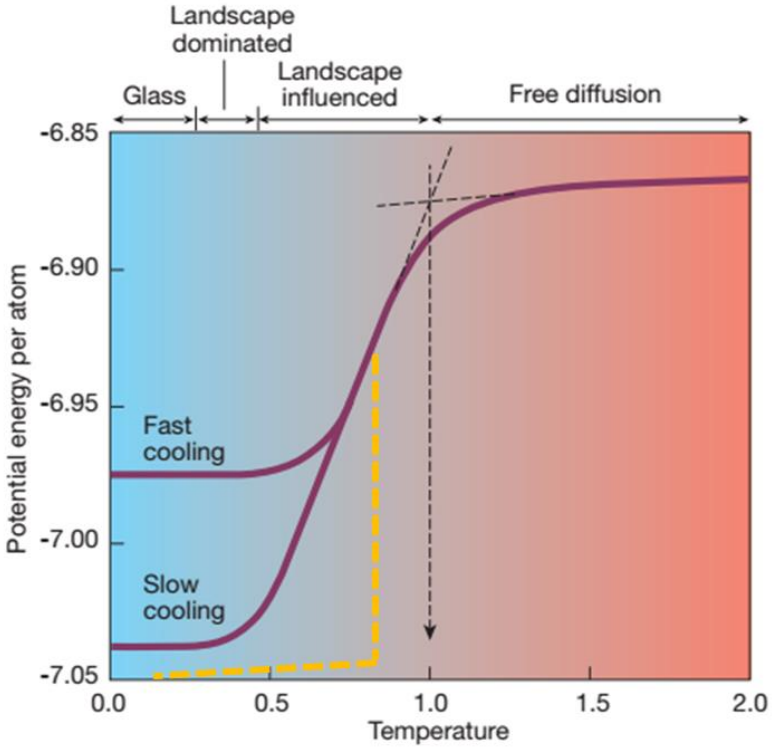

Figure 2.3 Mean inherent structure energy as a function of the temperature of the equilibrated liquid[11]. Many researchers incorrectly assume that atoms in high-temperature liquids only have gas-like free-diffusion motion.

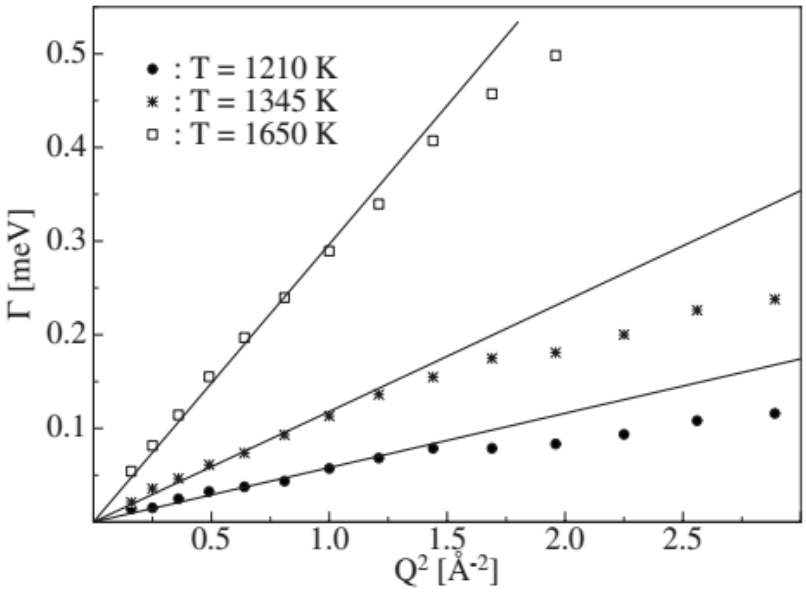

Figure 2.4 Full width at half maximum, Γ, of the Lorentzian fitting of low-Q incoherent scattering peak measured by QENS, plotted as a function of Q^2, for the liquid $Ni_{36}Zr_{64}$ at different temperatures[25].

However, this method has great limitations as it depends on measuring the incoherent neutron scattering at low Q values. Thus, only a few elements with significant incoherent scattering length/cross section, such as Ni, can be measured reliably through this method. Most elements that have quite small incoherent scattering length/cross section or large ratio of coherent scattering to incoherent scattering[31] are not suitable for this method. Later in this work, it will be showed that a new method using the self-part of Van Hove function, $G_s(r, t)$, to estimate the diffusivity could be applied much more widely to many metallic elements in liquid alloy systems.

2.3 The nature of viscosity

The atomistic origin of the viscous behavior is still not well elucidated, although it is the most well-known property of liquids. The shear viscosity η is a key parameter describing the macroscopic dynamics and transport property of liquids. It can be calculated by the Green-Kubo relation using molecular dynamics (MD) simulation[32]:

$$\eta = \frac{V}{k_B T}\int_0^\infty \left\langle \sigma_{xy}(0)\sigma_{xy}(t)\right\rangle dt \ , \tag{2.3}$$

where σ_{xy} is x-y component of the stress tensor, k_B is the Boltzmann constant, V is the volume of the system, T is the temperature and <·> means the thermal averaging over all choices of t = 0. The time scale to describe the macroscopic shear viscous behavior is the Maxwell relaxation time, defined asτ

$$\tau_M = \frac{\eta}{G_\infty} , \tag{2.4}$$

where G_∞ is the high-frequency shear modulus[32].

Recently, a significant progress in understanding the nature of viscosity and the dynamics in high-temperature metallic liquids through MD simulation was made by Egami's research group[1,

33, 34]. A direct connection was found between the timescale to describe the macroscopic viscous behavior, the Maxwell relaxation time, τ_M, and the timescale of a microscopic behavior, τ_{LC}. The τ_{LC} is the lifetime of a local connectivity change, the time for an atom to lose or gain one nearest neighbor by cutting or recreating a bond (as shown in Figure 2.5). The results (as shown in Figure 2.6) show that at high temperatures above the crossover temperature, T_A, τ_M is equal to τ_{LC}, for several different metallic liquid systems. This means that the physical mechanisms in the macroscopic viscous behavior and in the microscopic local connectivity change are the same above T_A. When the temperature is below T_A they are no longer equal ($\tau_M > \tau_{LC}$). This implies that viscosity is controlled by local connectivity change at high temperatures and that the local connectivity change is the elementary excitation in high-temperature liquids. The deviation from equality between τ_M and τ_{LC} below T_A is due to the phonon delocalization.

2.4 The Van Hove function

The Van Hove function (VHF) concept was proposed in 1954[35]. By definition, it is the probability to find one particle at position *r* and time *t*, given that there was a particle at the origin and time *t*=0. Theoretically, it can be calculated through

$$G(r,t) = \frac{1}{4\pi r^2 \rho_0 N} \left\langle \sum_{i,j=1}^{N} \delta\left(\mathbf{r} - \left|\mathbf{r}_i(t) - \mathbf{r}_j(0)\right|\right) \right\rangle, \tag{2.5}$$

where <·> means the thermal averaging over all possible choices of $t = 0$.When $i = j$, it is the self-part, $G_s(r, t)$, and it describes the self-diffusion behavior of single atom. When $i \neq j$, it is the distinct part, $G_d(r, t)$, and it describes the collective motion or cross correlation between atoms.

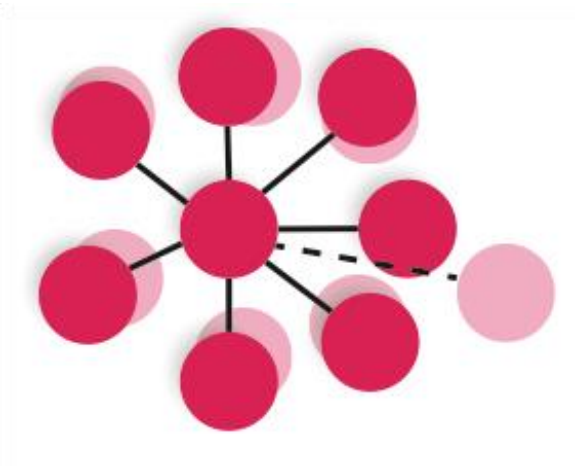

Figure 2.5 Change in the local atomic connectivity by losing or gaining one nearest neighbor defines the local connectivity change time, τ_{LC}.

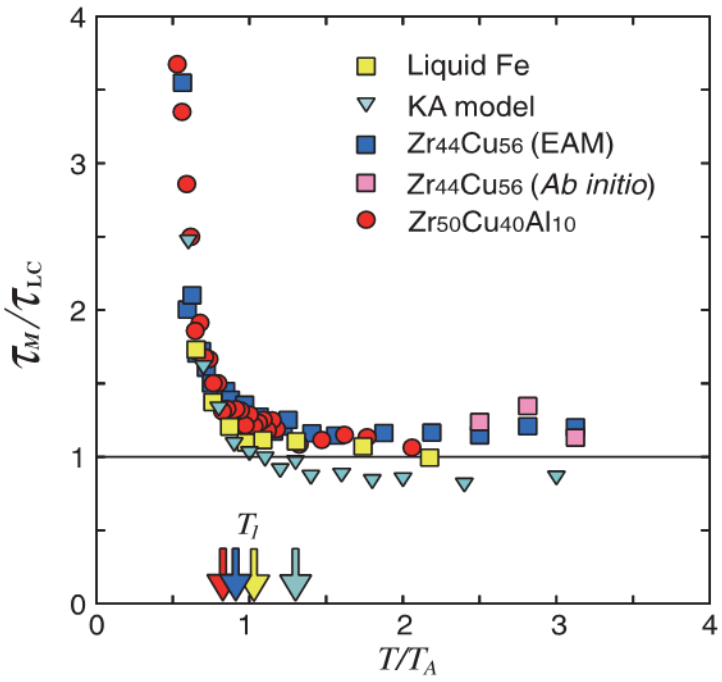

Figure 2.6 The ratio of τ_M/τ_{LC}, plotted against T/T_A for various metallic liquid systems in MD simulation. τ_M is approximately equal to τ_{LC} Above T_A.[33]

Compared with the static/instantaneous pair distribution function (PDF) which describe the "snapshot" structure of the system (like a picture), the Van Hove function can be considered as the time-dependent dynamic pair correlation function of the system (like a movie). When time goes to 0, its self and distinct parts can be reduced to

$$\begin{aligned} G_s(r,0) &\to \frac{1}{\rho}\delta(r) \\ G_d(r,0) &\to g(r) \end{aligned} . \tag{2.6}$$

Unlike that the structure function, $S(Q)$, the dynamic structure function, $S(Q, E)$, and the intermediate scattering function, $F(Q, t)$ are defined in the reciprocal space, the pair distribution function, $g(r)$, and the Van Hove function, $G(r, t)$, are defined in real space and/or real time, providing a more explicit and realistic method to analyze the structure and dynamics of the system[36, 37].

Even though the Van Hove function has been known for a long time, its experimental determination was always difficult as obtaining $S(Q, E)$ with large Q and E coverage, high statistics, and low background from neutron/X-ray scattering experiments was nearly impossible, hence only conceptual and tentative attempts were made. Therefore, analysis of dynamic relaxation based on accurate and reliable Van Hove function was unfeasible[38-41]. Most research using the Van Hove function was from computational simulations and was focusing on the self-part and self-diffusive behavior (as shown in Figure 2.7)[42, 43]

The mean-squared displacement (MSD) of particles in a liquid is a parameter to measure the average distance traveled by a particle during a time period in the system. Its computational implementation involves the averaging of particle displacements over all particles of interest between two time points and is related to the second moment of the self Van Hove function by[32]

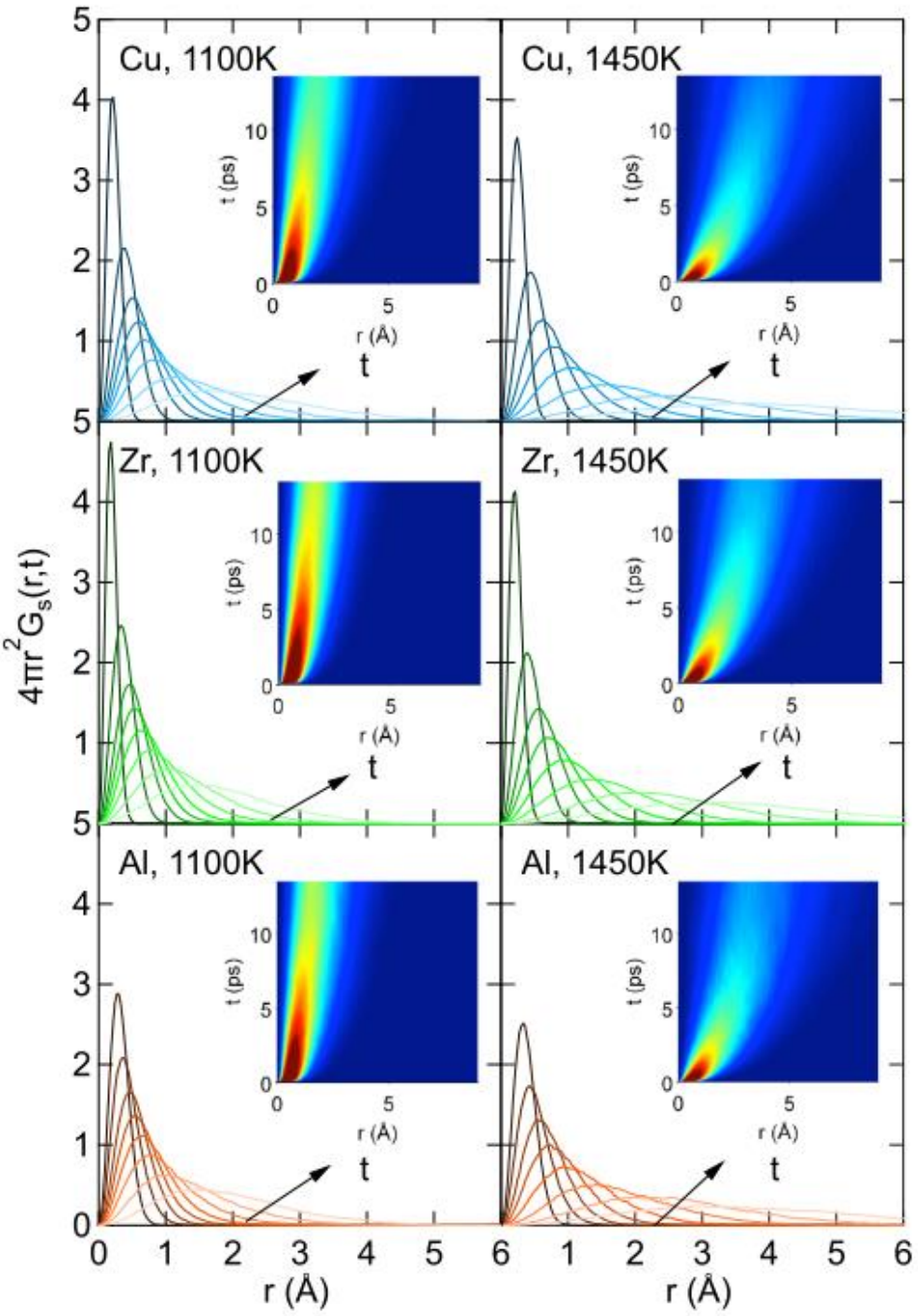

Figure 2.7 Self VHF, $G_s(r, t)$, obtained from MD simulation to analyze the atomic diffusion for a Zr-Cu-Al system [42].

$$\left\langle r^2(t)\right\rangle = \frac{1}{N}\left\langle \sum_{i=1}^{N} \left|\mathbf{r}_i(t) - \mathbf{r}_i(0)\right|^2 \right\rangle = \int r^2 G_s(\mathbf{r},t) d\mathbf{r}\,, \tag{2.7}$$

where <·> means the thermal averaging over all choices of $t = 0$. Then the self-diffusion coefficient can be calculated from the MSD of the simulated system by

$$D = \lim_{t\to\infty} \frac{1}{6t}\left\langle \left|\mathbf{r}_i(t) - \mathbf{r}_i(0)\right|^2 \right\rangle = \lim_{t\to\infty} \frac{1}{6t}\left\langle r^2(t)\right\rangle. \tag{2.8}$$

Only recently with the development of the inelastic neutron/X-ray scattering instrumentations, such as powerful spallation neutron source and advanced area detectors, has it become possible to get $S(Q, E)$ with large Q and E coverage and to obtain reliable Van Hove function experimentally. With these advances, self and distinct part of Van Hove function have been increasingly used to analyze the self and collective dynamics in various liquid systems, including water and aqueous salt solution[44-48]. An example is shown in Figure 2.8. Based on Equation 2.7 and 2.8, the self-part of VHF can be used to calculate the diffusion coefficient of the system. The role of distinct part of VHF in analyzing the collective dynamics will be emphasized in later chapters.

2.5 Summary

In this chapter, the atomic-level dynamics of viscous and diffusive behaviors in liquids was introduced. Then the progress in this area, especially in understanding the nature of viscosity through MD simulation, and the limitations such as the measurement of diffusivity through conventional methods were presented. Then the concept of Van Hove function and its recent development and advantages in analyzing the atomic-level dynamics in liquid systems were presented. This dissertation will focus on determination of atomic-level dynamics in metallic liquids through Van Hove function method based on inelastic neutron scattering experiments.

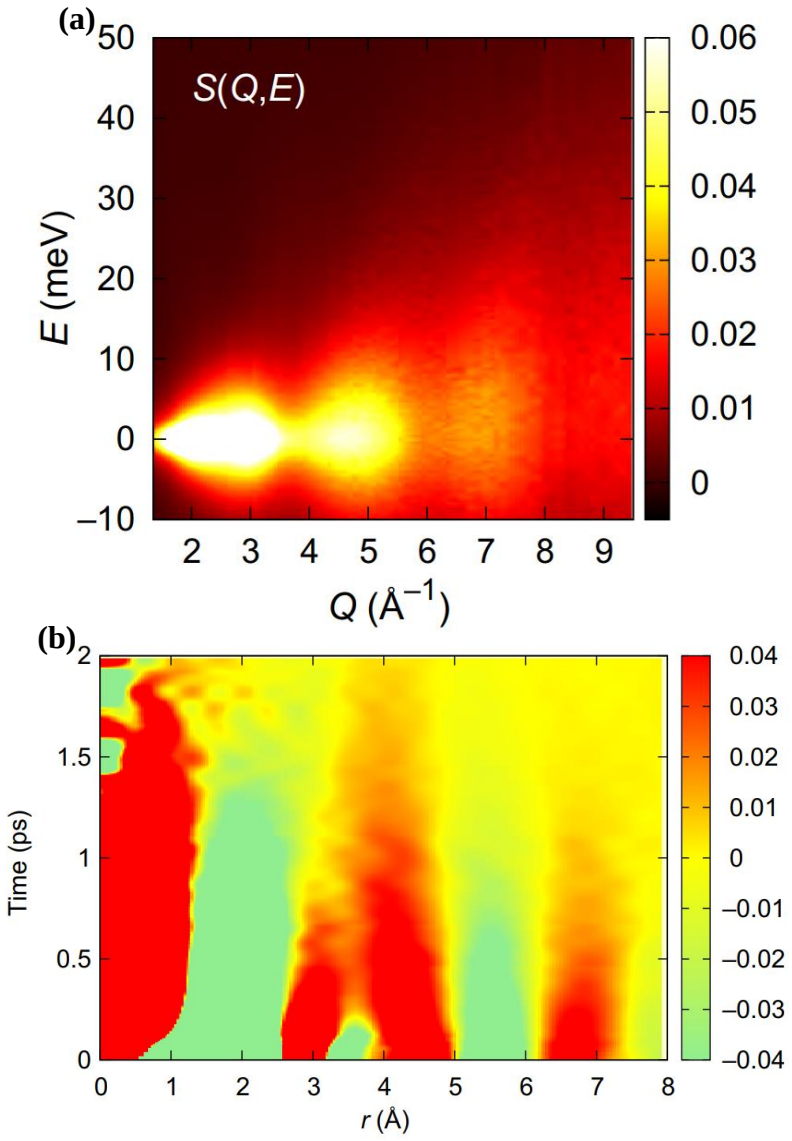

Figure 2.8 (a) Dynamic structure function, $S(Q, E)$, and (b) Van Hove function, $G(r, t)$, for liquid water determined by IXS experiments with recent instrumentation advances[48].

Chapter 3 Experimental Setup and Data Analysis Procedure to Obtain the Van Hove Function

3.1 Introduction

As mentioned in the previous chapter, the experimental determination of reliable and accurate Van Hove function (VHF) has only been possible with the recent development of the inelastic neutron/X-ray scattering instrumentations. In this chapter, the experimental setup for the inelastic neutron scattering measurements of $Zr_{50}Cu_{50}$ and $Zr_{80}Pt_{20}$ liquid samples will be first introduced and then the detailed data analysis procedure to determine the VHF with customized MATLAB codes will be presented.

3.2 Experimental details and setup

Measurements of metallic samples at high temperature are always troubled by issues such as the sample-container reaction and contamination, and oxidization. To minimize these issues, liquid samples in this experiment are handled by the technique of electrostatic levitation, providing a containerless and high vacuum environment[26, 49]. The inelastic neutron scattering (INS) experiment for metallic liquids was carried out at the Wide Angular-Range Chopper Spectrometer beamline (ARCS, BL-18, https://neutrons.ornl.gov/arcs)[50] at the Spallation Neutron Source (SNS) at Oak Ridge National Laboratory (ORNL), using the specially designed Electrostatic Levitator for Neutron (NESL)[51], which can be installed as a standard sample environment at the beamline. The ARCS beamline, as shown in Figure 3.1, is equipped with the large-area detector array that provides a large Q and E coverage.

To describe the technical details of the INS experiment, we use the $Zr_{50}Cu_{50}$ sample as an example. Solid spherical samples with the mass of about 300-400 mg and the diameter of about

4~5 mm were cast with the arc-melting method. One sample was released onto the top of the vertical post from the sample carousel which can hold about 30 samples. Then high voltage between the vertical electrodes is applied to levitate the sample and voltages between two pairs of side electrodes will be used to maintain the horizontal position of the sample. Next lasers are turned on to heat the sample until melting state (as shown in Figure 3.2). The sample will be heated up to a high temperature to burn out the impurities on the surface for a more stable levitation and temperature control. A few cycles of heating and free cooling are usually done to calibrate the solidus temperature, T_s, lowest supercooling temperature and the recalescence (recrystallization) temperature. Then the temperature is held at the desired temperature levels and neutron scattering data is collected for about 2 hours at each temperature for each sample. The desired temperatures are distributed below and above the solidus temperature (as listed in Table 3-1, in which T_s is 905 ℃ for $Zr_{50}Cu_{50}$ and 1180 ℃ for $Zr_{80}Pt_{20}$), taking into account the degree of supercooling and evaporation of the metallic elements of the sample and the heating capacity of the NESL levitator. Because this was the first experiment of this kind at SNS, a lot of preparation was done before the experiment and significant effort was put on the sample levitation and data collection to overcome the difficulties and problems ensued during the levitation. Measurements were made with neutron incident energy E_i = 20 meV. Since the energy resolution of INS measured data very much depends on the incident energy, attempts with E_i = 50 meV at ARCS and E_i = 10 meV at CNCS were also made, but the data will not be reported here. Same measurements were also carried out for $Zr_{80}Pt_{20}$ liquid samples.

The viscosity of all liquid samples were measured at different temperatures by the collaborators in Kelton's research group at Washington University in St. Louis using the oscillation method with

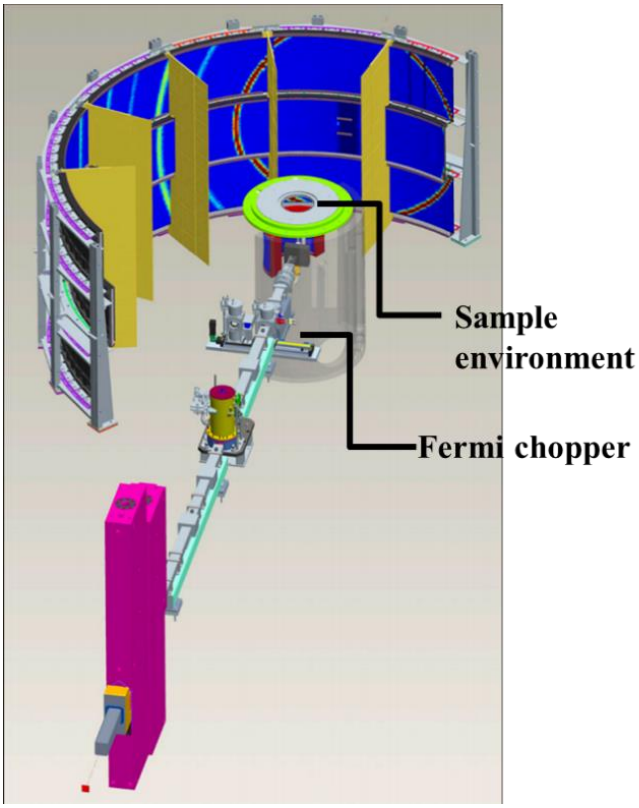

Figure 3.1 Engineering model of ARCS with neutron powder diffraction data superimposed on the large detector array. The NESL levitator can be installed as a standard sample environment.

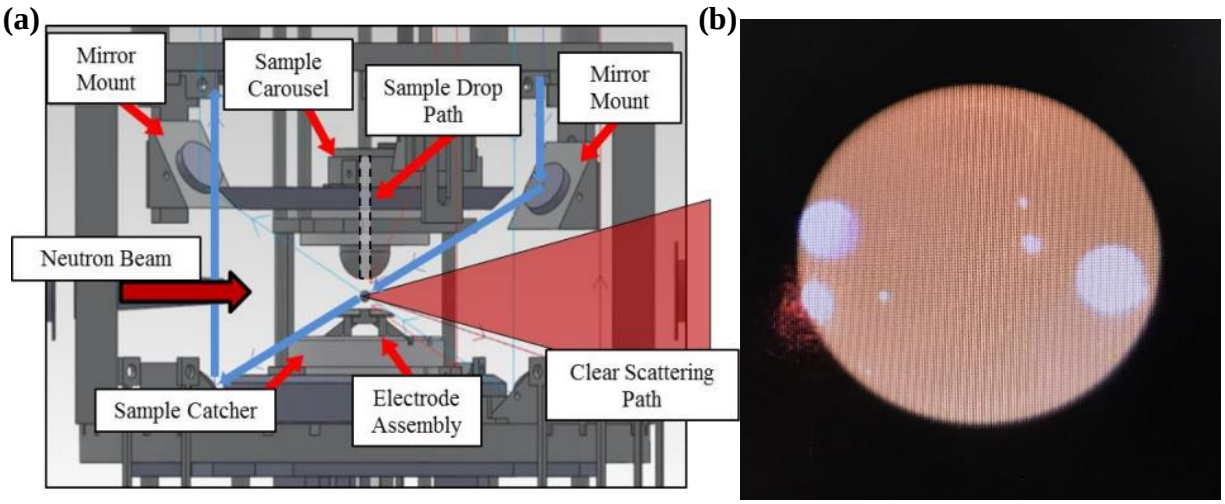

Figure 3.2 (a) The design sketch for part of the NESL, showing the sample position, some key parts, and the neutron scattering pathway. (b) An amplified image of the $Zr_{50}Cu_{50}$ droplet with diameter of 4~5 mm levitated and melted, ready for neutron scattering data collection.

Table 3-1 Temperatures for inelastic neutron scattering experiment for $Zr_{50}Cu_{50}$ and $Zr_{80}Pt_{20}$ samples.

Sample \ T(℃)	T_s -150	T_s -50	T_s +15	T_s +50	T_s+100	T_s+150	T_s+200	T_s+275	T_s+350
$Zr_{50}Cu_{50}$	755	--	855	920	955	1005	1055	--	--
$Zr_{80}Pt_{20}$	1030	1130	1195	1230	1280	1340	1400	1485	1540

a similar levitator[4]. Then the Maxwell relation time, τ_M, and the crossover temperature, T_A, can be determined from the measured viscosity data, which will be discussed in detail later.

3.3 Introduction to inelastic neutron scattering

The principle of inelastic neutron scattering technique will be briefly introduced here. As shown in Figure 3.3, in a direct-geometry spectrometer (DGS) like ARCS, the 'white' neutron beam coming from the source (target and moderator) becomes monochromatic after going through the Fermi chopper, which selects neutrons with a specified velocity. The monochromatic beam then interacts with the sample and neutrons lose energy to or gain energy from the sample due to their interaction with the matter, resulting in the change of direction and speed of the scattered neutrons. By tracking the impact position and time of flight for each neutron that arrives at the detector, the energy transfer E and momentum transfer $\boldsymbol{Q}$ could be obtained by

$$\begin{aligned} E &= E_i - E_f \\ \boldsymbol{Q} &= \boldsymbol{k}_i - \boldsymbol{k}_f \end{aligned} \tag{3.1}$$

where E_i and E_f are the initial and final energy of the neutron particles before and after the scattering, $\boldsymbol{k}_i$ and $\boldsymbol{k}_f$ are the initial and final wave vector of the neutron particles before and after the scattering, as shown in Figure 3.4. Note that the sketch is plotted in 2-D while the real scattering process happens in 3-D space.

A typical scattering pattern during INS measurement of a liquid sample on the large-area detector array is shown in Figure 3.5. The broad scattering ring is due to the largely homogeneous structure of the liquid state. Note that there are several big gaps (dark) between the detector sub-arrays, which will be filled by interpolation later during the data analysis procedure.

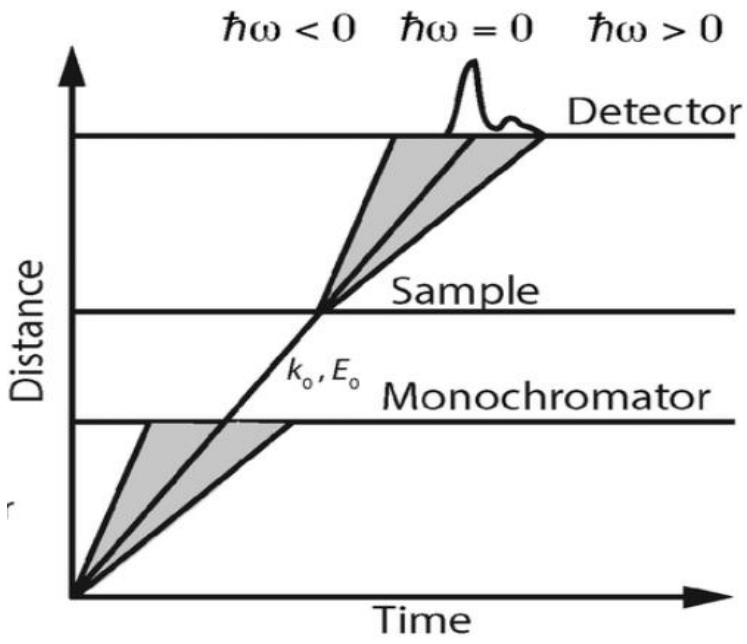

Figure 3.3 Sketch showing the time of flight (TOF) inelastic neutron scattering for a direct-geometry spectrometer like ARCS.

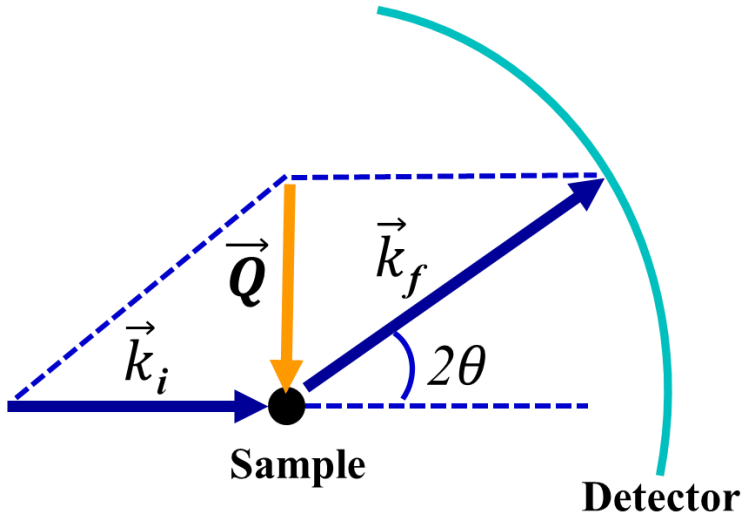

Figure 3.4 Momentum transfer in the INS measurement plotted in 2-D.

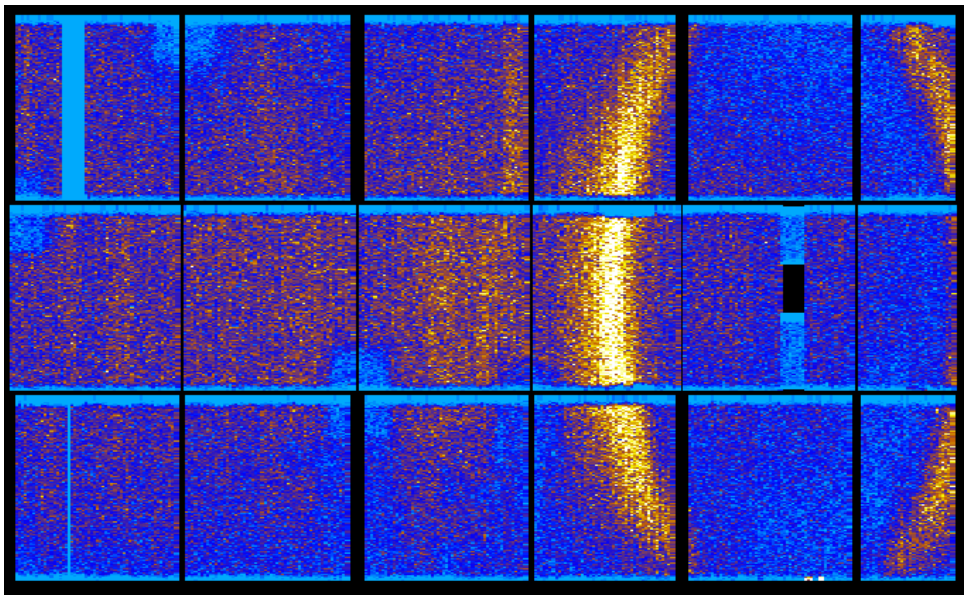

Figure 3.5 A typical detector image obtained from the INS measurement of $Zr_{50}Cu_{50}$ liquid.

3.4 Procedure to obtain the Van Hove function

3.4.1 Overview

For the case of neutron scattering by a monatomic liquid, the partial differential scattering cross section per particle has the form

$$\frac{d^2\sigma}{d\Omega dE} = \frac{b^2}{\hbar}\frac{k_f}{k_i}S(\mathbf{Q},\omega). \tag{3.2}$$

where b is the coherent scattering length. Then mathematically, the Van Hove function can be calculated from $S(Q, \omega)$ through double Fourier transformation[35, 38, 40],

$$G(\mathbf{r},t) = \frac{1}{(2\pi)^3\rho}\int S(\mathbf{Q},\omega)\exp[i(\omega t - \mathbf{Q}\cdot\mathbf{r})]d\omega d\mathbf{Q}, \tag{3.3}$$

which is the fundamental algorithm in the self-developed and customized MATLAB codes to determine the Van Hove function. The flow chart of the whole data analysis procedure is shown in Figure 3.6. The case of $Zr_{50}Cu_{50}$ at T_s+50 ℃ (955 ℃) INS measurement with incident energy of 20 meV will be used as the example to elaborate the data analysis procedure. The MATLAB codes used are attached in the Appendix.

3.4.2 Dynamic structure function $S(Q, E)$

First, the energy transfer E and momentum transfer Q were calculated from the raw time-of-flight (TOF) data based on the standardized direct-geometry spectrometer (DGS) reduction routine, using the Mslice in DAVE [52] or Mantidplot [53] software from Mantid project (https://www.mantidproject.org/Main_Page). and beamline parameters extracted from standard white beam calibrations [54], thus the $I(Q, E)$ spectrum was obtained for the liquid samples and the empty NESL levitator chamber (for background subtraction), as shown in Figure 3.7. Note that

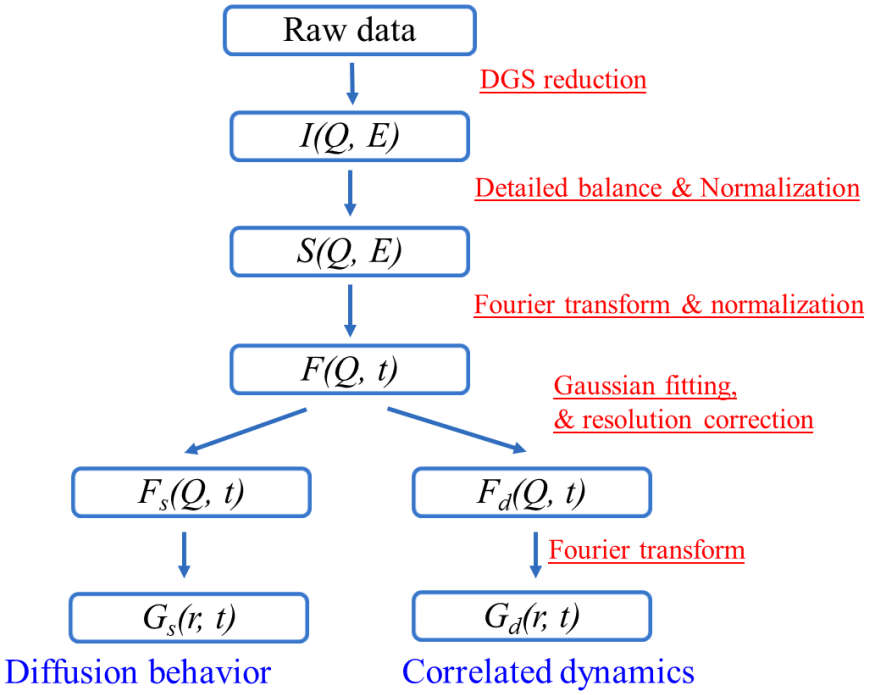

Figure 3.6 Flow chart for calculating the Van Hove function, $G(r, t)$, from data measured by inelastic neutron scattering for metallic liquids.

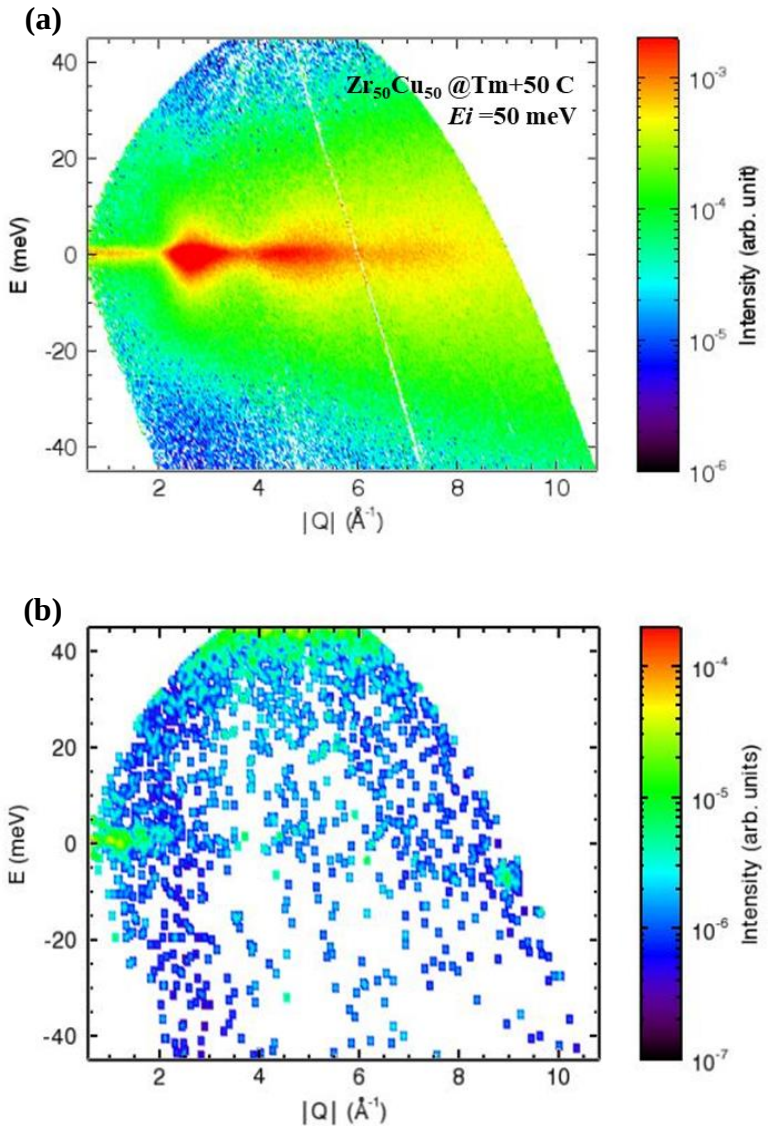

Figure 3.7 (a) Typical $I(Q, E)$ spectrum obtained from raw INS data through DGS reduction for $Zr_{50}Cu_{50}$ liquid. (b) $I(Q, E)$ spectrum measured for the empty NESL levitator chamber and used for background subtraction.

the scattering signal from the empty levitator chamber as background is very small compared with that from the sample, justifying the advantage of using the levitator.

To have sufficiently high statistics, the part of $I(Q, E)$ above the maximum Q at $E = 0$ will be discarded. This Q_{max} value is about 9.0 $Å^{-1}$ for $E_i = 50$ meV, which is enough to cover the first three main scattering peaks, and it is about 5.74 $Å^{-1}$ for $E_i = 20$ meV, which is enough to cover the first two main scattering peaks. Scattering peaks beyond this Q_{max} have very low intensity and contribute little to Fourier transform-obtained $F(Q, t)$ and $G(r, t)$, thus the Q-range measured by this INS experiment is reasonably enough.

The obtained $I(Q, E)$ was normalized by the square of mean scattering length $\langle b \rangle^2$, which is 0.553 for $Zr_{50}Cu_{50}$ and 0.585 for $Zr_{80}Pt_{20}$. Detailed balance was then applied to the $I(Q, E)$ spectrum by [55]

$$I(Q,E) = I(Q,-E)\exp(\hbar\omega / k_B T), \tag{3.4}$$

in order to extend data to the inaccessible positive energy transfer region restricted by the dynamic limitations of direct-geometry INS, and interpolation was also used to fill the blank stripes due to the gaps between detector sub-arrays. Hence the dynamic structure function $S(Q, E)$ was obtained (as shown in Figure 3.8), although it's not normalized to unity at large Q. This normalization will be done after the energy resolution correction in the following part.

3.4.3 Intermediate scattering function $F(Q, t)$ and energy resolution correction

The intermediate scattering function, $F(Q, t)$, was determined through the Fourier transform of $S(Q, E)$ over E or ω following

$$F(Q,t) = \int_{-E_{\max}}^{E_{\max}} S(Q,\omega)\exp(i\omega t)d\omega . \tag{3.5}$$

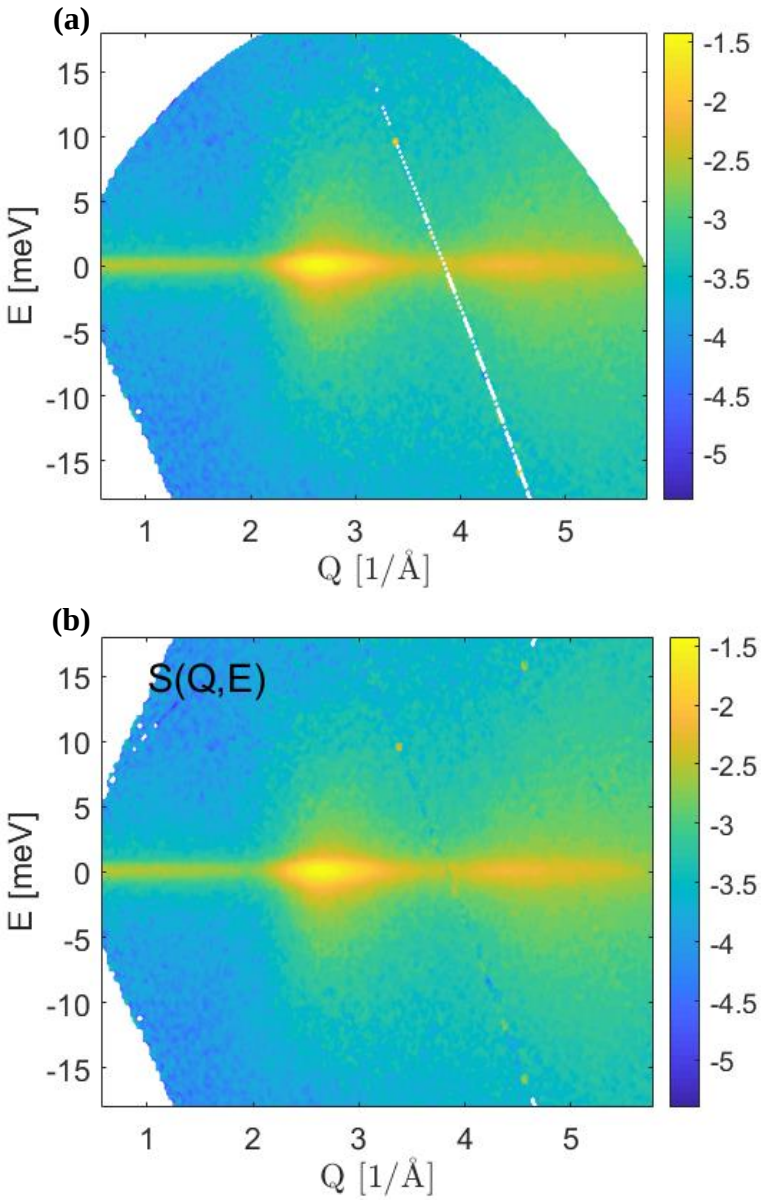

Figure 3.8 Dynamic structure function $S(Q, E)$ normalized by $\langle b \rangle^2$: (a) before and (b) after the detailed balance and interpolation to fulfill the detector gaps.

The contour plot and different time slices are shown in Figure 3.9. It is easy to see that first maximum of $F(Q, t)$ decays quickly with time and the $t = 0$ slice $F(Q, t=0)$ is oscillating around a constant value as $Q \rightarrow \infty$, suggesting that the relation $S(Q) = F(Q, t=0)$ is followed. Further normalization of $F(Q, t)$ by this constant value will be applied later after the energy resolution correction to enforce that $S(Q)$ oscillates around unity as $Q \rightarrow \infty$. The time dependent relaxation of the first maximum of $F(Q, t)$, $F(Q_1, t)$, also known as α-relaxation, has been widely used to analyze the structural change of the liquid, while B. Wu showed that the α-relaxation using reciprocal space information doesn't provide the true structural change or local dynamics of the liquid system[56].

In typical INS measurements the energy resolution depends on the incident energy and the geometrical orientation with respect to the moderator, which widens the elastic line. Consequently, the scattering intensity from the sample is convoluted with neutron beam energy profile. One way to improve the energy resolution is to implement the INS experiment with lower incident energy, which is not practical at ARCS where the lowest feasible incident energy is about 20 meV considering the neutron beam flux. Although INS experiment with lower incident energy can be done at other beamlines like CNCS, its Q coverage is smaller and the combination of data from different beamlines is difficult. Another way is to implement the energy resolution correction by applying deconvolution of the beamline energy profile. With a reasonable assumption that vanadium is an almost purely incoherent scatterer, its scattering intensity at the same incident energy can be used to describe the neutron energy profile. Hence, the total dynamic structure function can be expressed as

$$S_{tot}(Q,E) = S_{sample}(Q,E) * S_V(Q,E) \ , \tag{3.6}$$

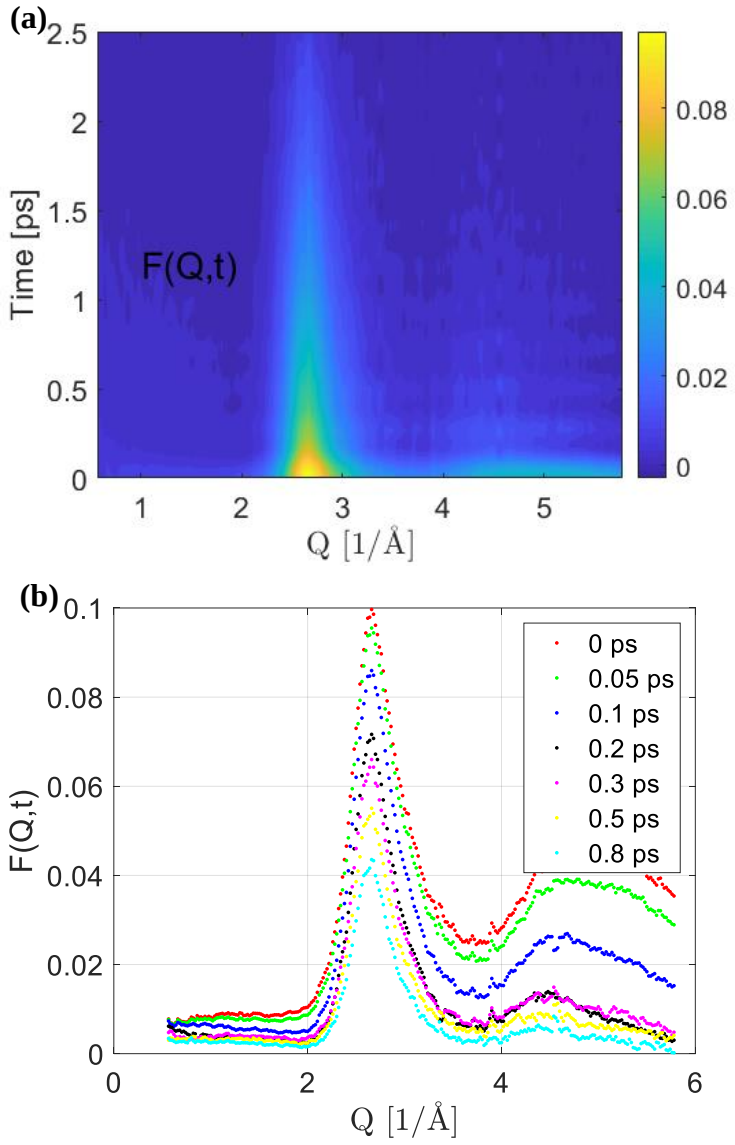

Figure 3.9 Intermediate scattering function $F(Q, t)$ before normalization and energy resolution correction: (a) contour plot and (b) different time slices.

where S_{tot} is the total dynamic structure function directly measured from the liquid samples, S_{sample} is the intrinsic dynamic structure function for the sample and S_V is the dynamic structure function measured from the standard vanadium sample with the same incident energy at room temperature, which is almost Q-independent and represents the beamline geometry and neutron energy profile. By applying the Fourier transform over E to both sides of Eq. 3.6, the convolution becomes a multiplication,

$$F_{tot}(Q,t) = F_{sample}(Q,t) \cdot R(t), \tag{3.7}$$

where the energy resolution function $R(t)$ is the Fourier transform of $S_V(Q, E)$, as shown in Figure 3.10 for E_i = 20 meV. A 6-order polynomial fitting was used to get a smooth $R(t)$. Note that $R(t)$ goes to very small or even negative values when t > 2.5 ps, which is obviously unreasonable and will result in some over correction. Therefore, the part longer than 2.5 ps was discarded in the following procedure of the data analysis.

Then the true intermediate scattering function for the sample can be easily obtained by

$$F_{sample}(Q,t) = F_{tot}(Q,t) / R(t). \tag{3.8}$$

The effect of energy resolution correction can be shown by plotting the α-relaxation for $Zr_{50}Cu_{50}$ at T_s + 50 °C (see Figure 3.11). Before energy resolution correction (deconvolution), the relaxation is much faster and gives a short relaxation time. After energy resolution correction, the α-relaxation gives a larger and more accurate relaxation time. Although there is some degree of over correction for longer times and for samples at lower temperatures where the relaxation curve became too flat, it is still more worthwhile than having data without the correction.

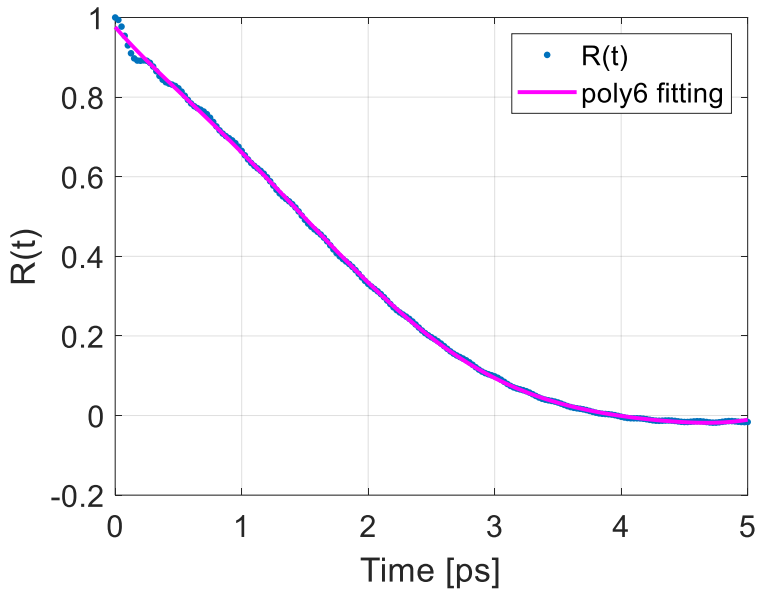

Figure 3.10 Energy resolution function $R(t)$ for E_i = 20 meV obtained from INS measurement of a vanadium standard.

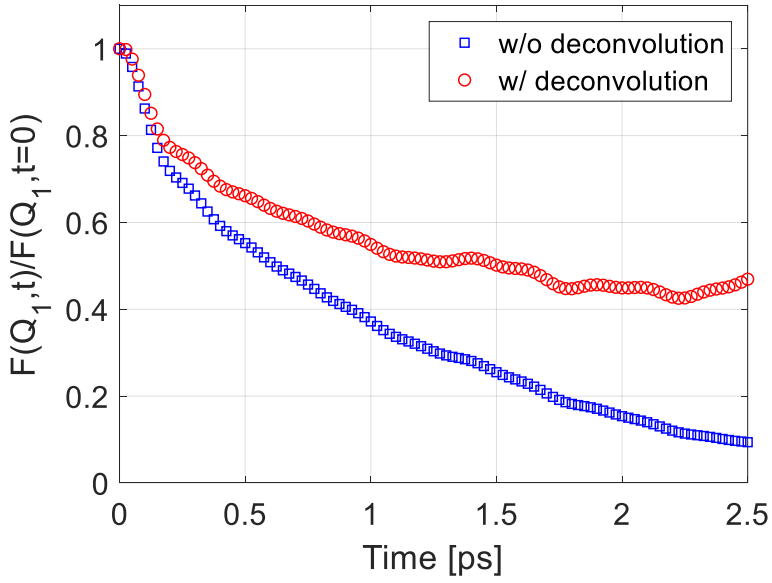

Figure 3.11 Effect of energy resolution correction shown by plotting the α-relaxation for $Zr_{50}Cu_{50}$ at T_s + 50 °C.

The self-part of the intermediate scattering function, $F_s(Q, t)$, is mostly corresponded to the incoherent part of the scattering, thus follows the Gaussian approximation

$$F_s(Q,t) \approx A(t)\exp[-w(t)Q^2], \tag{3.9}$$

where $A(t)$ and $w(t)$ are the time-dependent amplitude and width function. The fitting range is from 1.9 $Å^{-1}$ to Q_{max} for $Zr_{50}Cu_{50}$ and from 1.8 $Å^{-1}$ to Q_{max} for $Zr_{80}Pt_{20}$. Each time slice was double-checked to make sure that the fitting was reasonably good enough (some examples shown Figure 3.12). $F(Q, t)$ in all t-slices can be fitted with the Gaussian curve to separate the self-part, $F_s(Q, t)$, and distinct part, $F_d(Q, t)$ (= $F(Q, t) - F_s(Q, t)$). Another benefit of the Gaussian fitting is to extrapolate the data to a larger Q range (from 0 to 50 $Å^{-1}$) to avoid termination errors for the second Fourier transform[40]. Fitting parameters $A(t)$ and $w(t)$ are plotted against t, as shown in Figure 3.13. The reason for oscillations in $A(t)$ and $w(t)$ is not surely clear and is possibly due to contributions from errors of the original data and the uncertainty of the fitting. They are nonnegligible but small when considering the whole time range from 0 to 2.5 ps. At $t = 0$, $w(t = 0) = 0$, and $F(Q, t = 0)$ oscillates around the constant value $A(t = 0)$ as $Q \rightarrow \infty$, justifying the reliability of the Fourier transform. It is also noted that the first few points of $w(t)$ other than $t = 0$ are also zero because of the fitting algorithm cannot distinguish their slight difference with the $F(Q, t = 0)$ curve.

Both $F_s(Q, t)$ and $F_d(Q, t)$ are then normalized by $A(t = 0)$ value to enforce that $S(Q)$ oscillates around unity as $Q \rightarrow \infty$. The normalized $F(Q, t)$ are shown in Figure 3.14. The self and distinct parts of $F(Q, t)$ reflect the single particle and collective atomic density fluctuations and are dominated by the incoherent and coherent neutron scattering, respectively. The maximum $S(Q)$ at $Q_1 = 2.66$ $Å^{-1}$ is about 2.47 for $Zr_{50}Cu_{50}$ at $T_s + 50$ °C, reasonably smaller than the reference value of 3.05 at room temperature obtained through high energy X-ray diffraction.

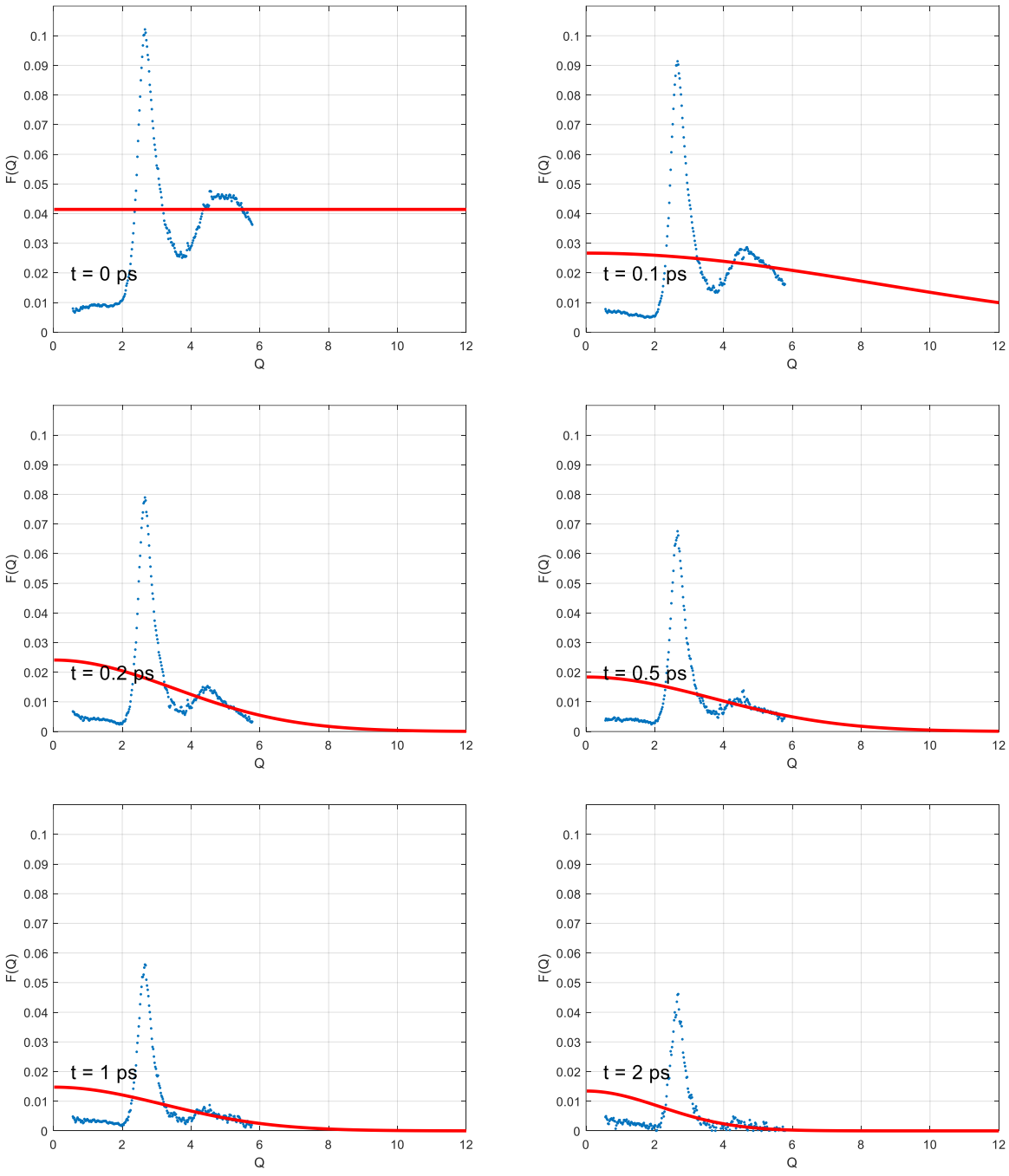

Figure 3.12 $F(Q, t)$ fitted by the Gaussian approximation at different times to separate the self and distinct part of $F(Q, t)$.

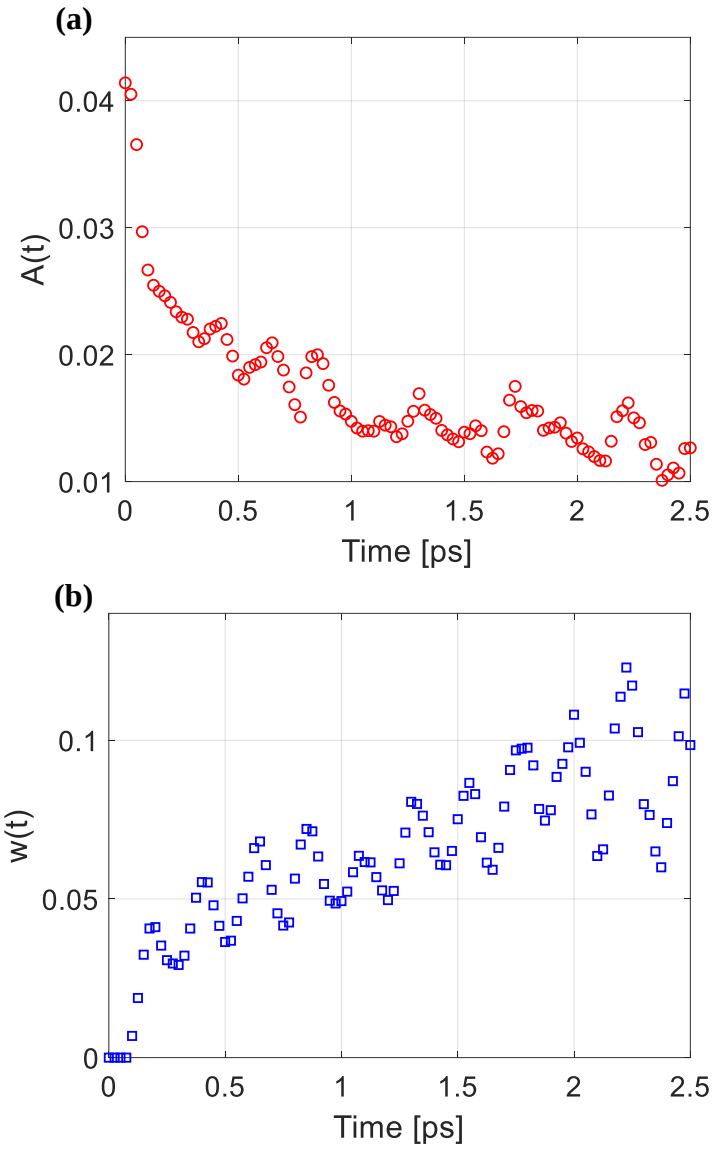

Figure 3.13 Gaussian fitting parameters $A(t)$ (a) and $w(t)$ (b) plotted with time.

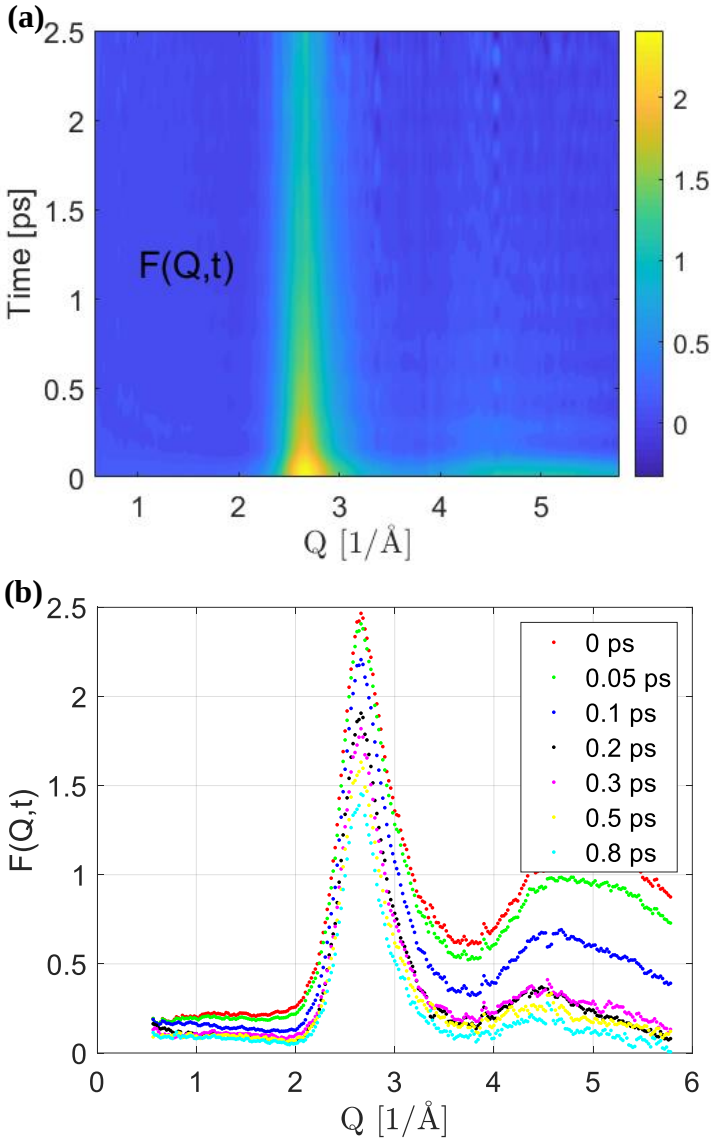

Figure 3.14 Final intermediate scattering function $F(Q, t)$ for $Zr_{50}Cu_{50}$ liquid sample at T_s + 50 ℃: (a) contour plot and (b) different time slices.

3.4.4 Distinct part of the Van Hove function

Since the metallic liquids are isotropic, $\exp(i\mathbf{Q}\cdot\mathbf{r})$ can be changed to $4\pi Q^2 \sin(Qr)/(Qr)$, and the distinct part of the Van Hove function, $G_d(r, t)$, can be obtained from the Fourier transform of $F_d(Q,t)$ over Q following the equation:

$$G_d(r,t) = \frac{1}{2\pi^2\rho}\int_{Q_{\min}}^{Q_{\max}} F_d(Q,t)\frac{\sin(Qr)}{Qr}Q^2 dQ, \tag{3.10}$$

where ρ is the atomic number density. ρ changes from 0.555 to 0.544 in the measured temperature range of 755 to 1055 ℃, which is quite small and can be ignored. The damping function $\sin(x)/x$ was applied to the tail of $F_d(Q, t)$ to suppress the truncation error in the Fourier transform.

When $t = 0$,

$$\begin{aligned} G_d(r,0) &= \frac{1}{2\pi^2\rho}\int_{Q_{\min}}^{Q_{\max}} \left[F(Q,0)-1\right]\frac{\sin(Qr)}{Qr}Q^2 dQ \\ &= \frac{1}{2\pi^2 r\rho}\int_{Q_{\min}}^{Q_{\max}} \left[S(Q)-1\right]Q\sin(Qr)dQ \\ &= g(r)-1 \end{aligned}, \tag{3.11}$$

which can be used as a reference to check the validity of the obtained $G_d(r, t)$. An example of the distinct part of Van Hove function, $G_d(r, t)$, is shown in Figure 3.15. It must be noted that the experimentally obtained $G_d(r, t)$ here is different from the theoretical one defined by Equation 2.5 by a constant of 1, which doesn't affect the following analysis of relaxation behavior. Further analysis based on the relaxation behavior of $G_d(r, t)$ will be discussed in the later chapter in order to determine the atomic-level collective dynamics in metallic liquids.

3.4.5 Self-part of the Van Hove function

Although the self-part of the intermediate scattering function, $F_s(Q, t)$, was approximated by the Gaussian function in Eq. 3.9, it is actually not strictly correct because it has the contributions from

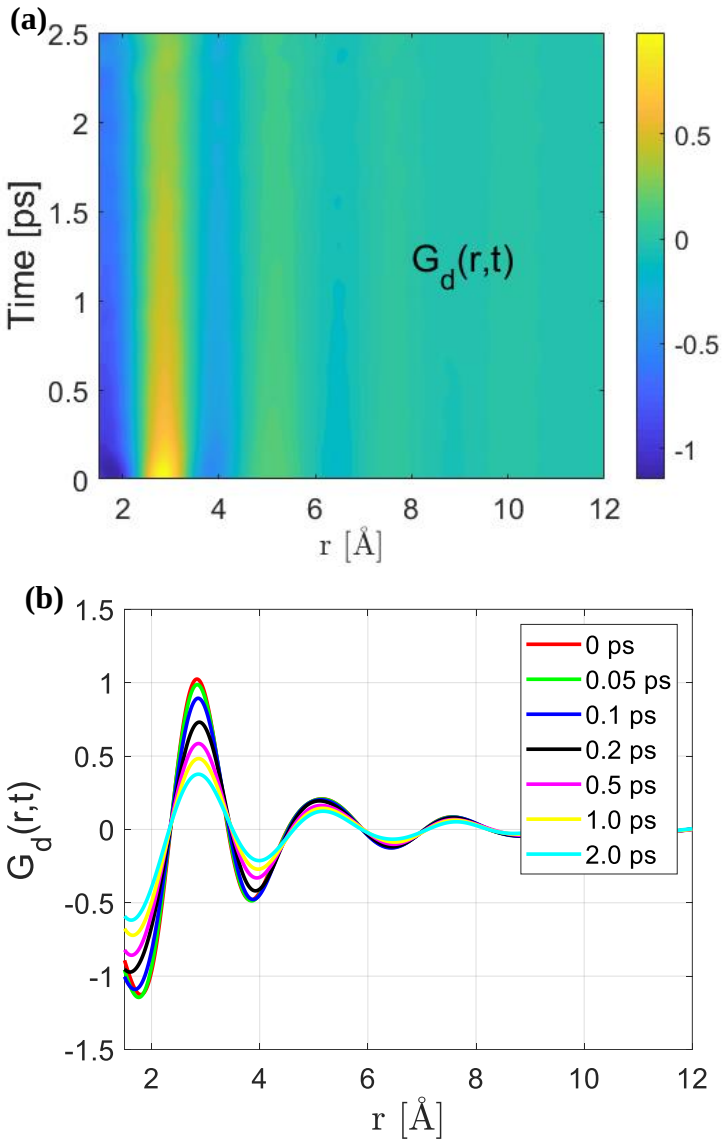

Figure 3.15 Distinct part of the Van Hove function obtained for $Zr_{50}Cu_{50}$ at T_s + 50 °C: (a) contour plot and (b) different time slices.

both the coherent and incoherent part of the scattering. Therefore, instead of using the Gaussian $F_s(Q, t)$ to calculate the self-part of the Van Hove Function, $G_s(r, t)$, we will use a modified total $F(Q, t)$ to obtain the total $G(r, t)$ through Fourier transform, and the low-r part of total $G(r, t)$ with $r \leq 1.5$ Å will be used to represent the $G_s(r, t)$. Initial $F(Q, t)$ is not used here in order to reduce the termination errors because of the limited Q range from this INS experiment resulting in incomplete decay to zero at Q_{max} . This is slightly different from the method used by Y. Shinohara in Ref. [57]. The modified total $F(Q, t)$ is calculated by

$$\begin{aligned} F_{tot}(Q,t) &= \text{damped } F_d(Q,t) + \text{Gaussian } F_s(Q,t) \\ &= \left(F(Q,t) - A(t)\exp[-w(t)Q^2]\right)\cdot\frac{\sin x}{x} + A(t)\exp[-w(t)Q^2], \end{aligned} \tag{3.9}$$

and an example is shown in Figure 3.16.

Then $G_s(r, t)$, or the low-r part of $G_{tot}(r, t)$, can be obtained through Fourier transform over Q and is plotted in Figure 3.17. When $t < 0.1$ ps, the termination errors are impossible to avoid, so only $G_s(r, t)$ with longer time $t \geq 0.1$ ps is calculated with this method. The obtained $G_s(r, t)$ will be used to analyze the self-motion of atoms in the liquids later.

3.5 Summary

In this chapter, the technique of inelastic neutron scattering (INS) and the experimental setup and details for the INS measurement of metallic liquid samples using the NESL levitator were covered. A full data analysis procedure and corresponding MATLAB codes were developed and the detailed procedure to obtain the Van Hove function (VHF) from INS data was elaborated step-by-step, including the determination of dynamic structure function, $S(Q, E)$, intermediate scattering function, $F(Q, t)$, and the self and distinct parts of the VHF. Highly reliable VHFs were determined and will be used to analyze the atomic-level dynamics in metallic liquids.

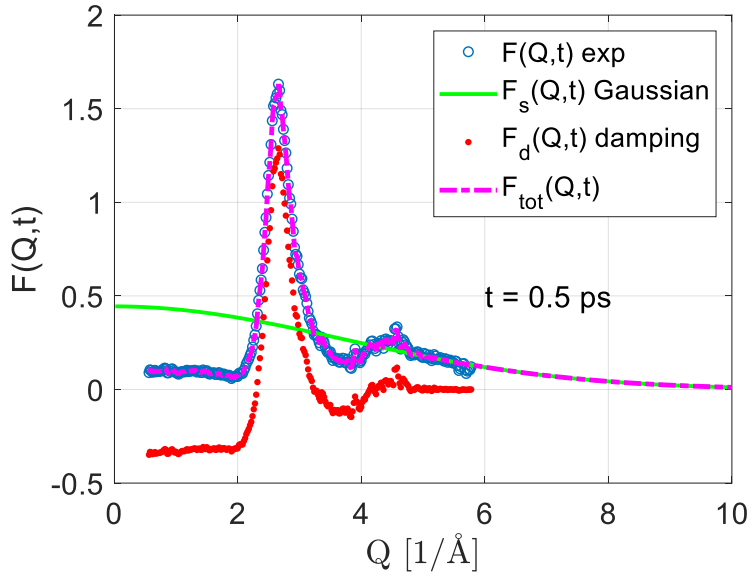

Figure 3.16 Calculation of the modified total intermediate scattering function, $F_{tot}(Q, t)$, at t = 0.5 ps.

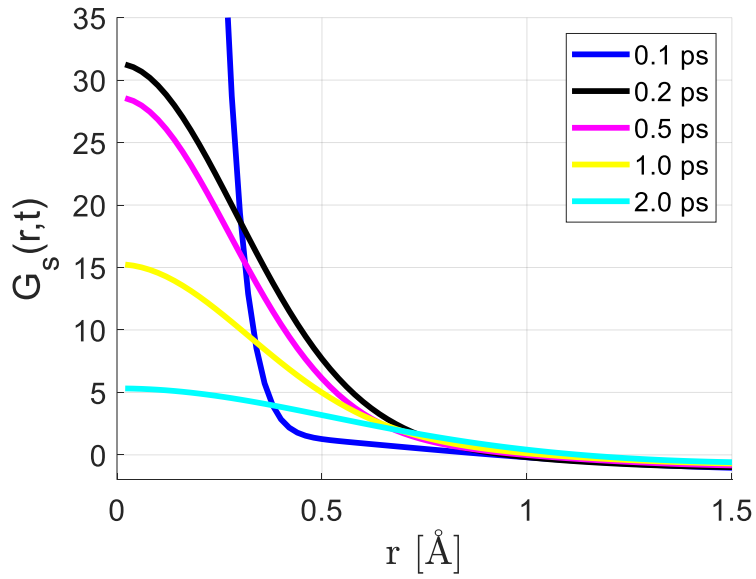

Figure 3.17 The self-part of Van Hove function obtained for $Zr_{50}Cu_{50}$ at T_s + 50 °C.

Chapter 4 Local Structures and Dynamics in Metallics Liquids

The Van Hove function (VHF) are determined from inelastic neutron scattering measurements for $Zr_{50}Cu_{50}$ and $Zr_{80}Pt_{20}$ liquid samples at different temperatures, using the self-developed data analysis procedures described in Chapter 3. The measured temperatures are distributed around the solidus temperatures for each sample. There are 6 different levels from T_s - 150 ℃ to T_s + 200 ℃ (755 ℃ to 1055 ℃) for $Zr_{50}Cu_{50}$ and 9 different levels from T_s-150 ℃ to T_s +350 ℃ (1030 ℃ to 1540 ℃) for $Zr_{80}Pt_{20}$. The measured temperature ranges inside the NESL levitator are limited by the supercooling degree of the liquid samples before crystallization as the low limit and by the evaporation issue of the metallic elements as the high limit. The obtained VHFs, including the self and distinct parts, can be used to analyze the single particle motion and collective dynamics at the atomic level for the metallic liquids, respectively. Meanwhile, the t = 0 slice represents the instantaneous structure for the liquids. In this Chapter, the atomic-level structures and local dynamics based on VHFs will be reported.

4.1 Temperature dependent structure information

When t = 0, the dynamic scattering function, $F(Q, t=0)$, equals the structure function, $S(Q)$, and the distinct part of the Van Hove function, $G_d(r, t=0)$, approaches to the pair distribution function, $g(r)$-1, as depicted in Equation 3.11. The coordination number, which is the number of neighboring atoms for the center atom inside the first atomic shell, can be calculated by the equation:

$$N = \int_{r_1}^{r_2} 4\pi r^2 \rho_0 g(r) dr \ , \qquad (4.1)$$

where ρ_0 is the atomic number density and $[r_1, r_2]$ is the distance range for the first atomic shell. These functions provide the instantaneous structural information in the samples. Besides,

compared with the reference data, they can be used to verify the procedures and algorithms used to determine the VHFs and the reliability of the obtained VHFs.

As shown in Figure 4.1, the main peak maximum of the structure function, $S(Q_1)$, is about 2.5 at Q_1 = 2.66 Å^{-1} for $Zr_{50}Cu_{50}$ and for $Zr_{80}Pt_{20}$ decreases from 3.56 to 2.85 at Q_1 = 2.50 Å^{-1} with the increasing temperature, and is smaller than the reference value of 3.05 (for $Zr_{50}Cu_{50}$) and 4.09 (for $Zr_{80}Pt_{20}$) at room temperature obtained through high energy X-ray diffraction. The main peak maximum of the PDF, $g(r_1)$-1, is around 1.05 for $Zr_{50}Cu_{50}$ and for $Zr_{80}Pt_{20}$ decreases from 1.4 to 1.2 with the increasing temperature. Coordination number is about 12.8 for $Zr_{50}Cu_{50}$ and 12.9 for $Zr_{80}Pt_{20}$ at all temperatures, which is very close to the theoretical value of 4π = 12.56, further justifying the procedure to obtain the VHF and the validity of the results.

4.2 Relaxation of distinct part of the Van Hove function

Multiple parameters related to the distinct part of the VHF, $G_d(r_1, t)$, can be used to depict the slowdown of atomic-level dynamics in the metallic liquids. The time dependent relaxation of the first maximum of the intermediate scattering function, $F(Q_1,t)$, also known as the α-relaxation (as plotted in Figure 4.2), has been widely used to analyze the structural relaxation of liquids, while B. Wu[56] showed that the α-relaxation using reciprocal space information doesn't correctly provide the true structural change or local dynamics of the liquid system.

The maximum of the first peak intensity of the distinct VHF, $G_d(r_1, t)$, is also decaying with time and can be used to analyze the dynamic relaxation of the liquids, as shown in Figure 4.3 for $Zr_{50}Cu_{50}$ and in Figure 4.4 for $Zr_{80}Pt_{20}$. However, the peak intensity maximum of $G_d(r, t)$ only gives the atomic density at the specific distance r_1, instead of a whole picture of the first nearest neighboring shell.

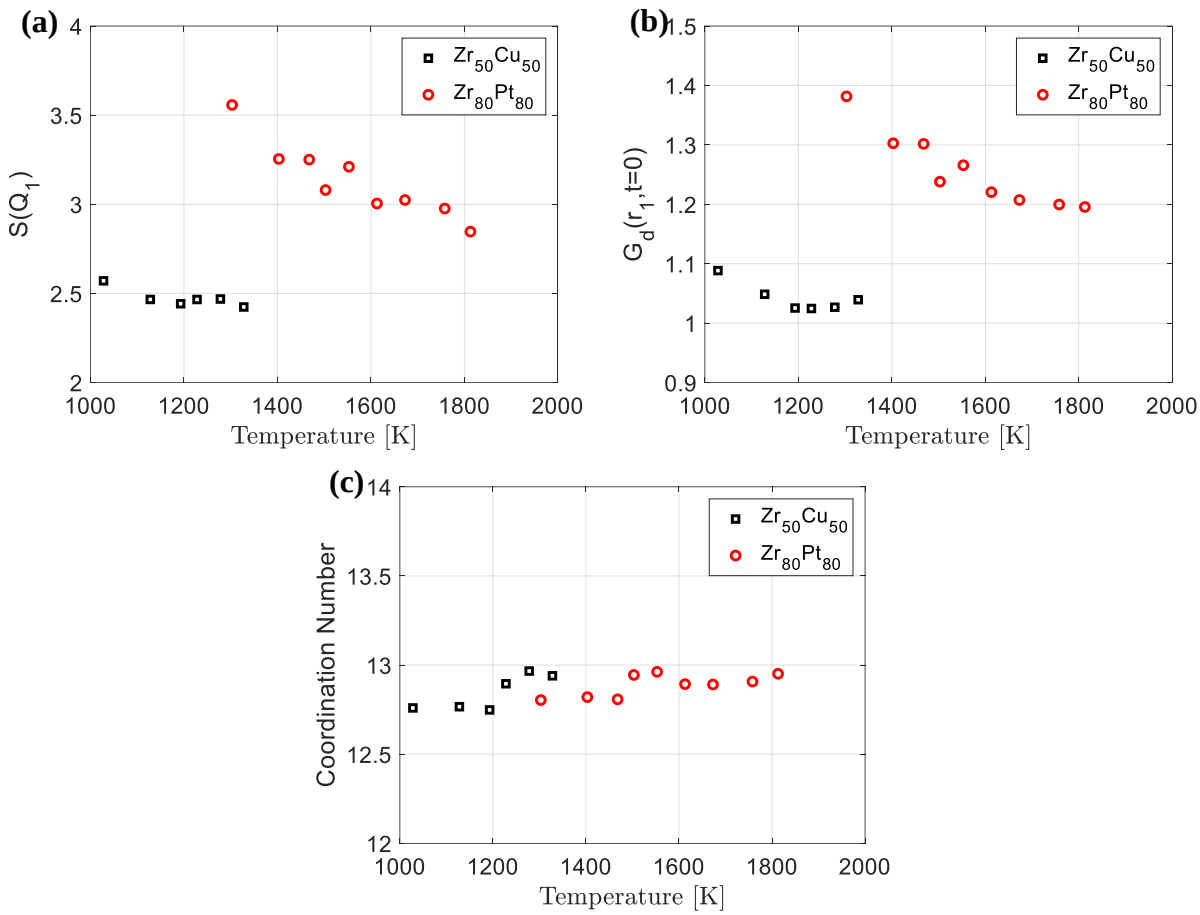

Figure 4.1 Structure function main peak maximum $S(Q_1)$ (a), PDF main peak maximum $g(r_1)$-1 (b), and coordination number (c), plotted against temperature for $Zr_{50}Cu_{50}$ and $Zr_{80}Pt_{20}$.

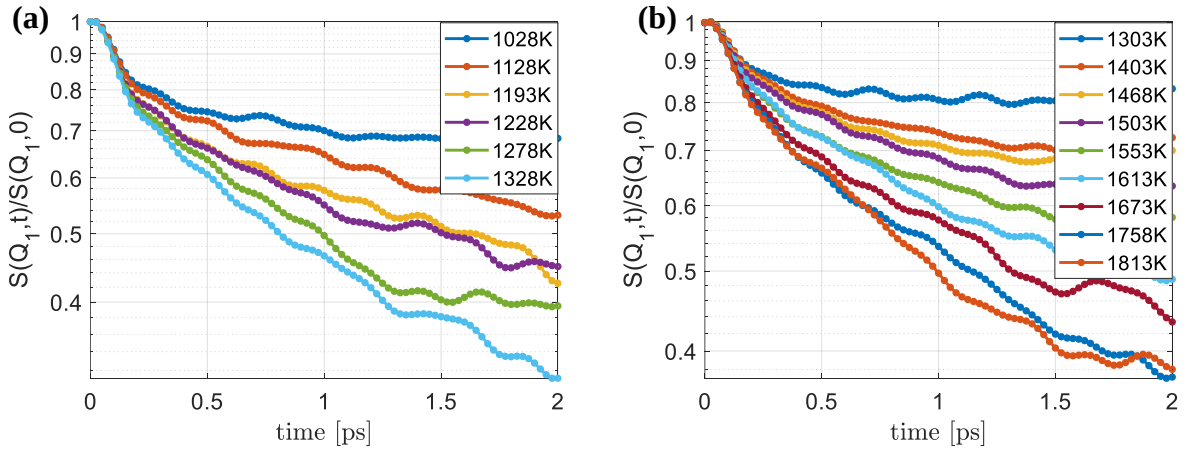

Figure 4.2 Normalized $F(Q_1, t)$ as a function of time describes the α-relaxation for (a) $Zr_{50}Cu_{50}$ and (b) $Zr_{80}Pt_{20}$ at different temperatures.

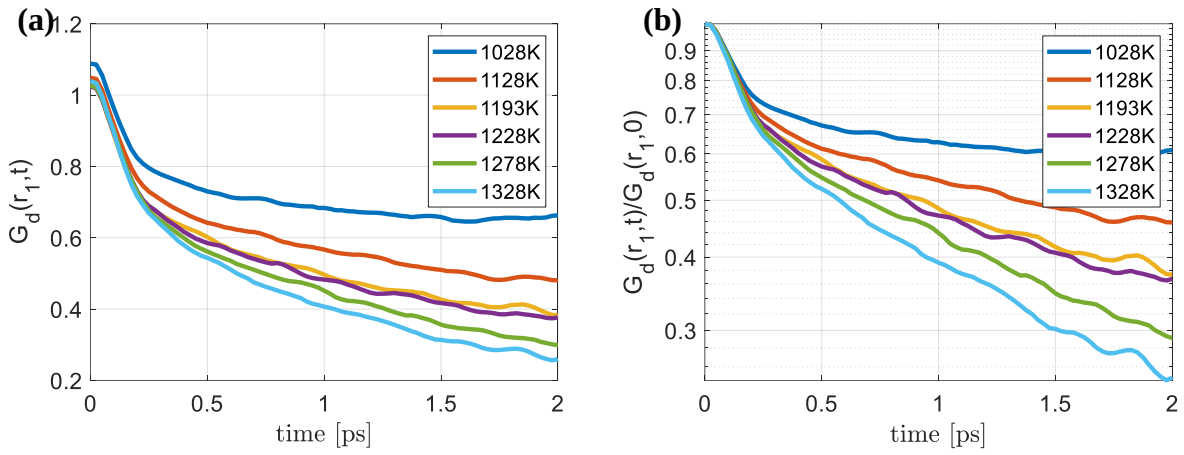

Figure 4.3 (a) Unnormalized and (b) normalized $G_d(r_1, t)$ plotted as a function of time for $Zr_{50}Cu_{50}$ at different temperatures.

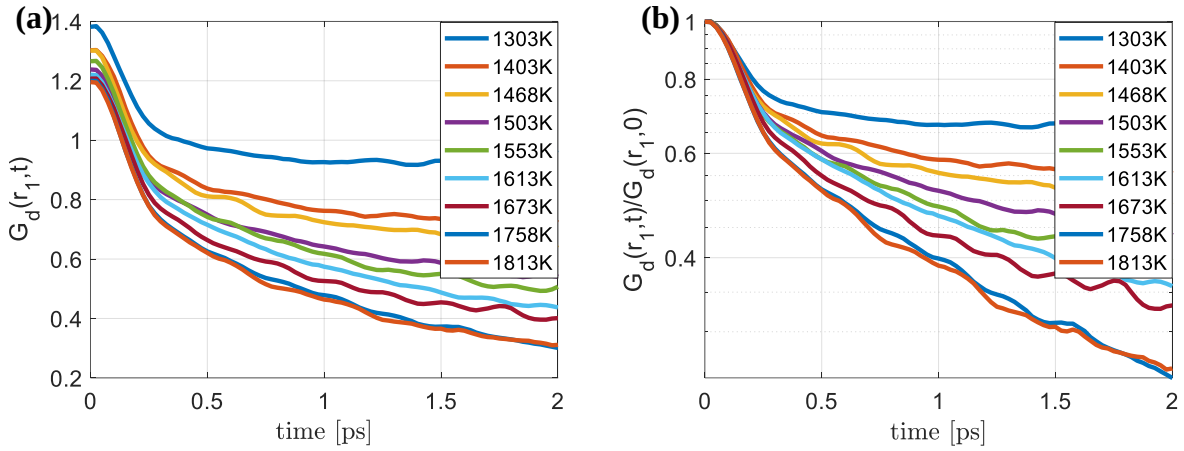

Figure 4.4 (a) Unnormalized and (b) normalized $G_d(r_1, t)$ plotted as a function of time for $Zr_{80}Pt_{20}$ at different temperatures.

It is also found that the relaxation slows down with increasing r (as shown in Figure 4.5 for $Zr_{80}Pt_{20}$ at T_s + 200 °C.), which is consistent with the conclusion from MD simulations in Ref. [56], although the low intensities and large errors in the second and third peaks of the experimentally obtained $G_d(r, t)$ make it impossible for quantitative analysis.

After attempts with different parameters, we finally define a new parameter $\Delta N_1(t)$ as

$$\Delta N_1(t) = \int_{r_1}^{r_2} 4\pi r^2 \rho_0 G_d(r,t) dr \,, \tag{4.2}$$

where integration range $[r_1, r_2]$ is the distance range of the first peak where the value of $G_d(r,t)$ is positive. Taking into account the coordination number defined by Equation 4.1, the physical meaning of $\Delta N_1(t)$ is closely related to part of the coordination number that is larger than the long-range average atomic number density, i.e., the density excess in the first atomic shell.

Its value at t = 0 is about 3.8 for $Zr_{50}Cu_{50}$ and decreases from 4.8 to 4.3 with the increasing temperature for $Zr_{80}Pt_{20}$, as shown in Figure 4.6, which means there is this number of more atoms in the first shell than the long-range average for the instantaneous structure. The $\Delta N_1(t)$ normalized by its value at t = 0 are plotted in Figure 4.7 for $Zr_{50}Cu_{50}$ and $Zr_{80}Pt_{20}$ liquids at different temperatures. Evidently, the relaxation slows down as the temperature decreases and two relaxation modes can be observed for both $Zr_{50}Cu_{50}$ and $Zr_{80}Pt_{20}$ liquids at all different temperatures; a faster relaxation mode when t < 0.25 ps and a slower one when t > 0.25 ps, which correspond to the quicker ballistic motion and slower collective motion of atoms in the metallic liquids, respectively.

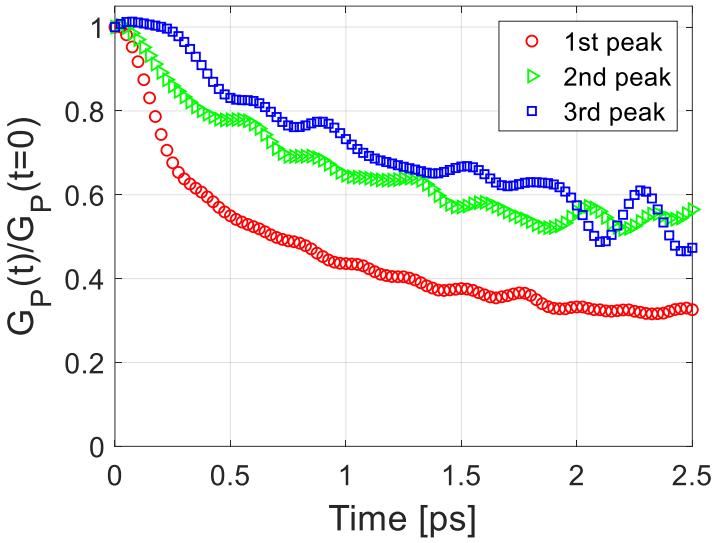

Figure 4.5 Normalized $G_d(r, t)$ peak maxima plotted as a function of time for the first three peaks for $Zr_{80}Pt_{20}$ at T_s + 200 °C.

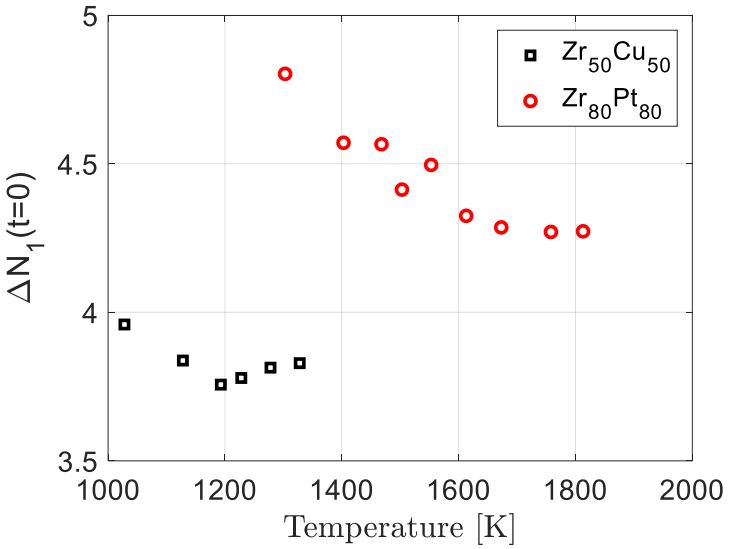

Figure 4.6 $\Delta N_1(t = 0)$ values for $Zr_{50}Cu_{50}$ and $Zr_{80}Pt_{20}$ liquids at different temperatures.

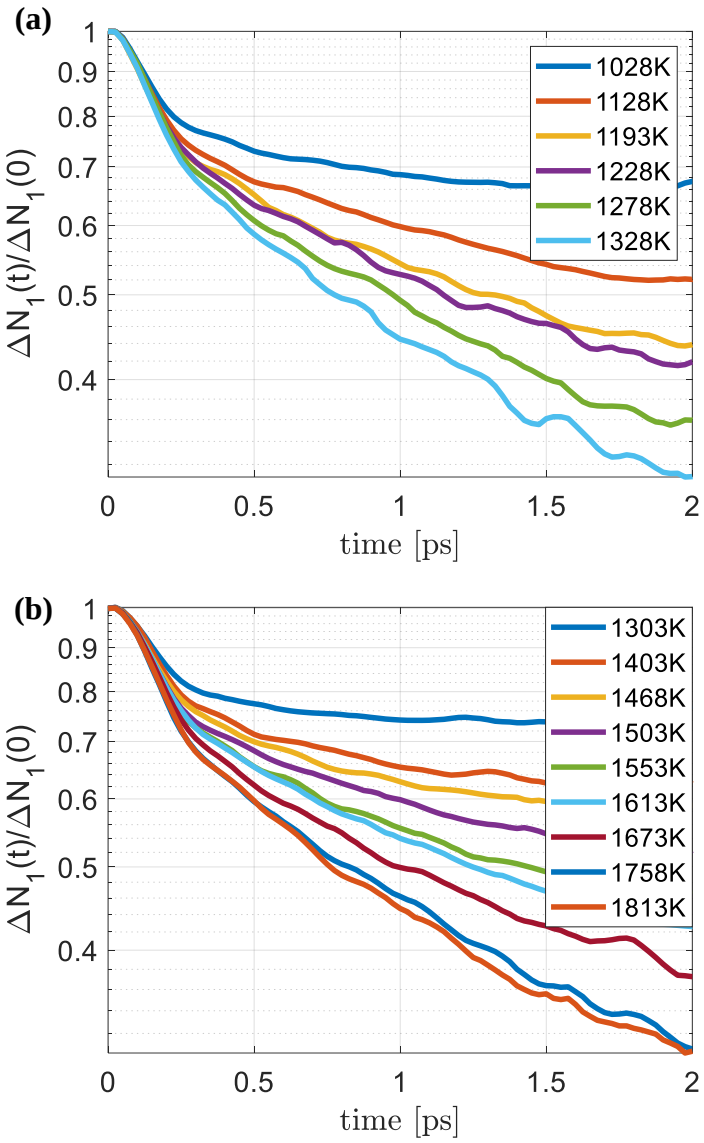

Figure 4.7 Normalized $\Delta N_1(t)$ as a function of time describes the dynamic relaxation in (a) $Zr_{50}Cu_{50}$ and (b) $Zr_{80}Pt_{20}$ liquids at different temperatures.

4.3 Determination of the relaxation times

The two relaxation modes observed from the $\Delta N_1(t)$ curves for $Zr_{50}Cu_{50}$ and $Zr_{80}Pt_{20}$ liquids at each temperature can be fitted to a two-part exponential decay function modified from KWW relationship[47],

$$y(t) = A_1 \exp(-\frac{t}{\tau_1}) + A_2 \exp(-\frac{t}{\tau_2}), \tag{4.3}$$

where A_1 and A_2 are the fitted amplitudes of the two relaxation modes. Hence the characteristic relaxation times of the two relaxation modes, $\tau_1$and τ_2, are determined for $Zr_{50}Cu_{50}$ and $Zr_{80}Pt_{20}$ liquids at all different temperature levels. Before t = 0.1 ps, $\Delta N_1(t)$ almost does not change, partly due to the inaccuracy of the fitted $w(t)$ at short time as mentioned in Section 3.4.3 and shown in Figure 3.13. After t = 1.5 ps, there are some oscillations in the relaxation curve and the relaxation seems too slow as the curve became flat for the lowest temperatures. These are probably artifacts introduced by the over-correction of energy resolution because resolution function $R(t)$ goes to zero quickly after 1.5 ps. Although imperfect, the energy resolution correction technique is still worthwhile to obtain more realistic relaxation times. Therefore, only data from 0.1 to 1.5 ps will be used for the two-part exponential decay function fitting.

The fitting for the normalized $\Delta N_1(t)$ curves for $Zr_{50}Cu_{50}$ and $Zr_{80}Pt_{20}$ liquids at different temperatures is shown in Figure 4.8 and the results are listed in Table 4-1. It is obvious that the fitting between 0.1 and 1.5 ps is very good and the relaxation slows down with decreasing temperature. The determined relaxation times of the two relaxation modes, $\tau_1$and τ_2, for $Zr_{50}Cu_{50}$ and $Zr_{80}Pt_{20}$ liquids at all different temperatures are plotted with inverse temperature, 1000/T, as in Figure 4.9. The error bars for many points are smaller than the symbol size. The activation energies, E_a, for $\tau_1$and τ_2 are determined by $\tau = \tau_0 \exp(E_a / k_B T)$ and plotted in Figure 4.9.

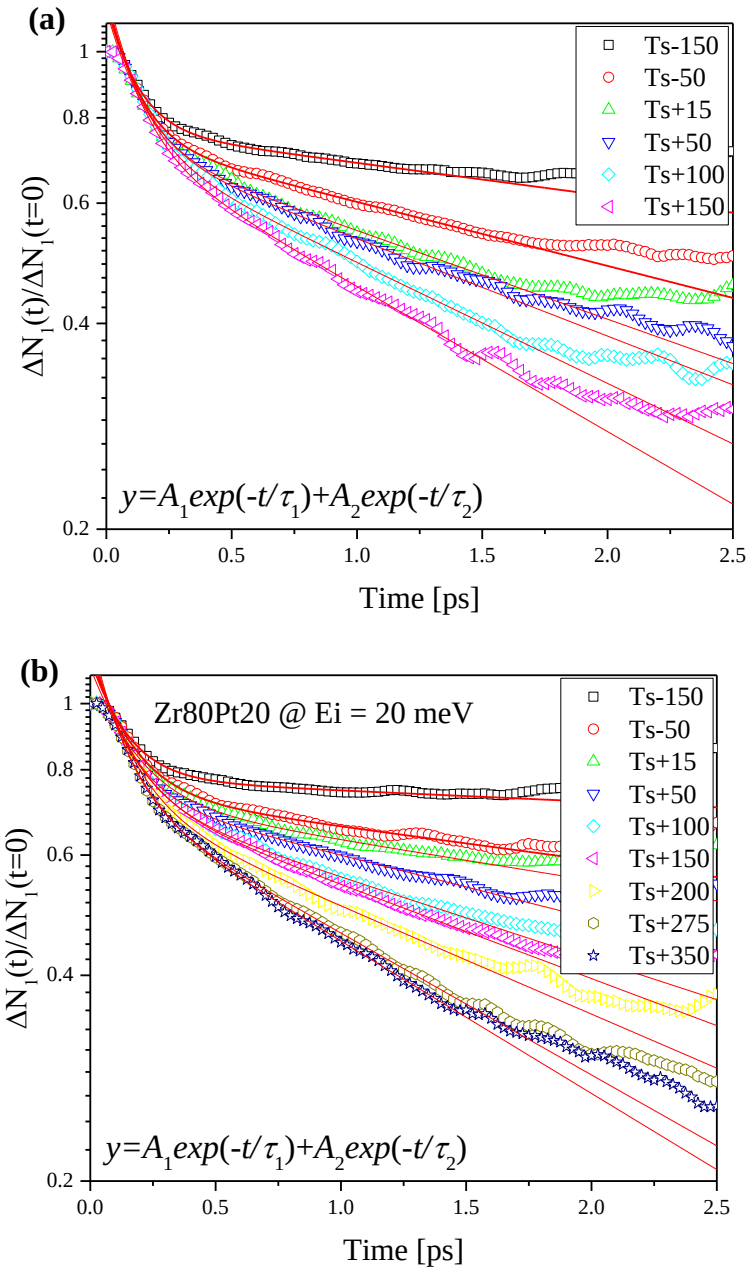

Figure 4.8 Fitting of the normalized $\Delta N_1(t)$ curves with the two-part exponential function for the two relaxation modes in (a) $Zr_{50}Cu_{50}$ and (b) $Zr_{80}Pt_{20}$ liquids at different temperatures.

Table 4-1 Results for the fitting of normalized $\Delta N_1(t)$ curves with the two-part exponential function for $Zr_{50}Cu_{50}$ and (b) $Zr_{80}Pt_{20}$ liquids at different temperatures.

Sample	T (K)	A_1	A_1_err	τ_1 (ps)	τ_1_err	A_2	A_2_err	τ_2 (ps)	τ_2_err
$Zr_{50}Cu_{50}$	1028	0.403	0.013	0.112	0.004	0.769	0.002	8.923	0.278
	1128	0.455	0.012	0.113	0.003	0.747	0.002	4.639	0.054
	1193	0.413	0.022	0.127	0.008	0.737	0.005	3.348	0.077
	1228	0.440	0.020	0.127	0.007	0.739	0.005	3.047	0.058
	1278	0.492	0.016	0.122	0.005	0.739	0.004	2.454	0.029
	1328	0.461	0.019	0.125	0.007	0.738	0.005	2.047	0.030
$Zr_{80}Pt_{20}$	1303	0.389	0.012	0.135	0.006	0.775	0.004	26.500	3.506
	1403	0.433	0.015	0.152	0.007	0.740	0.005	8.807	0.453
	1468	0.406	0.010	0.168	0.007	0.724	0.005	7.322	0.302
	1503	0.462	0.015	0.132	0.005	0.742	0.004	4.691	0.104
	1553	0.459	0.014	0.143	0.006	0.734	0.005	3.629	0.079
	1613	0.447	0.011	0.142	0.005	0.746	0.004	3.154	0.047
	1673	0.484	0.012	0.144	0.005	0.727	0.005	2.746	0.044
	1758	0.521	0.015	0.122	0.004	0.744	0.004	2.092	0.022
	1813	0.486	0.019	0.130	0.007	0.750	0.006	1.948	0.029

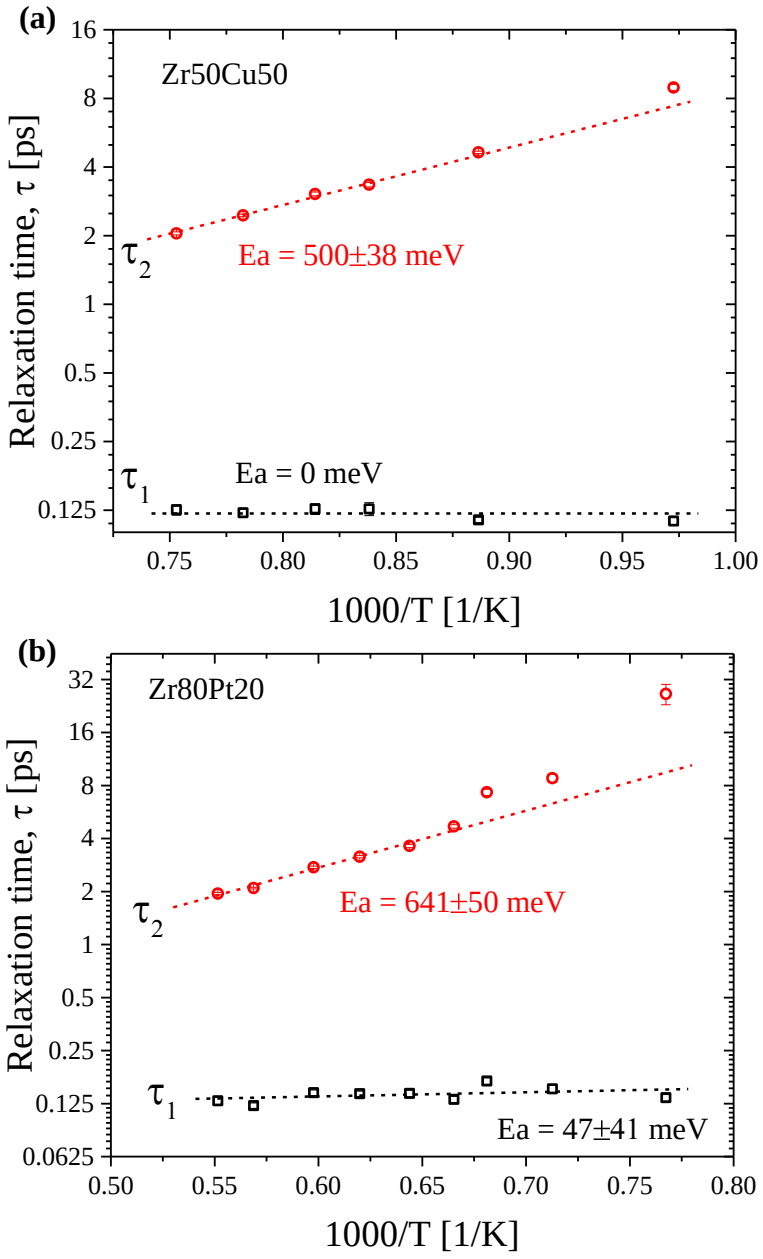

Figure 4.9 Relaxation time, $\tau_1$and τ_2, obtained for (a) $Zr_{50}Cu_{50}$ and (b) $Zr_{80}Pt_{20}$ liquids from the two-part exponential function fitting.

For the faster relaxation mode, τ_1 is small and less temperature dependent with an activation energy of about 0 for $Zr_{50}Cu_{50}$ and 47 meV for $Zr_{80}Pt_{20}$, indicating a ballistic motion of individual atoms at short time. Whereas for the slower relaxation mode, τ_2 is much larger and more temperature dependent with an activation energy of about 500 meV for $Zr_{50}Cu_{50}$ and 641 meV for $Zr_{80}Pt_{20}$, indicating the collective motion of the atoms or correlation dynamics of the system. It is noted that E_a for τ_2 determined in this work is about 2~3 times of that determined in the MD simulation[33], which may be due to the inaccuracy of the potential profiles used in the simulation and shows the significance of studying this topic through inelastic neutron scattering experiment.

4.4 Relation between τ_{LC} and τ_M

The local connectivity change time, τ_{LC}, is the lifetime of the local atomic connectivity change based on atomic bond cutting and reforming, i.e., the time for a center atom to lose an existing neighbor atom or gain a new one. Although it cannot be directly measured through experiment, it must be tightly related to τ_2 since τ_2 is the relaxation time for slow mode of $\Delta N_1(t)$, which depicts the collective motion of atoms in the first nearest neighboring shell. Thus τ_{LC} can be estimated from τ_2. Based on the MD simulation results[56, 58], τ_2 is about (4.1~4.4)τ_{LC} for Fe liquids at different temperatures and τ_2 is about 3.7τ_{LC} for $Zr_{80}Pt_{20}$ liquid. To be simple and averagely, we can claim that τ_{LC} can be estimated to be about one quarter of τ_2, universally for common metallic liquids. If we assume that this relationship still holds for our experimental data, we can calculate τ_{LC} from the above experimentally determined τ_2 values.

On the other hand, the Maxwell relaxation time, τ_M, can be calculated from the viscosity η measured using the oscillation method [4]for the same metallic liquids at the same temperatures for INS experiments, based on the Green-Kubo relationship $\tau_M = \eta / G_\infty$. And its activation energy

is 630 meV for $Zr_{50}Cu_{50}$. Then τ_M and τ_{LC} are compared as functions of inverse temperature for $Zr_{50}Cu_{50}$, as shown in Figure 4.10. The τ_{LC} seems to show Arrhenius behavior for the experimental temperature range, meanwhile, τ_M shows Arrhenius behavior above T_A (1284 K, 1000/ T_A = 0.78 in Figure 4.10) and super-Arrhenius below T_A. Since τ_{LC} is one quarter of τ_2, it has the same activation energy. The slope (activation energy) for τ_M and τ_{LC} are close, which indicates that the energy barrier and physical mechanism behind these two timescales are the same. The ratio of τ_M/τ_{LC} for $Zr_{50}Cu_{50}$ and $Zr_{80}Pt_{20}$ as a function of the temperature reduced by their respective T_A are plotted in Figure 4.11. At high temperatures above T_A, $\tau_M \approx \tau_{LC}$, while at low temperatures below T_A they are no longer equal ($\tau_M > \tau_{LC}$). Comparing the result with the MD simulation results in [33], as shown in Figure 4.12, it is apparent that they share the very similar trend, although the temperature range measured in INS experiment is much narrower than that of MD simulation, due to the metallic element evaporation problem, heating capacity limit of lasers used in the levitator and crystallization under deep supercooling. It is also noted that the ratio of τ_M/τ_{LC} for simulated liquid systems is slightly smaller than the experimentally determined value at lower temperatures, which is quite reasonable because for MD simulation the viscosity is, and thus τ_M, calculated from Green-Kubo relation is always underestimated at low temperatures as the integrand in Equation 2.3 does not easily go to zero within the simulation time at low temperatures.

This coincidence between experimental data and simulation results provides direct experimental support for the claim from MD simulation that the viscosity of metallic liquids is controlled by the local atomic connectivity change at high temperatures above the crossover temperature T_A.

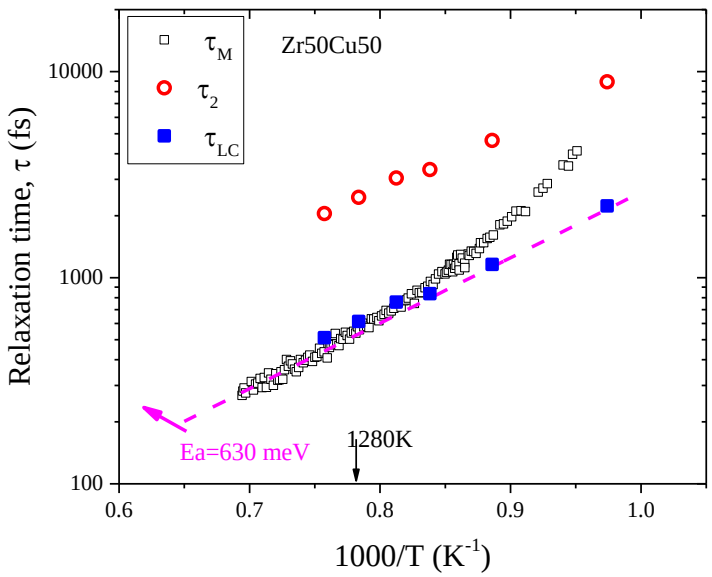

Figure 4.10 Comparison of τ_M and τ_{LC} for $Zr_{50}Cu_{50}$ liquid at different temperatures.

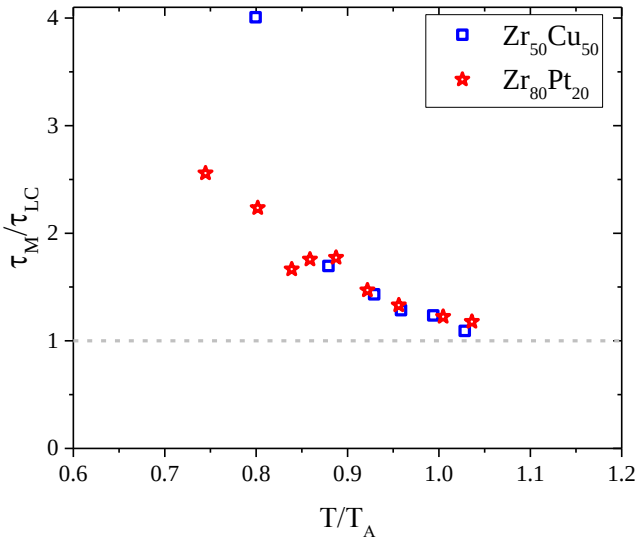

Figure 4.11 The ratio of τ_M/τ_{LC} as a function of temperature normalized by T_A for $Zr_{50}Cu_{50}$ and $Zr_{80}Pt_{20}$ liquids.

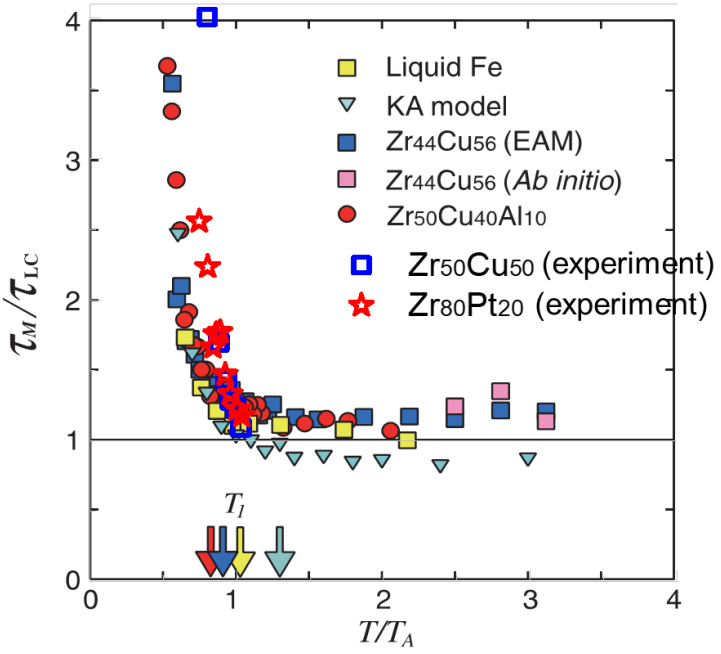

Figure 4.12 The ratio of τ_M/τ_{LC} obtained from INS measurements for $Zr_{50}Cu_{50}$ and $Zr_{80}Pt_{20}$ liquids compared with MD simulation results for various metallic liquid models.

4.5 Self-motion of atoms in metallic liquids

The self-part of VHF, $G_s(r, t)$, obtained from INS experiment in 3.4.5,can be used to analyze the self-motion of atoms or diffusion behavior in the metallic liquids. The self-part of VHFs below 1.5 Å are analyzed using the Gaussian approximation[57]:

$$G_s(R,t) = \frac{C(t)}{\rho}\left[\frac{1}{\pi\alpha(t)}\right]^{\frac{3}{2}} \exp[-R^2/\alpha(t)], \quad (4.4)$$

The coefficient $C(t)$ is introduced to handle the deviation from the Gaussian approximation and to compensate for a possible incomplete energy resolution correction. The fitting is shown in Figure 4.13 and fitting results are shown in Figure 4.14 The diffusivity can be estimated based on $\alpha(t)=4Dt$. Tentative attempt was tried to obtain diffusivity and to analyze self-motion of atoms.

4.6 Summary

1) Collective motion of atoms or atomic-level dynamic in metallic liquids can be analyzed based on the experimentally determined distinct part of Van Hove function, $G_d(r, t)$. A new parameter, $\Delta N_1(t)$, was defined and two relaxation modes were observed for the relaxation of $\Delta N_1(t)$. A two-part exponential decay function was applied to fit the relaxation curves and the characteristic relaxation times were determined.

2) The local atomic connectivity change time, τ_{LC}, was estimated from the experimentally determined τ_2, and is equal to the Maxwell relaxation time, τ_M, determined from the measurements of the viscosity for metallic liquids when $T > T_A$. This verified the conclusion from the MD simulation that the viscosity of liquids is controlled by the local atomic connectivity change at temperatures above the crossover temperature T_A.

3) The self-part of Van Hove function, $G_s(r, t)$ was tentatively used to analyze the self-motion of atoms in the metallic liquids.

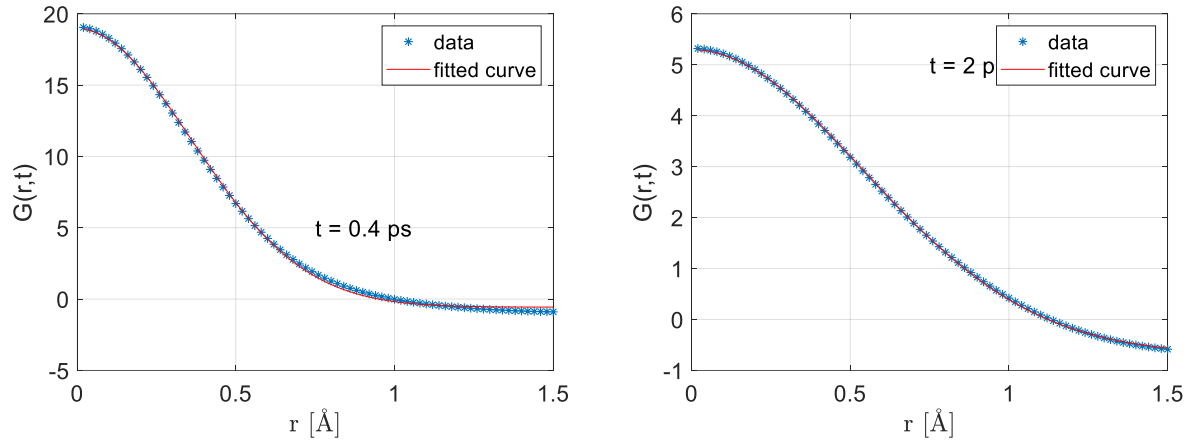

Figure 4.13 Fitting of the self-part of Van Hove function, $G_s(r, t)$, using Gaussian approximation at different time slices.

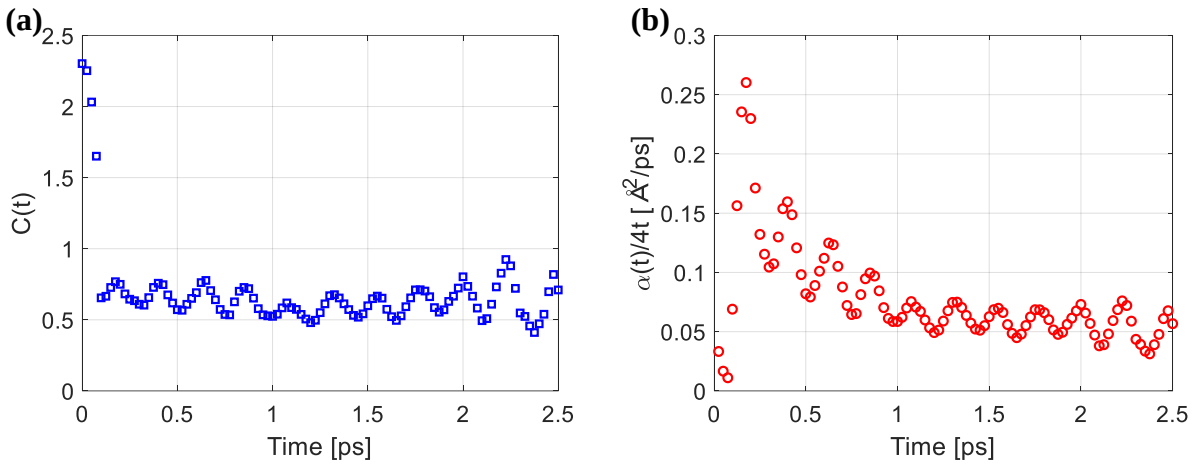

Figure 4.14 The result of fitting $G_s(r, t)$ using the Gaussian approximation: time evolution of (a) $C(t)$ and (b) $\alpha(t)/4t$.

Chapter 5 Thermal Structural Evolution of Two Zr-based Metallic Glasses Studied by High-Energy X-ray diffraction

5.1 Introduction

Extensive research on the metallic glasses (MGs) have been carried out since the discovery of the first amorphous alloy due to their promising mechanical properties like high strength, large elastic limit and excellent corrosion resistance. However, the applications of MGs as promising structural materials are restrained to certain few instances at room temperature mostly due to their poor plasticity and thermal stability[59-68]. Generally, glassy alloys, being metastable, undergo relaxation and devitrification during heating, resulting in the loss of their excellent mechanical properties. However, different kinds of metallic glasses may experience distinct structural evolution during the heating process[69-71]. $Zr_{65}Cu_{17}Ni_8Al_{10}$ is a typical Zr-rich metallic glass [72-74] with good glass-forming ability, outstanding mechanical properties, and typical crystallization phenomenon above glass transition temperature, T_g. $Zr_{80}Pt_{20}$ can form glassy ribbons and attracts lots of attention due to its characteristic five-fold icosahedral quasi-crystalline phase (i-phase) formation, and the effects of different cooling rates, annealing history and oxygen concentration on the formation of i-phase have been studied extensively[75-79].

Based on the difference in the structure of these two metallic glasses, the detailed study of their thermal structural evolution would benefit understanding the structure of metallic glasses and the nature of glass transition and glass-forming ability.

Here we study two different Zr-based metallic glasses, $Zr_{65}Cu_{17}Ni_8Al_{10}$ bulk metallic glass and $Zr_{80}Pt_{20}$ ribbon, to investigate the thermal structural changes on heating. Continuous sets of *in-situ* high-energy X-ray measurements were obtained, and the structural changes were analyzed using structure function and pair distribution function.

5.2 Experimental Methods

Two different kinds of Zr-based metallic glass samples were prepared for this experiment. The bulk metallic glass (BMG) $Zr_{65}Cu_{17}Ni_8Al_{10}$ was prepared by arc melting and suction casting method, while the $Zr_{80}Pt_{20}$ ribbon was prepared by the melt spinning method. Samples were cut to appropriate sizes, polished to remove surface contamination, and then encapsulated in quartz capillaries under secondary vacuum. The *in-situ* high-energy synchrotron X-ray diffraction measurements were carried out at beamline 6-ID-D of Advanced Photon Source, Argonne National Laboratory. The X-ray beam energy was 100.32 keV, corresponding to a wavelength of 0.12359 Å. The measurement was using transmission mode with a 2-D image plate detector being placed about 30 cm downstream the sample to collect the diffraction pattern. A resistance-heated furnace was used to heat the sample in the capillary and the temperature was held at certain levels to collect the diffraction data, with the temperature range from room temperature up to 1000 ^oC. Calibration of beam center position and detector geometrical information was performed by measuring a CeO_2 NIST powder standard.

Correction for beam polarization and dark current, and data integration over the 360^o azimuth angle were applied using the FIT2D software (http://www.esrf.eu/computing/scientific/FIT2D/), to obtain the 1-D intensity vs. 2θ diffraction pattern. After background subtraction and correction for air scattering, Compton scattering, and sample absorption conducted using PDFgetX2 software [80], the total structure function *S(Q)* was acquired with *Q* (scattering vector $Q = 4\pi\sin\theta/\lambda$, where θ is the diffraction angle and λ is the wavelength) upto about 25 $Å^{-1}$. Then the pair distribution function (PDF) was obtained through the direct Fourier transformation according to the following equations:

$$g(r) = 1 + \frac{1}{2\pi^2 r \rho_0} \int_{Q_{min}}^{Q_{max}} Q\left[S(Q) - 1\right] \sin(Qr) dQ \quad (5.1)$$

where ρ_0 is the average number density of the sample.

Classical molecular dynamics (MD) simulation is carried out for $Zr_{80}Pt_{20}$, using LAMMPS software (http://lammps.sandia.gov) [81]. The simulation was conducted with embedded atom method (EAM) potentials (https://sites.google.com/site/eampotentials/) [82] and 16000 atoms were used in the model. The model system is under NPT ensemble with a Nose-Hoover thermostat and external pressure equals to zero. First, the model was equilibrated at high temperature (2500 K) for 0.5 ns to obtain homogeneous liquid, and then quenched to 300 K with a cooling rate of 10^{12} K/s to obtain a disordered structure. Then the system was reheated up to different temperatures and kept for 2 ns for relaxation, in order to imitate the annealing process. The atomic configuration and trajectory data was recorded for PDF and Voronoi analysis.

5.3. Results and Discussions

5.3.1 $Zr_{65}Cu_{17}Ni_8Al_{10}$ BMG

$Zr_{65}Cu_{17}Ni_8Al_{10}$ is a bulk metallic glass with very good plasticity and a glass transition temperature of T_g = 362 °C. The continuous dataset of the total structure functions *S(Q)* at different temperatures from room temperature (RT) up to 960 °C was obtained, as shown in Figure 5.1(a). Three stages with apparently different features in the structure functions are identified during the heating process. First, at low temperatures, the *S(Q)* shows a typical amorphous feature with one main peak at low Q and quickly damped and oscillating about unity. As the temperature increases,

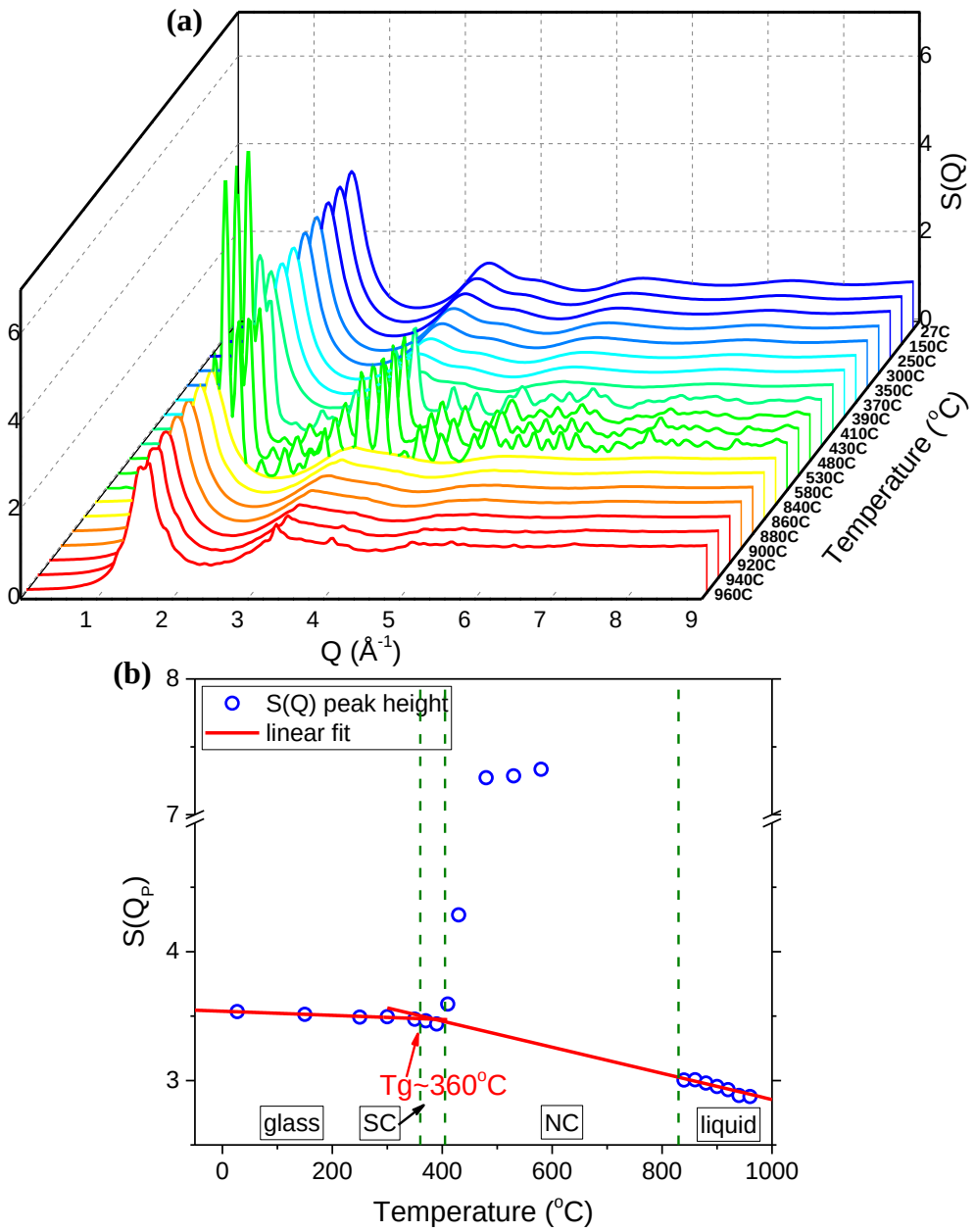

Figure 5.1. (a) Structure function of $Zr_{65}Cu_{17}Ni_8Al_{10}$ at different temperatures and (b) the main peak maximum as a function of temperature. The red lines are linear fitting. Framed text labels correspond to different phases, while SC and NC stands for supercooled liquid and nano-crystalline phase, respectively.

the *S(Q)* shows lots of strong diffraction peaks, featuring the nano-crystalline phase. At further heating to temperature above 840 ^{o}C, the *S(Q)* shows similar features as in glass state, indicating the liquid state. It is noticeable that some spikes show up on the first and second main peaks above 920 ^{o}C, which may be due to the partial oxidization in the sample due to the poor vacuum in the quartz container. To illustrate the phase transitions more accurately, the first main peak maximum of *S(Q)* vs. temperature was plotted in Figure 5.1(b). The first peak maximum $S(Q_1)$ is about 3.6 at room temperature and decreases slightly with temperature in the glass state, and then an obvious change of slope is observed between 350 and 370 ^{o}C, which indicates the passing of glass transition and the formation of the supercooled liquid phase, in good agreement with literature values. The decrease of $S(Q_1)$ indicates the structure of $Zr_{65}Cu_{17}Ni_8Al_{10}$ becomes more disordered with temperature in the glassy and supercooled liquid states. Then an abrupt increase of $S(Q_1)$ occurs at about 410 ^{o}C, indicating the onset of nano-crystallization and the ordering of the structure. At 840 ^{o}C, the $S(Q_1)$ decreased to about 3.2 as the sample melts and continues decreasing as the temperature of the liquid increases. Linear fitting is applied to the data points of the liquid phase above 840 ^{o}C (the last two points are with excluded from fitting due to the partial oxidization). The fitting is extrapolated to lower temperatures and it is in good agreement with the data points form supercooled liquid state and meets the fitting of glassy state data around T_g, confirming that the supercooled liquid state possesses very similar average structures with the liquid phase and that they follow the same structural ordering-temperature relationship. According to the definition of structural fragility index, $Zr_{65}Cu_{17}Ni_8Al_{10}$ has the fragility index of almost zero and can be classified as a relatively strong glass[83].

Figure 5.2(a) and (b) shows the PDFs for $Zr_{65}Cu_{17}Ni_8Al_{10}$ at different temperatures. Apparently, there are three different stages: the glass state, the nano-crystalline state, and the liquid state. Below 410 ^oC, it is hard to distinguish the supercooled liquid phase from the glass just based on the PDF due to the highly similar structure between them. Also, the PDF of the glassy state is very similar with that of the liquid state except that the former shows apparent first peak splitting feature while there is no obvious splitting but a broadening in the latter, which may be due to additional thermal excitations (high atomic mobility or disappearance of specific atomic pairs) in the liquid at high temperatures. It is noted that the primary PDF peak for nano-crystalline phase is similar with that of glass and supercooled liquid while more peaks erect after the first peak, indicating that the nano-crystalline phase possesses similar short-range order (nearest neighbor atoms) with the glass and supercooled liquid while different medium or long-range order shows up in nano-crystalline phase.

Figure 5.2(c) shows the centroid of the first main peak for $Zr_{65}Cu_{17}Ni_8Al_{10}$ as a function of temperature. While in Figure 5.1(b), the $S(Q_1)$ trend suggesting similar structural order in the supercooled liquid and liquid sates, here the peak centroid shows obvious difference in the liquid and supercooled liquid states. This reminds that too much weight was putting on the structure function when analyzing the structure of metallic glass, and $g(r)$ from real space should be considered more to provide supplemental structural information.

To further analyze the structural details, the PDF main peaks were fitted to discern different atomic pairs[84]. Instead of the original $g(r)$, the modified one $4\pi r\rho(r)$ of the primary peak was fitted because it is more Gaussian-like. As shown in Figure 5.3, two Gaussian functions were used to fit the primary peak from 2 to 4 Å and the fitting produced a very good agreement to the peak profile. At room temperature (27 ^oC), the first subpeak at 2.68 Å corresponds to a mixture of Zr-Cu, Zr-Ni and Zr-Al atomic pairs, the second subpeak at 3.14 Å corresponds to the Zr-Zr pairs.

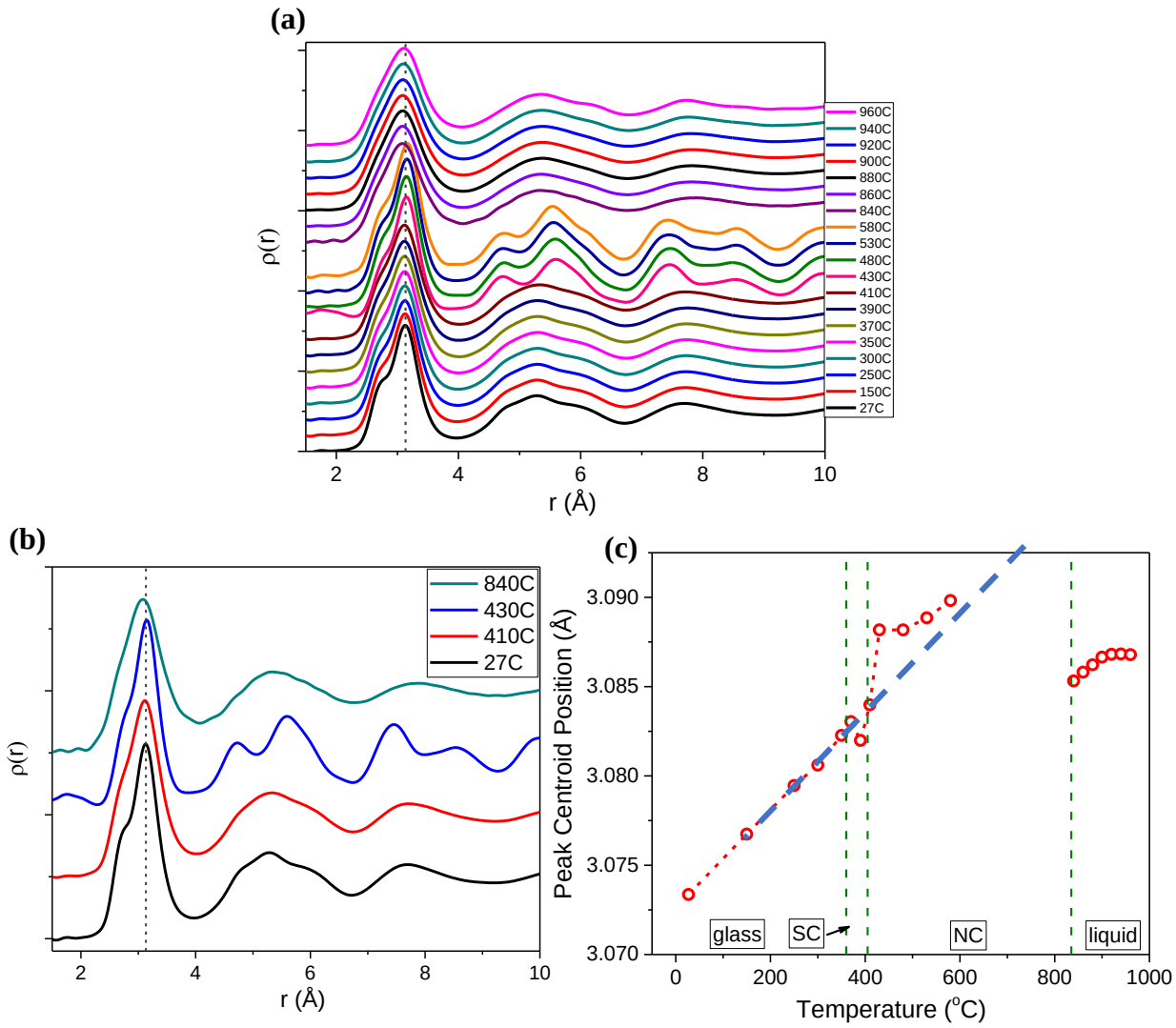

Figure 5.2 (a) PDFs for $Zr_{65}Cu_{17}Ni_8Al_{10}$ at different temperatures plotted with offset for clarity. Dash line indicates the position change of the first peaks. (b) PDFs at selected temperatures. (c) Centroid of the first main peak as a function of temperature.

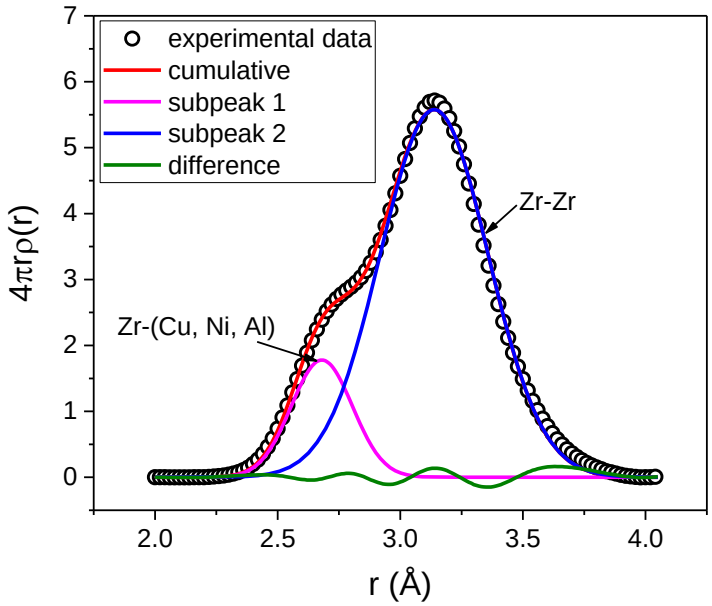

Figure 5.3 Fitting of the main PDF peak with two Gaussian functions to discern different atomic pairs for $Zr_{65}Cu_{17}Ni_8Al_{10}$ at 27 ^{o}C.

Based on the sums of Goldschmidt atomic radii, r_{Zr}=1.60 Å, r_{Cu}=1.28 Å, r_{Ni}=1.24 Å, and r_{Al}=1.43 Å, the calculated interatomic distances are 3.20 Å for atomic pair Zr-Zr, which is very close to the subpeak 2 position, and 2.84 Å, 2.88 Å and 3.03 Å for Zr-Ni, Zr-Cu and Zr-Al atomic pairs, respectively, which are larger than the subpeak 1 position but quite reasonable due to the highly negative mixing enthalpy among these elements (-49, -29 and -44 kJ/mol for Zr-Ni, Zr-Cu and Zr-Al pairs, respectively).

Through the Gaussian fitting, the peak positions, maximum heights, peak width (FWHM) and areas of the first two subpeaks from the primary peaks are obtained for $Zr_{65}Cu_{17}Ni_8Al_{10}$ at different temperatures, as shown in Figure 5.4. Emphasis is only put on the subpeak position and area during the glass and liquid state here, which describe the atomic pair distance and population of the pairs, respectively. The subpeak 1 position (Zr-M pairs distance, M = Ni, Cu, Al) decreases with temperature in the glassy state, then there is an increase of the slope in the supercooled liquid region above the glass transition, as well as subpeak 2 (Zr-Zr pairs). This decrease is in contrast to the macroscopic thermal expansion. After the sample is nano-crystallized, the subpeak positions are changed a lot, indicating that the structure and short-range order are very different from the glass and supercooled liquid. The peak area (Figure 5.4d) is positively related to the partial coordination number (CN) for different atomic pairs in the first shell. The population of Zr-Zr pairs is increasing while the Zr-M pairs are decreasing with temperature in the glass state and supercooled liquid state. These suggests that during the glass and supercooled liquid states, there is competing between the chemical short-range order (CSRO) and topological short-range order (TSRO), and that CSRO becomes dominant and overwhelms TSRO during the temperature increase through the development of Zr-Zr pairs by local atomic rearrangements.

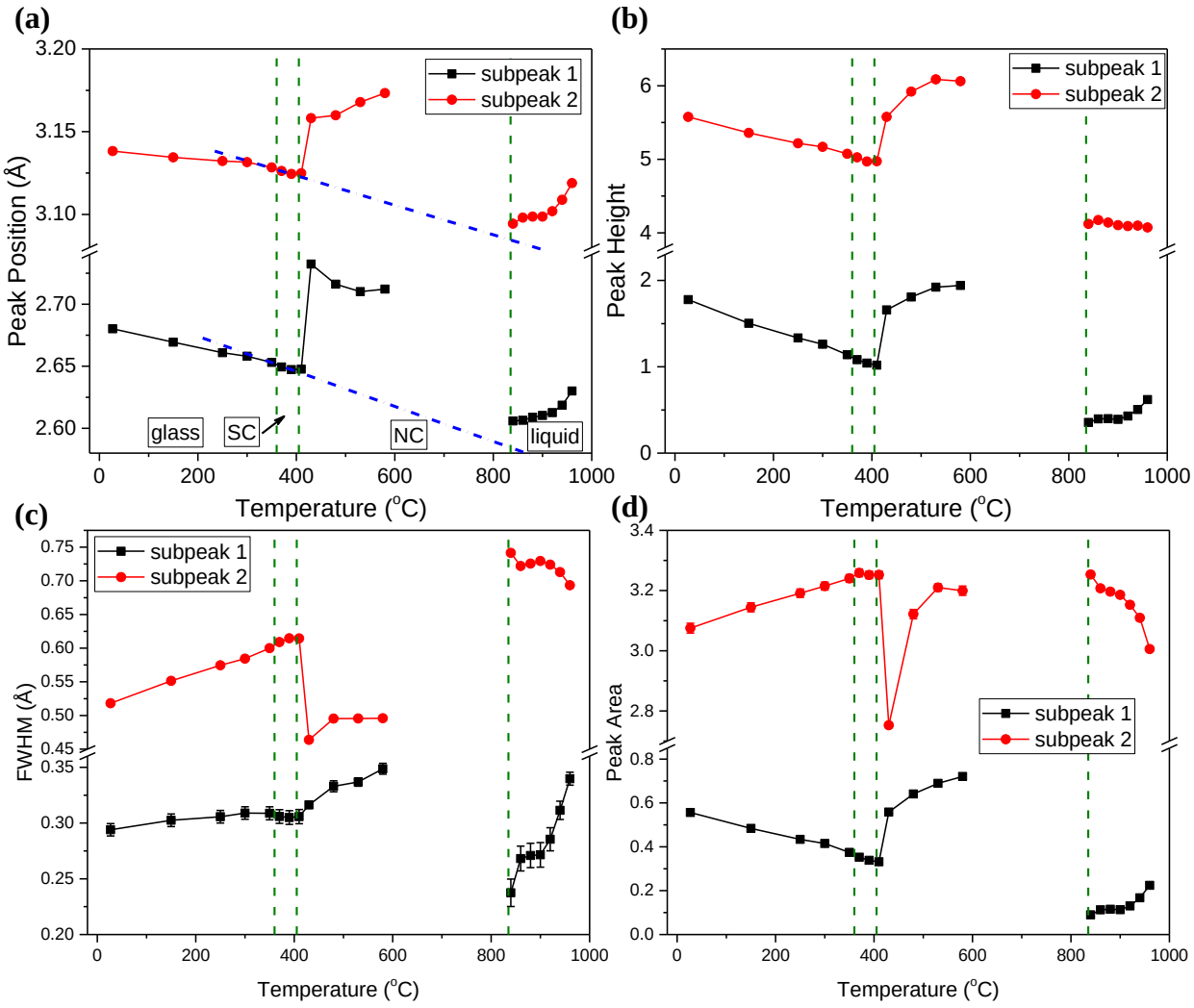

Figure 5.4 Subpeak position, height, FWHM and area as a function of temperature for $Zr_{65}Cu_{17}Ni_8Al_{10}$. Vertical dash lines indicate the glass transition, crystallization and liquidus temperatures. Blue dash dot lines in (a) are extrapolation from supercooled liquid to the melt.

5.3.2 $Zr_{80}Pt_{20}$ ribbon

The structure function and its first maximum for $Zr_{80}Pt_{20}$ sample at different temperatures are shown in Figure 5.5. For comparison, the diffraction pattern of as cast sample and a sample pre-annealed at 580 ^{o}C were also measured without the furnace. There are three apparent stages with different features within the temperature range. At low temperatures, the structure function shows typical features of amorphous solid with broad first and second peaks while there is a shoulder on the high *Q* side of the second peak. A small pre-peak at low *Q* of about 1.7 $Å^{-1}$ is present, which is indicating the chemical ordering in $Zr_{80}Pt_{20}$ glass. With the temperature increasing, the first peak position moves to higher *Q* direction, while the second peak goes to lower *Q* direction and becomes more prominent. In addition, the shoulder on the second peak becomes more pronounced and becomes a well-defined new peak. These features are attributes of icosahedral quasicrystalline phase (i-phase), which will be further discussed later. When the temperature is above 570 ^{o}C, prominent Bragg reflections indicate that the sample is nano-crystallized, which may be attributed to nano-Zr_5Pt_3 phase. The sample pre-annealed at 580 ^{o}C is still a quasicrystal while the in-situ measurement shows that the sample is nano-crystallized at 570 ^{o}C, which may be due to the accumulative thermal effect in the *in-situ* step-like measurement.

To further confirm the transition and determine the transition temperatures, the first maximum $S(Q_1)$ of the structure function is plotted vs. temperature as shown in Figure 5.5(c). In the glassy state the peak height $S(Q_1)$ decreases slightly and then increases abruptly when quasicrystallization occurs in the sample. The respective linear fittings for glass and quasicrystal stage cross at the temperature of about 430 ^{o}C, which signifies the onset temperature of quasicrystallization. Above 570 ^{o}C, the $S(Q_1)$ decrease suddenly due to the nano-crystallization. The $S(Q_1)$ for the 580 ^{o}C pre-

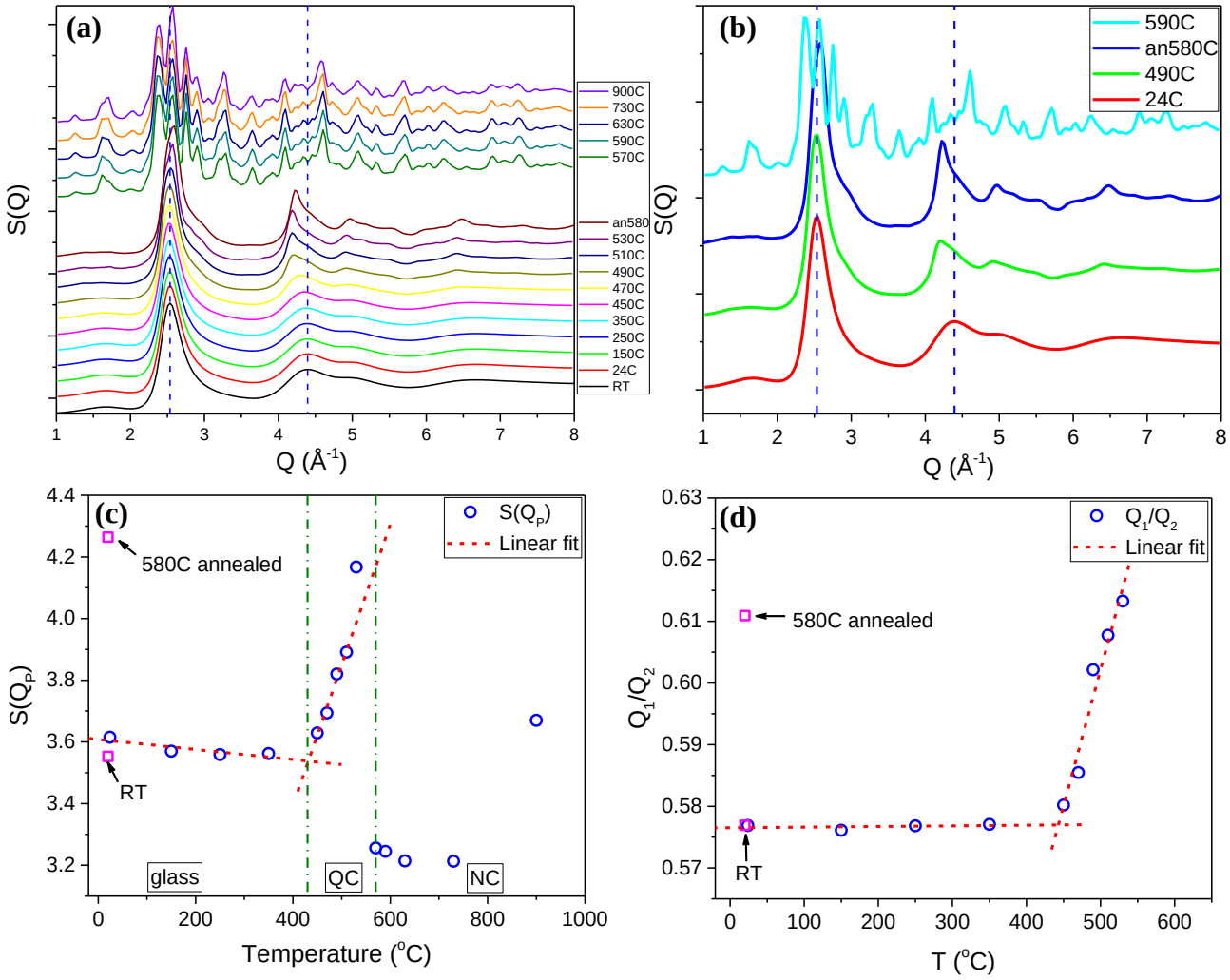

Figure 5.5 Structure function (a,b), its first maximum (c) and ratio of first and second peak position (d) as a function of temperature for $Zr_{80}Pt_{20}$.

annealed sample is in good agreement with the extrapolation of those for the quasicrystal region, indicating it is still quasicrystal phase as discussed above.

The ratio of the first and second maximum position Q_1/Q_2 (as shown in Figure 5.5d) is almost constant with the temperature in the glassy state and increases rapidly to 0.613 at 530 ^{o}C, further confirming that the transition here is quasicrystallization[85, 86]. The linear fitting provides a transition temperature of about 440 ^{o}C, in good agreement with the transition temperature obtained above from the $S(Q_1)$ fitting.

The PDFs for $Zr_{80}Pt_{20}$ obtained from the Fourier transformation of $S(Q)$ at different temperatures are shown as Figure 5.6(a). At room temperature, the two components of the first main peak are evident, and the preferred component shifts from the low-r side one to the high-r side one as the temperature increases and the quasicrystallization occurs in the sample. During the nanocrystalline stage, the low-r side component becomes more prominent again while more peaks arise. Figure 5.6(c) plots the relationship between the first main peak centroid and temperature. Similar to $Zr_{65}Cu_{17}Ni_8Al_{10}$, the peak centroid increases with T during glass state. However, the abrupt increase happens in the quasicrystalline state, followed by a slight decrease in nanocrystalline phase, in $Zr_{80}Pt_{20}$, while in $Zr_{65}Cu_{17}Ni_8Al_{10}$ the abrupt increase happens in nanocrystalline state.

Also, the first main peak of the $4\pi r\rho(r)$ for $Zr_{80}Pt_{20}$ is fitted with two Gaussian functions, and the subpeak properties such as peak position, peak height, FWHM and integrated area are plotted as in Figure 5.7. According to the peak position and Goldschmidt atomic radius, r_{Pt}=1.39 Å, we speculate that the first subpeak corresponds to Pt-Pt or Pt-Zr pairs and the second peak corresponds to the Zr-Zr pair. The pair distances for subpeak 1are much smaller than the sum of corresponding atomic radii sum because of the very highly negative mixing enthalpy (-100 kJ/mol) for the Pt-Zr pair. (1) In the glassy state, peak positions for both subpeak 1 and subpeak 2 keep almost constant

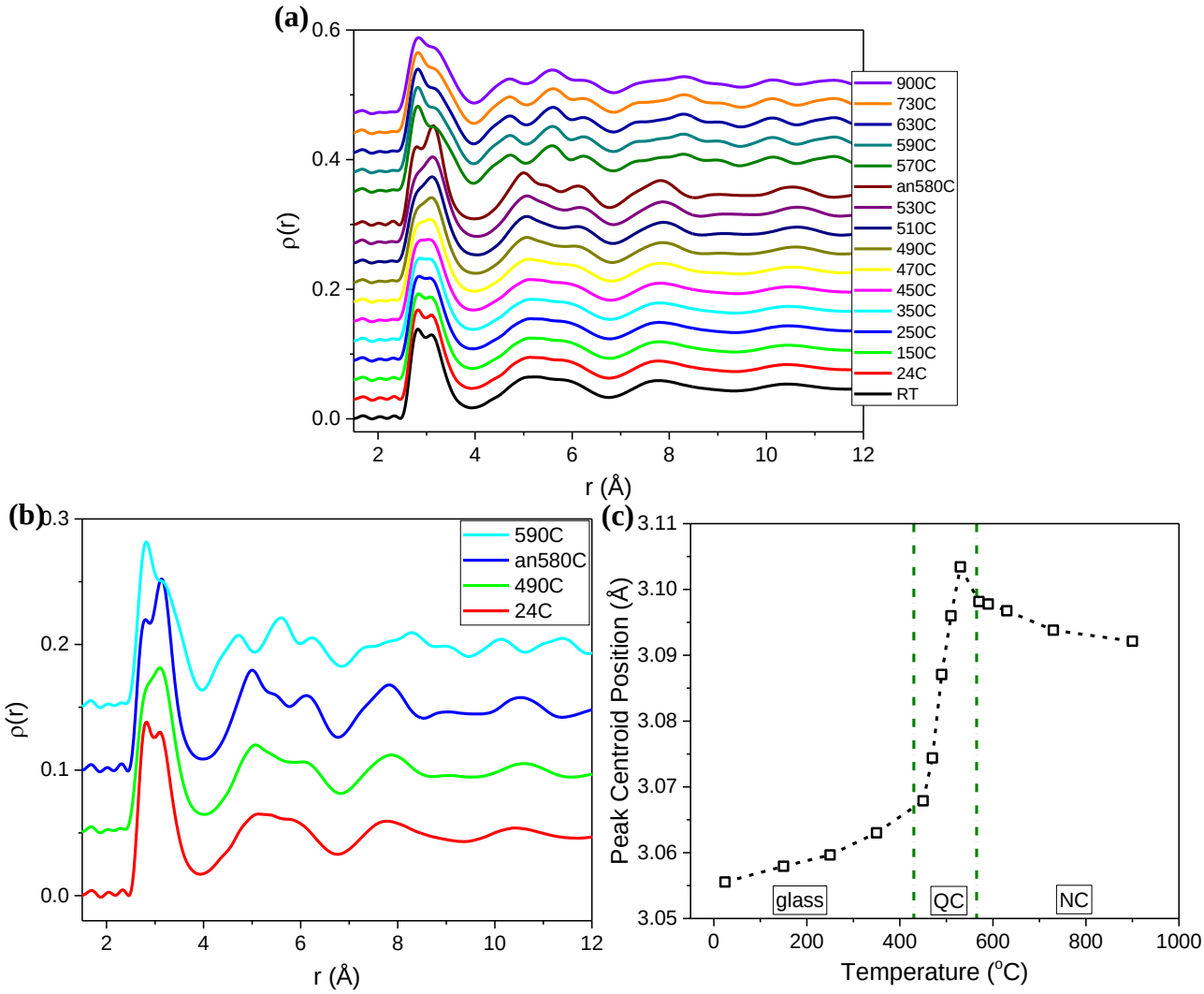

Figure 5.6 (a) PDFs for $Zr_{80}Pt_{20}$ at different temperatures; (b) main peak centroid position as a function of temperature.

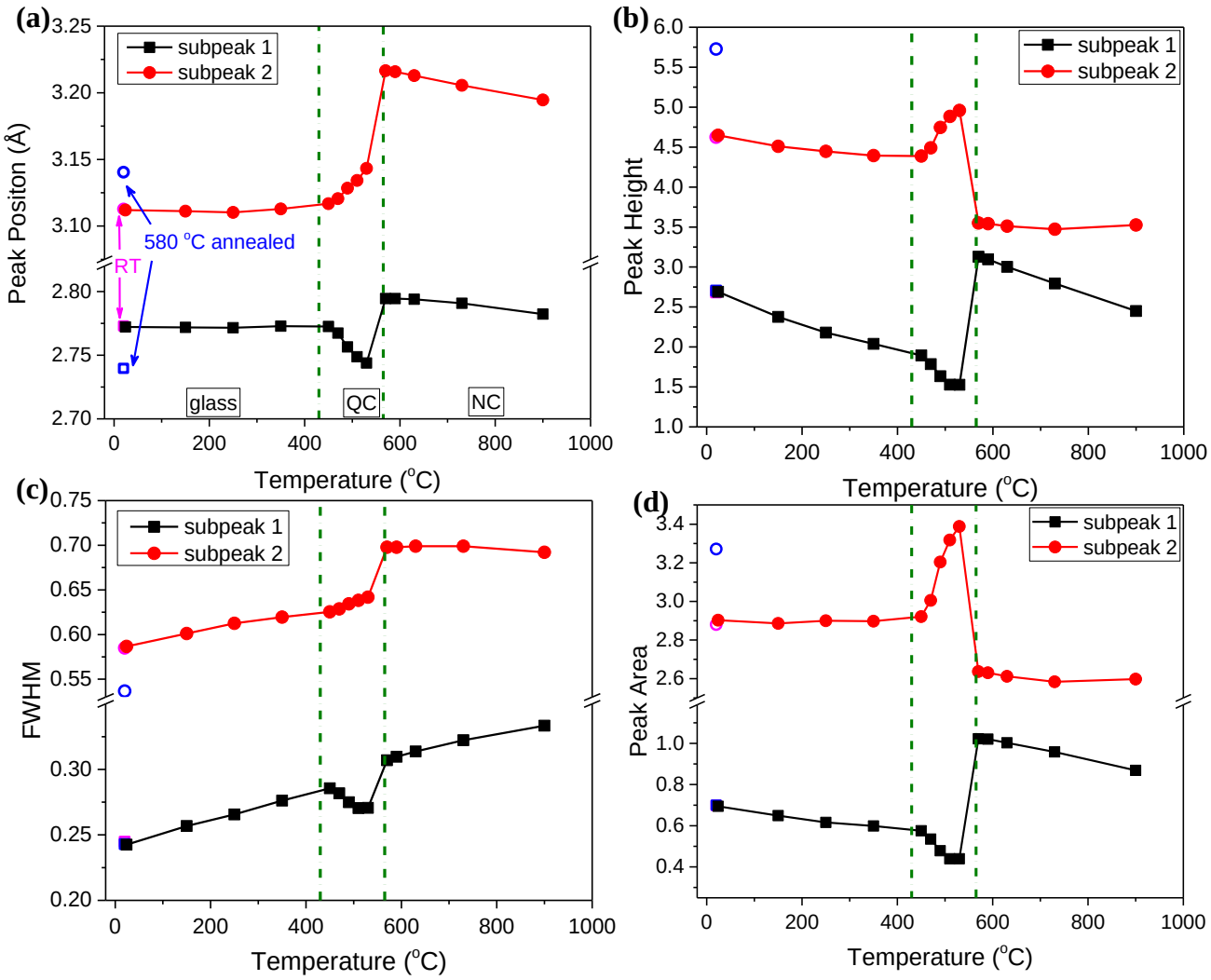

Figure 5.7 Subpeak position, height, width and area for $Zr_{80}Pt_{20}$ as a function of temperature. Vertical dash dot lines indicate the transition temperatures for quasicrystallization and nano-crystallizaiton. The hollow shapes are for the RT and pre-annealed samples.

with temperature, which is different from $Zr_{65}Cu_{17}Ni_8Al_{10}$. Therefore, there is a compromise between the CSRO and TSRO in glassy $Zr_{80}Pt_{20}$. The peak area, which is closely related to the partial coordination number, decreases slightly for Pt-based pairs while remains almost constant for Zr-Zr pairs. (2) In the quasicrystalline phase above 430 ^{o}C, apparent transitions are observed for all the subpeak properties. Pt-based pair distance decreases greatly with temperature while Zr-Zr pair distance increases greatly. Also, the subpeak area, or population of atomic pairs, decreases significantly for Pt-based pairs but increases strongly for Zr-Zr pairs, showing that the Zr-Zr pairs are much preferred in the quasicrystalline phase.

For a long time, it is claimed that when quenching from liquid, the strong chemical affinity of Pt-Zr atomic pair in $Zr_{80}Pt_{20}$ may help the inheritance of icosahedral short-range order (ISRO) from the liquid to the glass and contribute to the stabilization of ISRO and inhibition of stable crystalline phase with long-range order, which is important in the formation of the quasicrystalline i-phase[85-89]. But here, we show that when heating up from the glassy $Zr_{80}Pt_{20}$, Zr-Zr pairs may promote the ISRO and formation of the i-phase and impede the crystallization. Therefore, besides the Pt-Zr pairs, Zr-Zr pair is also significant in the ISRO and the formation of i-phase. Comparing with thermal structure change of $Zr_{65}Cu_{17}Ni_8Al_{10}$, it is demonstrated that different topological and chemical effects of the different atomic pairs in these two kinds of metallic glasses determines their distinct thermal structural evolution behaviors.

5.4 MD simulation for $Zr_{80}Pt_{20}$

Configurational PDF was calculated from the atomic trajectories and *S(Q)* was obtained by Fourier transformation of *G(r)*. Also, the partial structure functions $S_{\alpha\beta}(Q)$ for different atomic

pairs were obtained, as shown in Figure 5.8. According to Faber-Ziman definition [90], the structure factor for a binary system is a weighted sum of three partial structure factors:

$$w_{ij} = \frac{c_i c_j f_i(Q) f_j(Q)}{\langle f \rangle^2} \tag{5.2}$$

$$S(Q) = \sum_{i,j} w_{ij} S_{ij}(Q) \tag{5.3}$$

where c_i and f_i are the atomic concentration and the Q-dependent atomic scattering factor for atom species i, respectively. Then the weighted total PDF can be obtained through the Fourier transformation of the weighted $S(Q)$. However, the weighting factors vary slowly with Q when compared with $S(Q)$, so the following approximation is applicable:

$$w_{ij} = \frac{c_i c_j Z_i Z_j}{\langle Z \rangle^2} \tag{5.4}$$

where Z_i is the atomic number of atom i. Comparison shows that there is only a small and negligible difference between the $g(r)$ obtained from the weighted $S(Q)$ with a Q-dependent w_{ij} and approximated w_{ij}.

Figure 5.8(a) compares PDFs from MD simulation results with experimental data. At RT, the MD result does not reproduce the experimental one very well, however at higher temperature (770 K), the difference between MD and experimental data is very small, indicating that the model system is more liquid-like and cannot depict the local orders in the glass very well. PDFs at different temperatures are plotted in Figure 5.8(b). The liquid-like $g(r)$ changes gradually with temperature and does not reveal the quasicrystalline and nanocrystalline phases. The main peak maximum position skews towards the right (longer distance side) below 870 K like normal thermal expansion but shifts towards the left above 870 K. The former shift is consistent with the peak centroid rightward shift of the experimental data, which is due to increasing asymmetry of the peak

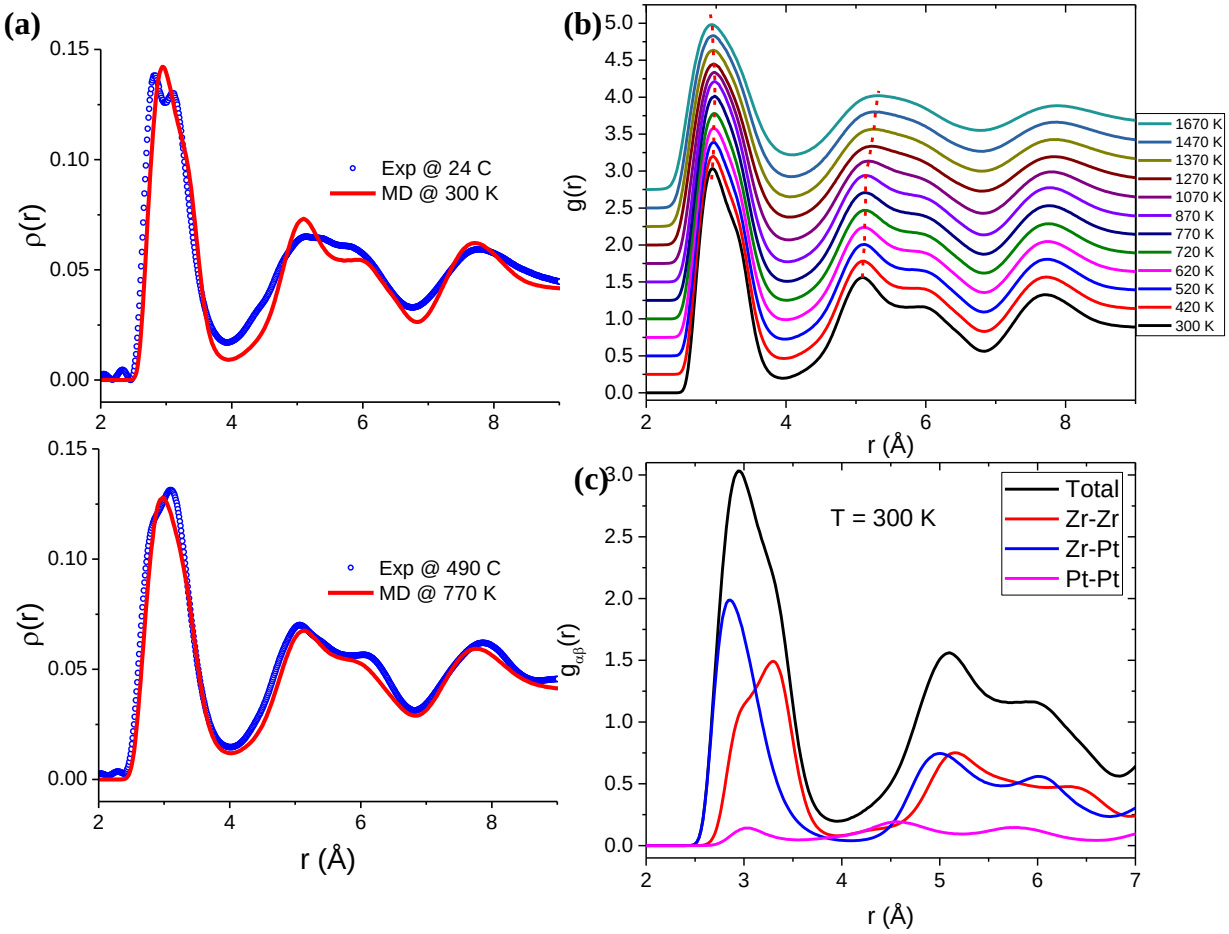

Figure 5.8 PDFs for $Zr_{80}Pt_{20}$ from MD simulation: (a) comparison with experimental data; (b) PDFs at different temperatures; (c) total and partial PDFs at 300 K.

shape and asymmetric redistribution of neighboring atoms besides the topological or chemical short-range ordering. However, the second and third peak maximum positions shift towards the longer distance monotonously and the shoulder on the right side of the second peak merges gradually with the second main peak. Figure 5.8(c) plots the total and partial PDF for $Zr_{80}Pt_{20}$ at 300K. Notably, the partial PDF for Pt-Pt pair has the first main peak at 3.04 Å, which is much larger than the sum of Goldschmidt atomic radius, 2.78 Å, indicating that Pt atoms are not closely packed with other Pt atoms. Pt-Zr pairs have a peak at distance of 2.86 Å, smaller than the atomic radii's sum, due to the strong bonding between Zr and Pt atoms. Zr-Zr pairs have an asymmetric peak with two subpeaks at 2.95 Å and 3.30 Å, showing that there may be two kinds of Zr-Zr pairs in the first shell.

Figure 5.9(a) plots the total and partial *S(Q)* obtained from MD simulation and compares with the experimental results. It is noted that the MD simulation reproduces the main features of the experimental *S(Q)*, including the pre-peak before the main peak, which is from the medium range order (MRO) for Pt-Pt pairs and the reason that Pt-Pt pair distance is larger than sum of atomic radius. However, the intensities of the first, second peak and the shoulder are higher than the experimental result, suggesting that the model structure is less disordered than the real glass structure (perhaps more icosahedra clusters). As the simulation temperature increases, the *S(Q)* becomes more liquid-like: the first and second peak become lower and broader and the shoulder on the second peak becomes less pronounced (as shown in Figure 5.9b). Also, the pre-peak disappears at high temperature. The main peak maxima of the simulated *S(Q)* are plotted with temperature in Figure 5.9(c), in which the peak intensity decreases with temperature and a noticeable transition is observed at about 875 K. This transition seems to be from icosahedra phase to more liquid-like phase and it does not exist in the experimental data.

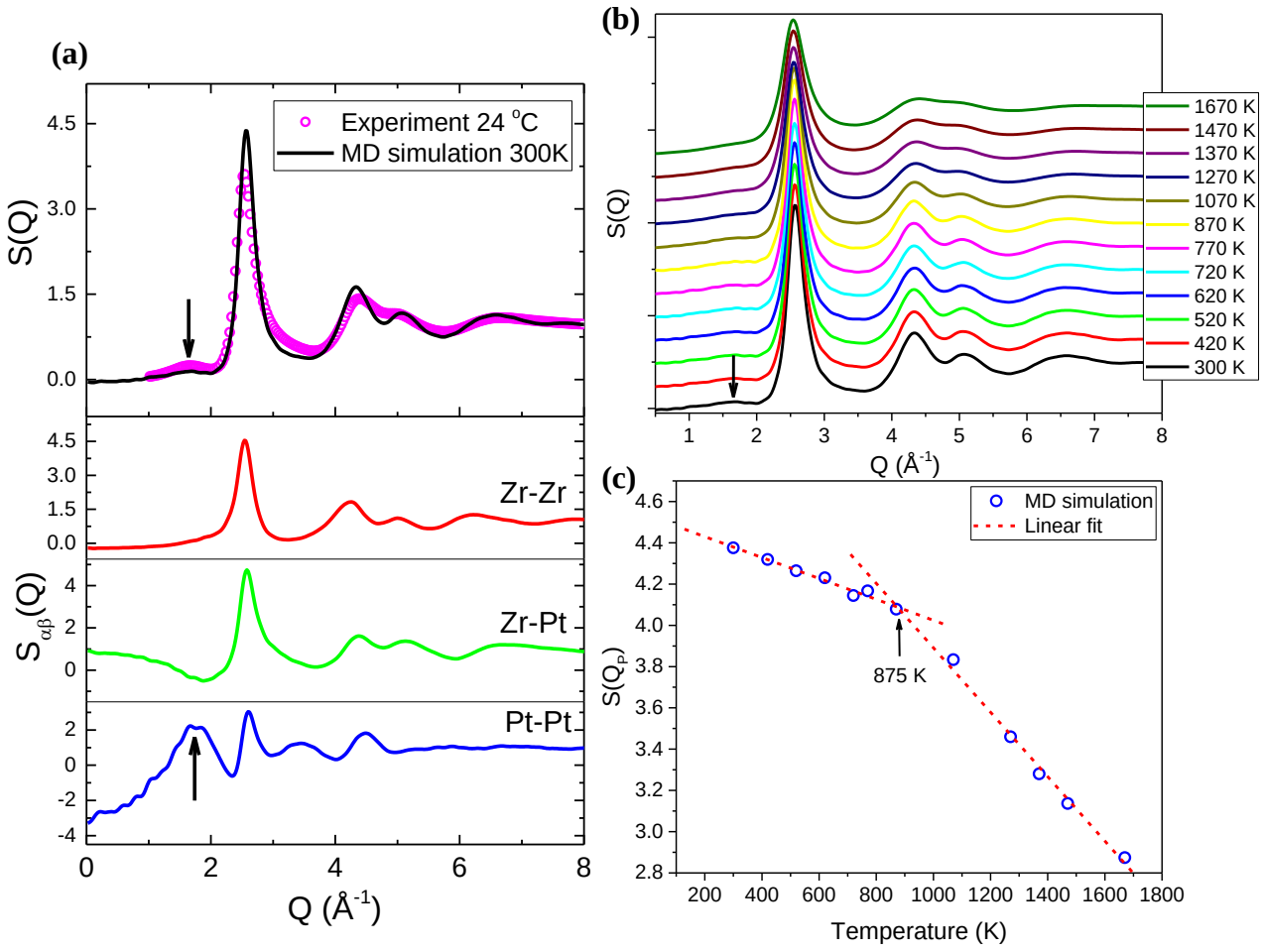

Figure 5.9 Structure functions for $Zr_{80}Pt_{20}$ from MD simulation: (a) total and partial S(Q) at 300 K and comparison with experimental data; (b) S(Q) at different temperatures; (c) first maximum of S(Q) as a function of temperature. Linear fit indicates an obvious transition at 875 K.

Through the MD simulation, we were unable to reproduce the nano-crystallization process, which may be because of the potentials used, or lower atomic mobility in the model. This is the common limitation of MD simulation.

Voronoi analysis is conducted on the $Zr_{80}Pt_{20}$ model structure to describe the local coordination polyhedron for each atom. A Voronoi cell encloses the space that is closer to the center atom than any other atoms, constructed by all the inner planes that bisect the bonds between the center atom and its neighboring atoms. The Voronoi index, <i3, i4, i5, i6>, is the number of faces with n edges on the polyhedron and describes the arrangement and topology of the nearest-neighbor atoms around the center atom.

The fraction of Pt-centered Voronoi polyhedra, out of the total number of Pt atoms, as a function of temperature is plotted in Figure 5.10(a). It is observed that the Pt-centered full icosahedra (<0,0,12,0>) and icosahedra-like clusters (<0,2,8,2> and <0,2,8,1>) are the dominant clusters, taking more than 50% of all the Pt-centered polyhedra. Since 13 atoms (one center atom and 12 shell atoms) are involved in a full icosahedron, most atoms in the system are related to the Pt-centered icosahedral clusters. However, they heavily decrease above 870 K, justifying that the transition is from icosahedra phase to more liquid-like phase. Meanwhile, the fraction of less icosahedra-like polyhedra (<0, 3, 6, 4> and <0, 3, 6, 3>) remains almost constant with temperature. For the Zr-centered polyhedra (as shown in Figure 5.10b), they are distributed more evenly among many different Voronoi indices than the Pt-centered polyhedra, and the full icosahedra (<0,0,12,0>) and icosahedra-like clusters were less populous than that in Pt-centered ones.

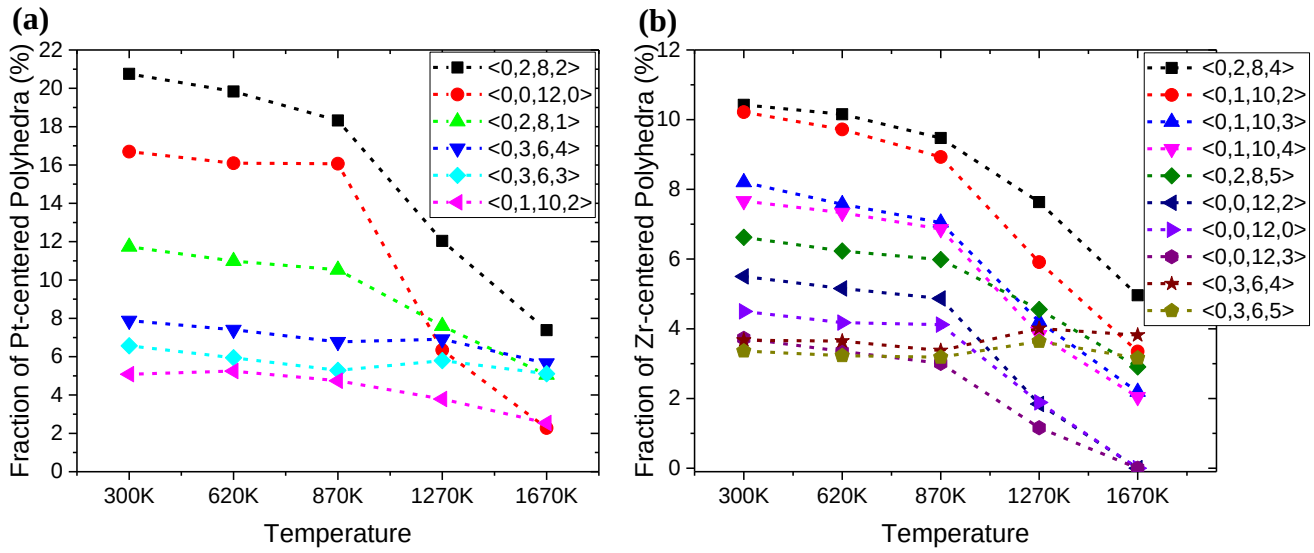

Figure 5.10 Fraction of Pt-centered (a) and Zr-centered (b) polyhedral at different temperatures in $Zr_{80}Pt_{20}$.

5.5 Conclusion

In-situ high-energy X-ray diffraction of $Zr_{65}Cu_{17}Ni_8Al_{10}$ BMG and $Zr_{80}Pt_{20}$ glassy ribbon reveals the phase transitions and thermal structural evolution at different temperatures. $Zr_{65}Cu_{17}Ni_8Al_{10}$ experiences a glass transition from glass to supercooled liquid at T_g = 360 ^oC before the nanocrystallization at T_x = 410 ^oC, while $Zr_{80}Pt_{20}$ forms icosahedral quasicrytalline phase (i-phase) at 430 ^oC followed by the crystallization at 570 ^oC.

In the glass state, there is competing between CSRO and TSRO in both $Zr_{65}Cu_{17}Ni_8Al_{10}$ and $Zr_{80}Pt_{20.}$ CSRO becomes dominant as temperature increase by developing more Zr-Zr atomic pairs for $Zr_{65}Cu_{17}Ni_8Al_{10}$, while there is a compromise between them for $Zr_{80}Pt_{20}$ as atomic pair distances and population do not change much. Beyond the glass state, icosahedral quasicrystalline phase (i-phase) forms in $Zr_{80}Pt_{20}$ as the preferred Zr-Zr pairs promote the icosahedral short-range order (ISRO) and formation of the i-phase, and thus delay the onset of crystallization.

This work reveals different thermal phase transition behavior and atomic structural evolution for $Zr_{65}Cu_{17}Ni_8Al_{10}$ and $Zr_{80}Pt_{20}$ glasses and explains them by the different topological and chemical effects of the different atomic pairs.

Chapter 6 Conclusions

Structure and dynamics at the atomic level in metallic glasses and liquids are poorly understood when compared to the crystalline solids. Even though viscosity is the one of the most basic property of liquids, its atomistic origin is not well elucidated. Also, the physics of the fragility of liquids and the crossover phenomenon is far from full understanding. Earlier, through molecular dynamics (MD) simulations a direct connection was found between the timescale describing the macroscopic viscous behavior, the Maxwell relaxation time, τ_M, and the timescale of microscopic atomic behavior, τ_{LC}, which is the time for an atom to lose or gain one nearest neighbor by cutting or creating a bond.

In order to validate the MD simulation result experimentally, inelastic neutron scattering (INS) experiments on metallic liquid droplets of $Zr_{50}Cu_{50}$ and $Zr_{80}Pt_{20}$ were carried out at the ARCS beamline at the Spallation Neutron Source (SNS). The main achievements of this work can be summarized as below:

(1) $I(Q, E)$ spectra with a wide Q-E space coverage, high statistics and low backgrounds for $Zr_{50}Cu_{50}$ and $Zr_{80}Pt_{20}$ metallic liquids were obtained from INS measurements for the first time with assistance of the electrostatic levitator (NESL).

(2) A full data analysis procedure and MATLAB codes were developed to obtain reliable Van Hove function, $G(r, t)$, including the self and distinct part, from INS data; temperature-dependent structural information and atomic dynamics can be elucidated based on the obtained Van Hove function.

(3) A new parameter $\Delta N_1(t)$ was defined and derived from the distinct part of the Van Hove function to describe the local collective motion of atoms in the liquids. Tow relaxation modes were

observed for the relaxation of $\Delta N_1(t)$, and a two-part exponential decay function was applied to fit the relaxation curves and the characteristic relaxation times were determined.

(4) The local atomic connectivity change time, τ_{LC}, was estimated from τ_2 based on the experimentally obtained Van Hove function information, and is equal to the Maxwell relaxation time, τ_M, determined from the measurements of the viscosity of the metallic liquids when $T > T_A$. This verified the conclusion from the MD simulation that the viscosity of liquids is controlled by the local atomic connectivity change at temperatures above the crossover temperature T_A.

In addition, the thermal structural evolution of two Zr-based metallic glasses were studied by in-situ high energy X-ray diffraction experiment and MD simulations with the pair distribution function (PDF) analysis technique. Main conclusions are listed as below:

(5) The different phase transition and thermal atomic structural evolution behaviors for $Zr_{65}Cu_{17}Ni_8Al_{10}$ and $Zr_{80}Pt_{20}$ were observed and attributed to the different effects of topological short-range order (TSRO) and chemical short-range order (CSRO) because of the different atomic pairs involved.

Using the experimental and data processing procedures developed by us, significant progress was made in the elucidation of local atomic dynamics in metallic liquids and thermal structural evolution in metallic glasses. Meanwhile, there are new points of interest and questions being raised during this research:

Only binary metallic liquids were measured by INS in this study. Whether the local dynamics is related to the complexity of the liquids is unanswered. It would be interesting to extend this research to different kinds of metallic liquids, such as single-element liquid and multi-component good glass-forming liquids.

Appendix

MATLAB codes for obtaining the Van Hove Function

```
%%%%%%%%%%%%%%%%%%%%%%%%%%%%%%%%%%%%%%%%%%%%%%%%%%%%%%%%%%%%%%%%%%%%%%%%
%%% MATLAB codes to calculate the Van Hove function
%%%
%%% Author: Zengquan Wang
%%%
%%% Date: last modified 10/31/2020
%%%
%%%%%%%%%%%%%%% Results from 20meV data only: %%%%%%%%%%%%%%%%%%
%%% >>> Read *.SPE data and tranfer to I(Q,E) matrix
%%% >>> Detailed balance and fill missing data (detector gaps)
%%% >>> Get F(Q,t) by 1st FT
%%% >>> Deconvolution with Resolution function F(t)(Vanadium)
%%% >>> Exponential fitting of F(Q,t) and Normalize by S(Q)
%%% >>> Alpha relaxation (decon)
%%% >>> Damping and calculate G(r,t) from 2nd FT
%%% >>> G(R1,t) decay, Calculate N.N. and their relaxation
%%%%%%%%%%%%%%%%%%%%%%%%%%%%%%%%%%%%%%%%%%%%%%%%%%%%%%%%%%%%%%%%%%%%%%%%

%% read data from *spe file
% clear;IQE0 = readIQE_spe('IQE_ZrPt_Ts-150C_20meV.spe');
% clear;IQE0 = readIQE_spe('IQE_ZrPt_Ts-50C_20meV.spe');
% clear;IQE0 = readIQE_spe('IQE_ZrPt_Ts+15C_20meV.spe');
% clear;IQE0 = readIQE_spe('IQE_ZrPt_Ts+50C_20meV.spe');
% clear;IQE0 = readIQE_spe('IQE_ZrPt_Ts+100C_20meV.spe');
% clear;IQE0 = readIQE_spe('IQE_ZrPt_Ts+150C_20meV.spe');
% clear;IQE0 = readIQE_spe('IQE_ZrPt_Ts+200C_20meV.spe');
% clear;IQE0 = readIQE_spe('IQE_ZrPt_Ts+275C_20meV.spe');
% clear;IQE0 = readIQE_spe('IQE_ZrPt_Ts+350C_20meV.spe');
%%%%%%%%%%%%%%%%%%%%%%%%%%%%%%%%%%
% % Zr50Cu50 data
% clear; IQE0 = readIQE_spe('IQE_CuZr_Tm-
150C_20meV_ebin0.2dQ0.02.spe');
% % % %clear; IQE0 = readIQE_spe('IQE_CuZr_Tm-
100C_50meV_ebin0.2dQ0.02.spe');%%% No data for Tm-100C at 20meV
% clear; IQE0 = readIQE_spe('IQE_CuZr_Tm-
50C_20meV_ebin0.2dQ0.02.spe');
% clear; IQE0 =
readIQE_spe('IQE_CuZr_Tm+15C_20meV_ebin0.2dQ0.02.spe');
clear; IQE0 =
readIQE_spe('IQE_CuZr_Tm+50C_20meV_ebin0.2dQ0.02.spe');
```

```
% clear; IQE0 =
readIQE_spe('IQE_CuZr_Tm+100C_20meV_ebin0.2dQ0.02.spe');
% clear; IQE0 =
readIQE_spe('IQE_CuZr_Tm+150C_20meV_ebin0.2dQ0.02.spe');
% % clear; IQE0 =
readIQE_spe('vanadium95518_NESL_20meV_ebin0.2dQ0.02.spe');
%%%%%%%%%%%%%%%%%%%%%%%%%%%%%%%%
%{
% clear; IQE0 = readIQE_spe('IQE_CuZr_Tm+150C_50meV.spe');
% clear; IQE0 = readIQE_spe('IQE_CuZr_Tm+150C_50meV_long.spe');
% clear; IQE0 = readIQE_spe('IQE_CuZr_Tm+50C_50meV.spe');
% clear; IQE0 = readIQE_spe('IQE_CuZr_Tm+15C_50meV.spe');
% clear; IQE0 = readIQE_spe('IQE_CuZr_Tm-50C_50meV.spe');
% clear; IQE0 = readIQE_spe('IQE_CuZr_Tm-100C_50meV.spe');
% clear; IQE0 = readIQE_spe('IQE_CuZr_Tm-150C_50meV.spe');

% clear;IQE0 = readIQE_spe('IQE_ZrPt_50meV_Tm-150C.spe');
% clear;IQE0 = readIQE_spe('IQE_ZrPt_50meV_Tm-50C.spe');
% clear;IQE0 = readIQE_spe('IQE_ZrPt_50meV_Tm+50C.spe');
% clear;IQE0 = readIQE_spe('IQE_ZrPt_50meV_Tm+150C.spe');
% clear;IQE0 = readIQE_spe('IQE_ZrPt_50meV_1500C.spe');

% clear;IQE0 = readIQE_spe('IQE_ZrNi_50meV_Tm-50C.spe');
% clear;IQE0 = readIQE_spe('IQE_ZrNi_50meV_Tm+50C.spe');
% clear;IQE0 = readIQE_spe('IQE_ZrNi_50meV_Tm+150C.spe');
% clear;IQE0 = readIQE_spe('IQE_ZrNi_50meV_1300C.spe');

% clear;IQE0 = readIQE_spe('IQE_vit106_50meV_RT.spe');
% clear;IQE0 = readIQE_spe('IQE_vit106_50meV_Tm+50C.spe');
% clear;IQE0 = readIQE_spe('IQE_vit106_50meV_Tm+150C.spe');
%}
Ei = 20 ; %%<<<<<<<<<<<<<<<<<<<<<<<<Incident Energy, Unit = meV

T = 955 + 273.15;   %%<<<<<<<<<<<<<<<< Input Temperature (C)
here. (Ta=1750K for Zr80Pt20)
% Qp1 = 2.5;        %% <<<<<<<<< Input Q1 value here,for alpha
relaxation @ diff Temp>>>>>
%%% Nominal Temp:   /Tm-150  /Tm-100 /Tm-50 /Tm+15  /Tm+50
/Tm+100 /Tm+150
%%% Real T(50meV):  /753.31 /805.71 /855.65 /919.89 /957.63 /NaN
/1046.44  %%% for ZrCu_50meV_Oct2015 Combined runs
%%% real T(20meV)   /755    /NaN    /855    /920    /955
/1005   /1055   %%% Estimate based on Ts=905C
% %Delta_T = -50; %% dT above or below Tm
bms = 0.553; %% <b>^2 = 0.553 barn for ZrCu, 0.5849 for
Zr80Pt20, 0.6873 for Zr64Ni36, 0.5278 for vit106
```

```
rho0 = 0.054; %atomic number density,0.054 for ZrCu, 0.045 for
ZrPt,~0.05 for Zr64Ni36, ? for vit106
%Tm=1180 + 273; %%C to K,Melting temperauture 935C for
Zr50Cu50,1180C for ZrPt, 1075C for ZrNi,850C for vit106
%T=Tm + Delta_T; %1500+273;     %Tm + Delta_T or a specific
value

if Ei == 50 %% meV
    Q_bin = 513; Q_num = Q_bin-87; %513-87 for 50meV
    Emax = 45; dE = 0.2;
elseif Ei == 20 %% meV
    Q_bin = 317; Q_num = Q_bin-55; %from Q=0.56, 317-55 for 20
meV
    Emax = 18; dE = 0.2;
end
Evec = -Emax:dE:Emax; %%%%%Ei=50 meV:
(Q294*E181,dQ=0.035)(Q401*E181,dQ=0.0256)
E_num = length(Evec); %%%%%% Evec=-110:1:110; %Ei=120 meV

%% read Q values from I(Q,E) matrix
Qvec=zeros(Q_num,1);
Q_rows=ceil((1+Q_bin)/8);
for i=1:Q_rows
    for j=1:8
        jj=j+8*(i-1);
        if (jj <=Q_num)
        Qvec(jj)=IQE0(i,j);
        end
    end
end

% %% Transfer *spe file to I(Q,E) matrix
IQE=zeros(Q_num,E_num);
IQE_err=zeros(Q_num,E_num);

E_rows=ceil((1+E_num)/8);
for i=1:Q_num
    for j=1: E_rows
        for k=1:8
            jj=k+8*(j-1);
            if (jj<=E_num)
                IQE(i,jj)=IQE0(Q_rows+E_rows+(2*i-2)*E_rows+j,
k); %60 is because the matrix start line is 61
                if IQE(i,jj)<0
                    IQE(i,jj)=NaN;
                end
```

```
                IQE_err(i,jj)=IQE0(Q_rows+E_rows+(2*i-
1)*E_rows+j, k);
            end
        end
    end
end
IQE=IQE/bms; %% <b>^2 = 0.553 barn for ZrCu, 0.5849 for
Zr80Pt20, 0.6873 for Zr64Ni36, 0.5278 for vit106

%%%plot I(Q,E) contour in log scale
logIQE=log10(IQE');
figure;contourf(Qvec,Evec,logIQE,40,'linestyle','none');colorbar
;
%colorbar('Yticklabel',[10^-6 10^-5 10^-4 10^-3 10^-2 10^-1 1]);
xlabel('Q [1/\AA]','Interpreter','latex','FontSize',20);
ylabel('E [meV]','FontSize',20);
set(gca,'Fontsize',16);
text(1,40,'S(Q,E)','fontsize',20);
% % %%non-log scale;
% figure; contourf(Qvec,Evec,IQE',100,'linestyle','none');
colorbar;
% xlabel('Q [1/\AA]','Interpreter','latex','FontSize',20);
% ylabel('E [meV]','FontSize',20);
%}
%% Detailed balance: Flip contour to fullfil E positive part
kb=8.6173e-5*1000; %meV/K
ff=exp(+Evec/(kb*T)); %detailed balance equation

for j=1:1:length(Qvec)

    IEslice=IQE(j,:);

    %%%%%%%%%%%%%%%%%%%%%%%%%%%%%%%%%%%%%%%%%%%%%%%%
% %     %%%% Plot to check if the E flip is Ok or not
% %     figure;plot(Evec,IEslice,'.')
% %     xlabel('E [meV]'); ylabel('Intensity [a.u.]');
% %     legend(['Q=',num2str(Qvec(j)),' A^-^1']);
% %     hold on;
% %
% %     IEslice2=NaN(1,length(Evec));
% %     for i=3:length(Evec)
% %             IEslice2(i)=IEslice(2*92-i)*ff(i); %% 91 is the
index of
% % %%max(I(E)) for CuZr_50mev
% %     end
% %     plot(Evec,IEslice2,'mo'); %flipped data
```

```
    %%%%%%%%%%%%%%%%%%%%%%%%%%%%%%%%%%%%%%%%%%%%%%%%%%%%

% %%      [IEmax,Imax]=max(IEslice);

    for i=1:length(Evec)
        if Evec(i)>0 && isnan(IEslice(i))
            IEslice(i)=IEslice(2*ceil(E_num/2)-i)*ff(i); %92 is
maximum for 181 points.
        end
    end

    IQE(j,:)=IEslice;
end

%%%%%%%%%%%%%%%%%%%%%%%%%%%%%%%%%%%%%%%%%%%%%%%%%%%%%%%%%%%
%%%%plot E_flipped I(Q,E) contour
figure;
logIQE=log10(IQE');
contourf(Qvec,Evec,logIQE,40,'linestyle','none');colorbar;
xlabel('Q [1/\AA]','Interpreter','latex','FontSize',20);
ylabel('E [meV]','FontSize',20);
text(1,40,'S(Q,E)','fontsize',20); set(gca,'Fontsize',16);

%% Interpolate to fill the gap of missing data
for i=1:E_num
    for j=1:Q_num
        if abs(Evec(i))<Emax*0.95 && Qvec(j)>3 && Qvec(j)<5.5 &&
(isnan(IQE(j,i))...
                ||IQE(j,i)> 3*mean(IQE(j-2:j+2,i-
2:i+2),'all','omitnan'))        %20meV
%         if abs(Evec(i))<Emax*0.95 && Qvec(j)>3 && Qvec(j)<8.2
&& isnan(IQE(j,i)) %50meV
%             IQE(j,i)= mean( [IQE(j-2,i), IQE(j-1,i),
IQE(j+1,i), IQE(j+1,i)] );
            IQE(j,i) = mean(IQE(j-2:j+2,i-
2:i+2),'all','omitnan');
        end
    end
end
% % for i=1:E_num
% %     for j=1:Q_num
% %     if abs(Evec(i))<Emax*0.95 && Qvec(j)>3 && Qvec(j)<5.5 &&
isnan(IQE(j,i)) %20meV
% % %     if abs(Evec(i))<Emax*0.95 && Qvec(j)>3 && Qvec(j)<8.2
&& isnan(IQE(j,i)) %50meV
```

```
% %          IQE(j,i)=mean( [IQE(j,i-2), IQE(j,i-1), IQE(j,i+1),
IQE(j,i+2)],'omitnan' );
% %      end
% %      end
% % end
%%%%%%%%%%%%%%%%%%%%%%%%%%%%%%%%%%%%%%%%%%%%%%%%%%%%
%%%plot gap-filled I(Q,E) contour
logIQE=log10(IQE');
figure;contourf(Qvec,Evec,logIQE,40,'linestyle','none');colorbar
;
xlabel('Q [1/\AA]','Interpreter','latex','FontSize',20);
ylabel('E [meV]','FontSize',20);
text(1,15,'S(Q,E)','fontsize',20); set(gca,'Fontsize',16);

% %
figure;contourf(Qvec,Evec,IQE',500,'linestyle','none');colorbar;
% % xlabel('Q [1/\AA]','Interpreter','latex','FontSize',16);
% % ylabel('E [meV]','FontSize',14);

%%  >>>>>>>>> Apply FT to get F(Q,t) <<<<<<<<<<
h_red=6.582119514E-16; %eV*s
w=Evec*1e-3/h_red;
dw=w(2)-w(1);
%%%%%%%%%%%%%%%%%%%%%%%%%%%%%%%%%%%%%%%%%%%%%%%%%%%%%%%%%%%
%%%%%%%%%%%%%%%%%%%%%%%%%%%%%%%%%%%%%%%%%%%%%%%%%%%%%%%%%%%
dt = 0.025; % Picosecond, =25fs
time = 0:dt:5.0; % Picosecond
%%%%%%%%%%%%%%%%%%%%%%%%%%%%%%%%%%%%%%%%%%%%%%%%%%%%%%%%%%%%%
%%%%%%%%%%%%%%%%%%%%%%%%%%%%%%%%%%%%%%%%%%%%%%%%%%%%%%%%%%%%%
FFQt=zeros(length(Qvec),length(time));

for i=1:Q_num
    for j=1:length(time)
        for k=1:E_num
            if ~isnan(IQE(i,k))
            FFQt(i,j)=FFQt(i,j)+IQE(i,k)*exp(1i*w(k)*time(j)*1E-
12)*dw;
            end
        end
    end
end
FFQt=real(FFQt)*h_red*1E3;

%
figure;contourf(Qvec,time,log(FFQt'),'linestyle','none');colorba
r;
```

```
% xlabel('Q [1/\AA]','Interpreter','latex','FontSize',14);
% ylabel('t [ps]','FontSize',14);

figure;contourf(Qvec,time,FFQt',40,'linestyle','none');colorbar;
xlabel('Q [1/\AA]','Interpreter','latex','FontSize',20);
ylabel('Time [ps]','FontSize',20); ylim( [0 2.5]);
text(1,1.2,'F(Q,t)','fontsize',20); set(gca,'Fontsize',16);

figure; plot(Qvec,FFQt(:,0/dt+1),'r.','linewidth',3);
xlabel('Q [1/\AA]','Interpreter','latex','FontSize',20);
ylabel('F(Q,t)','fontsize',20);  set(gca,'Fontsize',16);
% text(1,1.8,'F(Q,t)','fontsize',20);
hold on; grid on
plot(Qvec,real(FFQt(:,1/dt*0.05+1)),'g.','linewidth',3);
plot(Qvec,real(FFQt(:,1/dt*0.1+1)),'b.','linewidth',3);
plot(Qvec,real(FFQt(:,1/dt*0.2+1)),'k.','linewidth',3);
plot(Qvec,real(FFQt(:,1/dt*0.3+1)),'m.','linewidth',3);
plot(Qvec,real(FFQt(:,1/dt*0.5+1)),'y.','linewidth',3);
plot(Qvec,real(FFQt(:,1/dt*0.8+1)),'c.','linewidth',3);
legend('0 ps','0.05 ps','0.1 ps','0.2 ps','0.3 ps','0.5 ps','0.8
ps');
hold off;

%% alpha relaxation (Convoluted one)
Qp1 = 2.66;        %% <<<<<<<<<<<<<<<<<<<<<<<<<<<<<<< Input Q1
value here >>>>>
tau_a=FFQt(Qvec==Qp1,:)'/FFQt(Qvec==Qp1,1);
figure('Name','Alpha relaxation'); %%plot the decay of the first
F(Q,t) peak
plot(time,tau_a(1:length(time)),'bs');
xlabel('Time [ps]','FontSize',20); set(gca,'Fontsize',16);
ylabel('F(Q_1,t)/F(Q_1,t=0)','fontsize',20); grid on; hold on
%% Deconvolution with Energy resolution function obtained from
Vanadium data
load('Res_fun_Vanad_20mev','At_Van');  %% Load deconv. factor
from Van. data
load('Res_fun_Vanad_20mev','At_Van_polyfit') % load RF(t)
polyfit from Van. data
% load('Res_fun_simu_20mev','Ft');  At_Van = Ft;%% Load
simulated deconv. factor

ffQt = zeros(size(FFQt));  %%% Pre-set Normalized (deconvoluted)
F(Q,t)
for i=1:length(time)
%     ffQt(:,i) = FFQt(:,i)/At_Van(i)*At_Van(1);  %% Normalise
by Vanadium data
```

```
    ffQt(:,i) = FFQt(:,i)/At_Van_polyfit(i)*At_Van(1); %
Normalize by polyfit RF(t)
end
%% poly6 fitting of experimental RT result
% p1 = polyfit(time, At_Van, 6);
% At_Van_polyfit = polyval(p1,time);
% figure; plot(time,At_Van,'.',time,At_Van_polyfit,'-')
% xlabel('Time [ps]','Fontsize',16)
% ylabel('R(t)','Fontsize',16)
% set(gca,'Fontsize',16); grid on

%% Again, plot alpha relaxation (deconvoluted one)
tau_a=ffQt(Qvec==Qp1,:)'/ffQt(Qvec==Qp1,1); %% Input Q1 value
here
% figure; %%plot the decay of the first deconvoluted F(Q,t) peak
plot(time,tau_a(1:length(time)),'ro');
xlabel('Time [ps]','FontSize',20);
ylabel('F(Q_1,t)/F(Q_1,t=0)','fontsize',20);xlim([0 2.5]);
ylim([0. 1.1]);
set(gca,'Fontsize',16); grid on;
hold off; legend('w/o deconvolution','w/ deconvolution');

figure('Name','Deconvoluted F(Q,t)');
contourf(Qvec,time(time<=2.5),ffQt(:,time<=2.5)',50,'linestyle',
'none');colorbar;
xlabel('Q [1/\AA]','Interpreter','latex','FontSize',20);
ylabel('Time [ps]','FontSize',20); ylim( [0 2.5]);
text(1,1.2,'F(Q,t)','fontsize',20); set(gca,'Fontsize',16);

figure; plot(Qvec,ffQt(:,0/dt+1),'r.','linewidth',3);
xlabel('Q [1/\AA]','Interpreter','latex','FontSize',20);
ylabel('F(Q,t)','fontsize',20);  set(gca,'Fontsize',16);
% text(1,1.8,'F(Q,t)','fontsize',20);
hold on; grid on
plot(Qvec,real(ffQt(:,1/dt*0.05+1)),'g.','linewidth',3);
plot(Qvec,real(ffQt(:,1/dt*0.1+1)),'b.','linewidth',3);
plot(Qvec,real(ffQt(:,1/dt*0.2+1)),'k.','linewidth',3);
plot(Qvec,real(ffQt(:,1/dt*0.3+1)),'m.','linewidth',3);
plot(Qvec,real(ffQt(:,1/dt*0.5+1)),'y.','linewidth',3);
plot(Qvec,real(ffQt(:,1/dt*0.8+1)),'c.','linewidth',3);
legend('0 ps','0.05 ps','0.1 ps','0.2 ps','0.3 ps','0.5 ps','0.8
ps');
hold off;
%%
FFQt = ffQt; %% >>>>>>>>>>>>>>> IMPORTANT!!! Reset F(Q,t) value
to the deconvoluted one. <<<<<<<<<<<
```

```
%}
%% Tail fitting for t = 0 ps (first)
%{
% ind_to_fit=(Qvec>=5.5);
% xfit=Qvec(ind_to_fit);
% yfit=real(FFQt(ind_to_fit,1)); %% for t=0;
%
% FFQt_f=polyfit(xfit, yfit, 0);

% figure; plot(xfit, yfit,'ro');
% hold on;
% plot(Qvec, pp, 'linewidth',3);
%}
%% Exponetial decaying tail fitting for t=0-n ps (2nd)
xq=0.02:.02:50;          %%% 50 represents Inf
FFQt_fl=zeros(length(xq),length(time)); %%extended fitting line
for self part
FFQt_f=zeros(length(Qvec),length(time)); %%data range of fitting
line

At = zeros(length(time),1);
Bt = zeros(length(time),1);
for i = 1:1:length(time) %length(time)

    ind_to_fit=(Qvec>=1.9); %fitting from 1.8 for ZrPt and 1.9
for ZrCu
    xfit=Qvec(ind_to_fit);
    yfit=real(FFQt(ind_to_fit,i)); %% for t=0.05 ps;

    % Set up fittype and options.
    ftype = fittype( 'At*exp(-Bt*x^2)', 'independent', 'x',
'dependent', 'y' );
    opts = fitoptions( 'Method', 'NonlinearLeastSquares' );
    opts.Algorithm = 'Trust-Region'; %% or 'Levenberg-Marquardt'
    opts.Display = 'Off';
    opts.Lower = [0 0]; %%lower limit for At and Bt
    opts.Robust = 'LAR'; %% or 'LAR','Off'
    opts.StartPoint = [0.01 0.01];

    % Fit model to data.
    fit1 = fit( xfit, yfit, ftype, opts);
    At(i)=fit1.At;
    Bt(i)=fit1.Bt;

    FFQt_f(:,i)=At(i)*exp(-Bt(i)*Qvec.^2); %data range of
fitting line
```

```
    FFQt_fl(:,i)=At(i)*exp(-Bt(i)*xq.^2); %extended fitting line

    %%%figure; plot(fitresult, xfit, yfit);

        %%%%%%%%%%%%%%%%%%%%%%%%%%%%%%%%%%%%%%%%%%%%%%%%%%%%%%%%%%%
       %%% plot fit results for each time to check if fitting is
ok or not
     if time(i)<= 0.1 || time(i)>0.1 && ...
         time(i)<= 1.0 && mod(i,4)==1 || time(i)>1 && time(i)<=
3.0 && mod(i,10)==1 ...
         || time(i)>3 && mod(i,20)==1  %plot interval
0.2,0.25,0.5ps
        figure; %plot(fitresult, Qvec,real(FFQt(:,i)));
        plot(Qvec,real(FFQt(:,i)),'.');
        hold on;
        %%%% FFQt_f(:,i)=At*exp(-Bt*Qvec.^2); %data of fitting
line
        %%%% x=0:.02:15;
        %%%% FFQt_fl(:,i)=At*exp(-Bt*x.^2); %extended fitting
line
        plot(xq, FFQt_fl(:,i), 'r','linewidth',2.5);
        xlabel('Q'); ylabel('F(Q)');grid on; xlim([0 12])
        text(0.5,0.02,['t = ',num2str(time(i)),'
ps'],'FontSize',16);

        %figure(80); hold on; plot(Qvec,real(FFQt(:,i))-FFQt_f)
        %figure(90); hold on;
plot(Qvec,real(FFQt(:,i))./FFQt_f , 'm')
        %%%
        %%%%%%%%%%%%%%%%%%%%%%%%%%%%%%%%%%%%%%%%%%%%%%%%%%%%%%%%%%%
%%%%
     end
end
%plot time=0 fitting and check S(Q) value.
SQ = At(1)
%%
%%% Normalize F(Q,t) by S(Q) to unity
FFQt = FFQt/At(1);
FFQt_f = FFQt_f/At(1);
FFQt_fl = FFQt_fl/At(1);

%%% Or, Should normalize F(Q,t) by the 1st fitting curve (since
sometimes S(Q) or fitting curve
%%% at t=0 is not perfectly constant) %%
% %     for i= 1:length(time)
% %         FFQt(:,i) = FFQt(:,i)./FFQt_f(:,1);
```

```
% %          FFQt_f(:,i) = FFQt_f(:,i)./FFQt_f(:,1);
% %          FFQt_fl(:,i) = FFQt_f(:,i)./FFQt_fl(:,1);
% %      end
max(real(FFQt(:,1)))
FQ1 = FFQt(Qvec==Qp1,:)';

figure;plot(Qvec,real(FFQt(:,1)),'.');
hold on;  plot(xq, FFQt_fl(:,1), 'r','linewidth',2.5);
xlabel('Q'); ylabel('F(Q)');grid on; xlim([0 15]);
set(gca,'Fontsize',16);

%%% plot At and Bt with time
figure('Name','A(t)'); plot(time, At,'ro','linewidth',1);
xlabel('Time [ps]','FontSize',20);    xlim([0 2.5]);
ylabel('A(t)','fontsize',20); set(gca,'Fontsize',16); grid on;
figure('Name','B(t)'); plot(time, Bt,'bs','linewidth',1);
xlabel('Time [ps]','FontSize',20);     xlim([0 2.5]);
ylabel('w(t)','fontsize',20); set(gca,'Fontsize',16); grid on;

%%%%--------------- Plot deconvoluted and normalized F(Q,t) ----
---------%%%%%%
figure('Name','Normalized F(Q,t)');
contourf(Qvec,time(time<=2.5),FFQt(:,time<=2.5)',50,'linestyle',
'none');colorbar;
xlabel('Q [1/\AA]','Interpreter','latex','FontSize',20);
ylabel('Time [ps]','FontSize',20); ylim( [0
2.5]);set(gca,'Fontsize',16);
text(1,1.2,'F(Q,t)','fontsize',20);

figure; plot(Qvec,FFQt(:,0/dt+1),'r.','linewidth',3);
xlabel('Q [1/\AA]','Interpreter','latex','FontSize',20);
ylabel('F(Q,t)','fontsize',20);set(gca,'Fontsize',16); grid on;
% text(1,1.8,'F(Q,t)','fontsize',20);
hold on; grid on
plot(Qvec,real(FFQt(:,1/dt*0.05+1)),'g.','linewidth',3);
plot(Qvec,real(FFQt(:,1/dt*0.1+1)),'b.','linewidth',3);
plot(Qvec,real(FFQt(:,1/dt*0.2+1)),'k.','linewidth',3);
plot(Qvec,real(FFQt(:,1/dt*0.3+1)),'m.','linewidth',3);
plot(Qvec,real(FFQt(:,1/dt*0.5+1)),'y.','linewidth',3);
plot(Qvec,real(FFQt(:,1/dt*0.8+1)),'c.','linewidth',3);
legend('0 ps','0.05 ps','0.1 ps','0.2 ps','0.3 ps','0.5 ps','0.8
ps');
hold off;
%%%%%%%%%%%%%%%%%%%%%%%%%%%%%%%%%%%%%%%%%%%%%%%%%%%%%%%%%%%%%%%%5

%% Apply damping or not before 2nd FT
```

```
%%% partial damping function for partial Q range
Qs=min(Qvec)+0.7*(max(Qvec)-min(Qvec)); %start point for
damping, damp last 30 percent
xxx=pi/(max(Qvec)-Qs)*(Qvec-Qs);
f_damp=sin(xxx)./xxx;   %%% Damping function sinx/x

time = 0:dt:2.5;  %% Reset time range and Disgard t>= 2.5 ps
part

FFQt_d = zeros(length(Qvec),length(time)); %% Distinct part of
F(Q, t)
for j=1:length(Qvec)
    if xxx(j)<0
        f_damp(j)=1;
    end
end
for i=1:length(time)
%       FFQt_d(:,i)=real(FFQt(:,i)-FFQt_f(:,i))*1; %% no damping
   FFQt_d(:,i)=real(FFQt(:,i)-FFQt_f(:,i)).*f_damp; %%applying
damping to F(Q,t=0)
end
%%%
%%%%%%%%%%%%%%%%%%%%%%%%%%%%%%%%%%%%%%%%%%%%%%%%%%%%%%%%%%%

%% double FT to get G(r,t)
dr = 0.02;
r = (0:dr:12)';

dQvec=diff(Qvec);
dQ=zeros(Q_num,1);
dQ(1)=dQvec(1); dQ(Q_num)=dQvec(Q_num-1);
for i=2:Q_num-1
    dQ(i)=.5*dQvec(i-1)+.5*dQvec(i);
end

%%%%%%%%%%%%%%%%%%Caculate distinct part of G(r,t)
%%Grt = zeros(length(r),length(time)); % Total
Grt_d=zeros(length(r),length(time)); % Distinct
%%grt_d=zeros(length(r),length(time)); %
%%Rrt_d=zeros(length(r),length(time)); % Radial DF
for i=1:length(time)
    for j=1:length(r)
        for k=1:length(Qvec)
            if ~isnan(FFQt_d(k,i))
                %%Grt(j,i)=Grt(j,i)+(FFQt(k,i))*(exp(1i*Qvec(k)*
r(j)))*dQ(k);
```

```
                Grt_d(j,i)=Grt_d(j,i)+FFQt_d(k,i)*Qvec(k)^2 *
sin(Qvec(k)*r(j))/(Qvec(k)*r(j))*dQ(k);
            end
        end
    end
end

% % %% Grt_d=Grt_d/2/pi^2/rho0/At(1);  % At(1)=0.0377 comes from
fitting of F(Q,t=0)
Grt_d = Grt_d/2/pi^2/rho0;
grt_d = Grt_d + 1;

%% Contour plot of G_d
Grt_d = Grt_d(r>=1.5,:); %only plot r>1.6 for G_d
r = r(r>=1.5);

figure('Name','Gd(r,t) Contour');
contourf(r,time,Grt_d',50,'linestyle','none');colorbar;
xlabel('r
[\AA]','Interpreter','latex','FontSize',20); %xlim([1.6 12]);
set(gca,'Fontsize',16);
ylabel('Time [ps]','FontSize',20); ylim( [0 2.5]);
text(8,1.2,'G_d(r,t)','fontsize',20);

figure;  %% Plot Grt_d slices
plot(r,Grt_d(:,0/dt+1),'r-','linewidth',2);
set(gca,'Fontsize',16); grid on;
xlabel('r
[\AA]','Interpreter','latex','FontSize',20);ylabel('G_d(r,t)','f
ontsize',20);
% text(1,1.8,'F(Q,t)','fontsize',20);
hold on;  xlim([1.5 12]);
plot(r,Grt_d(:,1/dt*0.05+1),'g-','linewidth',2);
plot(r,Grt_d(:,1/dt*0.1+1),'b-','linewidth',2);
plot(r,Grt_d(:,1/dt*0.2+1),'k-','linewidth',2);
plot(r,Grt_d(:,1/dt*0.5+1),'m-','linewidth',2);
plot(r,Grt_d(:,1/dt*1.0+1),'y-','linewidth',2);
plot(r,Grt_d(:,1/dt*2.0+1),'c-','linewidth',2);
legend('0 ps','0.05 ps','0.1 ps','0.2 ps','0.5 ps','1.0 ps','2.0
ps');
hold off; grid on;
%%%%%%%%%%%%%%%%%%%%%%%%%%%%%%%%%%%%%%%%%%%%%%%%%%%%%%%%%%%%%%%


%% Calculate self part of G(r,t) from 0 to Inf
%{
```

```
dxq=0.02;

% r = (0:dr:3)';
% % xq=dxq:dxq:50; %%% 50 represents Inf
% % FFQt_fl=zeros(length(xq),length(time)); %extended fitting
line to Q=50, self F(Q,r)
Grt_s=zeros(length(r),length(time)); %% FT for the self F(Q,t)
for i=1:length(time)
% %     FFQt_fl(:,i)=At(i)*exp(-Bt(i)*xq.^2)/At(1); %extended
fitting line
    for j=1:length(r)
        for k=1:length(xq)
            if ~isnan(FFQt_fl(k,i))
                Grt_s(j,i)=Grt_s(j,i)+FFQt_fl(k,i)*xq(k)^2 *
sin(xq(k)*r(j))/(xq(k)*r(j))*dxq;
            end
        end
    end
    %figure; plot(r,Grt_s(:,i))
end

Grt_s=Grt_s/2/pi^2/rho0;
% Grt=Grt_d+Grt_s;

figure;contourf(r,time,Grt_s',50,'linestyle','none');colorbar;
xlabel('r [\AA]','Interpreter','latex','FontSize',20);
xlim([0 3]);set(gca,'Fontsize',16);
ylabel('Time [ps]','FontSize',20); ylim( [0 2.5]); grid on;
% text(8,1.2,'G(r,t)','fontsize',16);

figure;  %% Plot Grt_d slices
plot(r,Grt_s(:,0.025/dt+1),'r-','linewidth',3); xlim([0
3]);set(gca,'Fontsize',16); grid on;
xlabel('r
[\AA]','Interpreter','latex','FontSize',20);ylabel('G_s(r,t)','f
ontsize',20);
% text(1,1.8,'F(Q,t)','fontsize',20);
hold on;
plot(r,Grt_s(:,1/dt*0.05+1),'g-','linewidth',3);
plot(r,Grt_s(:,1/dt*0.1+1),'b-','linewidth',3);
plot(r,Grt_s(:,1/dt*0.2+1),'k-','linewidth',3);
plot(r,Grt_s(:,1/dt*0.5+1),'m-','linewidth',3);
plot(r,Grt_s(:,1/dt*1.0+1),'y-','linewidth',3);
plot(r,Grt_s(:,1/dt*2.0+1),'c-','linewidth',3);
legend('0.025 ps','0.05 ps','0.1 ps','0.2 ps','0.5 ps','1.0
ps','2.0 ps');
```

```
hold off; grid on;

% %
figure;contourf(r,time,imag(Grt'),20,'linestyle','none');colorba
r;
% % xlabel('r [\AA]','Interpreter','latex','FontSize',14);
% % ylabel('t [ps]','FontSize',14);
%}

%% plot the decay of the first peak G(r1,t) to determine
characteristic time scale
%{
[C1,I]=max(Grt_d((r>=2 & r<=4),:));
figure; %%plot the decay of the first peak
plot(time,C1/C1(1),'ro');
xlabel('Time [ps]','FontSize',14);
ylabel('G_1(t)/G_1(t=0)','fontsize',14);
%
% figure;
% plot(time,r(I),'s');
% xlim([-0.05 .9]);
% xlabel('Time [ps]','FontSize',14);
% ylabel('r1 [\AA]','Interpreter','latex','FontSize',14);
% r1=r(I);
%}
 %% plot the decay of the first three peaks to determine
characteristic time scale
[C1,I]=max(Grt_d((r>=2 & r<=4),:));
[C2,I]=max(Grt_d((r>=4 & r<=6.5),:));
[C3,I]=max(Grt_d((r>=6.5 & r<=9),:));
figure; %%plot the decay of the first peak
plot(time,C1/C1(1),'ro',time,C2/C2(1),'g>', time,
C3/C3(1),'bs','linewidth',1);
ylim([0 1.05]); set(gca,'Fontsize',16); grid on;
legend('1st peak','2nd peak','3rd peak');
xlabel('Time [ps]','FontSize',20);
ylabel('G_P(t)/G_P(t=0)','fontsize',20);
% text(0.5,1.01,'Zr50Cu50 Tm-50C','fontsize',20);
CC=[C1; C2; C3]';
CCnorm=[C1/C1(1); C2/C2(1); C3/C3(1)]';  %% Normalized G_d
relaxation of 3 peaks

%% Calculate Coordination Number and time to lose one neighbor.
% %{
NN = zeros(length(time),1);  %%% Coordination Number
```

```
% NN1 = zeros(length(time),1); % Manual integration vs.
Trapozoidal, same results.
%%%>>>>>>>>>>>>>>>>>>>>>>>>>
% rlo = 1.80 ;  %%% Input the first shell R-range here.
% rhi = 3.84 ;
%%%<<<<<<<<<<<<<<<<<<<<<<<<
% rrange = (r>=rlo & r<=rhi);

for i = 1:1:length(time)
    % floating first shell R-range
    [~, I1]=min(Grt_d(r>=1.5 & r< 2.5,i));
    rlo = r(find(r==1.5) + I1 -1);
    [~, I2]=min(Grt_d(r>=3.5 & r<4.5,i));
    rhi = r(find(r==3.5) + I2 -1);
    rrange = (r>=rlo & r<=rhi);

    for j = 1:length(r)
        if r(j) == rlo || r(j) == rhi
       NN(i) = NN(i) +
4*pi*rho0*r(j)^2.*(Grt_d(j,i)+1)*dr/2; %Rrt_d(j,i)*dr;
        elseif r(j)> rlo && r(j) < rhi
        NN(i) = NN(i) + 4*pi*rho0*r(j)^2.*(Grt_d(j,i)+1)*dr;
        end
    end          %%% Manual integration; Results same as
Trapozoidal integration NN1
%     NN1(i)=
trapz(r(rrange),4*pi*rho0*r(rrange).^2.*(Grt_d(rrange,i)+1)); %%
% Trapozoidal integration
end
figure('Name','Coordination Num');
plot(time, NN, 'ro')%,time, NN1,'b*');
set(gca,'Fontsize',16); grid on;
xlabel('Time [ps]','FontSize',20);
ylabel('N(t)','fontsize',20);
% text(0.5,11.5,'Zr50Cu50 Tm+150C','fontsize',16);

% figure; plot(time,NN/NN(1)*12.5,'ro');
%%%%%%%%%%%%%%%%%%%%%%%%%%%%%%%%%%%%%%%%%%%%%%%%%%%%%%%%%%%
%}

%% Calculate N.N. above average through Integration of Grt_d >0
NNplus = zeros(length(time),1);    %%% Coordination Number
deviated from LR average.
% NNplus1 = zeros(length(time),1); %Manual integration vs.
Trapozoidal one
rlo = 2.0 ;  %%% Input the first shell R-range here.
```

```
rhi = 4.0 ;
rrange = (r>=rlo & r<=rhi);

for i = 1:1:length(time)
    for j = 1:length(r)
        if r(j)> rlo && r(j) < rhi && Grt_d(j,i)>=0
        NNplus(i) = NNplus(i) +
4*pi*rho0*r(j)^2.*(Grt_d(j,i)+0)*dr;   % Manual rectangular
integration
        end
    end
%     yyy=4*pi*r.^2.*Grt_d(:,i)*rho0;       %%% Trapezoidal
integration, result same as above manual one
%     NNplus1(i) = trapz(yyy(yyy>=0 & r >2 & r <4))*dr;
end
figure('Name','Delta_N(t)');
plot(time, NNplus, 'ro');
set(gca,'Fontsize',16); grid on;
xlabel('Time [ps]','FontSize',20);
ylabel('\DeltaN(t)','fontsize',20);
%
%%% END OF THE SCRIPT.
```

List of References

[1] T. Egami, Elementary excitation and energy landscape in simple liquids, Modern Physics Letters B, 28 (2014) 1430006.

[2] P.W. Anderson, Through the Glass Lightly, Science, 267 (1995) 1615-1616.

[3] V. Lubchenko, P.G. Wolynes, Theory of Structural Glasses and Supercooled Liquids, Annual Review of Physical Chemistry, 58 (2007) 235-266.

[4] M.E. Blodgett, T. Egami, Z. Nussinov, K.F. Kelton, Proposal for universality in the viscosity of metallic liquids, Scientific Reports, 5 (2015) 13837.

[5] S. Yip, Understanding the viscosity of supercooled liquids and the glass transition through molecular simulations, Molecular Simulation, 42 (2016) 1330-1342.

[6] K. Akihiro, L. Xi, Y. Sidney, Commentary on the temperature-dependent viscosity of supercooled liquids: a unified activation scenario, Journal of Physics: Condensed Matter, 21 (2009) 504104.

[7] A. Kushima, X. Lin, J. Li, J. Eapen, J.C. Mauro, X. Qian, P. Diep, S. Yip, Computing the viscosity of supercooled liquids, The Journal of Chemical Physics, 130 (2009) 224504.

[8] C.A. Angell, Spectroscopy simulation and scattering, and the medium range order problem in glass, Journal of Non-Crystalline Solids, 73 (1985) 1-17.

[9] C.A. Angell, Formation of Glasses from Liquids and Biopolymers, Science, 267 (1995) 1924-1935.

[10] C.A. Angell, K.L. Ngai, G.B. McKenna, P.F. McMillan, S.W. Martin, Relaxation in glassforming liquids and amorphous solids, Journal of Applied Physics, 88 (2000) 3113-3157.

[11] P.G. Debenedetti, F.H. Stillinger, Supercooled liquids and the glass transition, Nature, 410 (2001) 259.

[12] V.N. Novikov, A.P. Sokolov, Poisson's ratio and the fragility of glass-forming liquids, Nature, 431 (2004) 961.

[13] Y.C. Hu, F.X. Li, M.Z. Li, H.Y. Bai, W.H. Wang, Structural signatures evidenced in dynamic crossover phenomena in metallic glass-forming liquids, Journal of Applied Physics, 119 (2016) 205108.

[14] K.F. Kelton, Kinetic and structural fragility—a correlation between structures and dynamics in metallic liquids and glasses, Journal of Physics: Condensed Matter, 29 (2017) 023002.

[15] A.K. Gangopadhyay, K.F. Kelton, Recent progress in understanding high temperature dynamical properties and fragility in metallic liquids, and their connection with atomic structure, Journal of Materials Research, 32 (2017) 2638-2657.

[16] A. Jaiswal, T. Egami, K.F. Kelton, K.S. Schweizer, Y. Zhang, Correlation between Fragility and the Arrhenius Crossover Phenomenon in Metallic, Molecular, and Network Liquids, Physical Review Letters, 117 (2016) 205701.

[17] A. Jaiswal, S. O'Keeffe, R. Mills, A. Podlesynak, G. Ehlers, W. Dmowski, K. Lokshin, J. Stevick, T. Egami, Y. Zhang, Onset of Cooperative Dynamics in an Equilibrium Glass-Forming Metallic Liquid, The Journal of Physical Chemistry B, 120 (2016) 1142-1148.

[18] F. Mallamace, C. Branca, C. Corsaro, N. Leone, J. Spooren, S.-H. Chen, H.E. Stanley, Transport properties of glass-forming liquids suggest that dynamic crossover temperature is as important as the glass transition temperature, 107 (2010) 22457-22462.

[19] A. Jaiswal, A. Podlesynak, G. Ehlers, R. Mills, S. O'Keeffe, J. Stevick, J. Kempton, G. Jelbert, W. Dmowski, K. Lokshin, T. Egami, Y. Zhang, Coincidence of collective relaxation anomaly and specific heat peak in a bulk metallic glass-forming liquid, Physical Review B, 92 (2015) 024202.

[20] H.C. Andersen, Molecular dynamics studies of heterogeneous dynamics and dynamic crossover in supercooled atomic liquids, Proceedings of the National Academy of Sciences of the United States of America, 102 (2005) 6686-6691.

[21] M.D. Dickey, Stretchable and Soft Electronics using Liquid Metals, Advanced Materials, DOI 10.1002/adma.201606425(2017) 1606425-n/a.

[22] D. Bolmatov, V.V. Brazhkin, K. Trachenko, The phonon theory of liquid thermodynamics, Scientific Reports, 2 (2012) 421.

[23] J. Brillo, A.I. Pommrich, A. Meyer, Relation between Self-Diffusion and Viscosity in Dense Liquids: New Experimental Results from Electrostatic Levitation, Physical Review Letters, 107 (2011) 165902.

[24] S.M. Chathoth, A. Meyer, M.M. Koza, F. Juranyi, Atomic diffusion in liquid Ni, NiP, PdNiP, and PdNiCuP alloys, Applied Physics Letters, 85 (2004) 4881-4883.

[25] D. Holland-Moritz, S. Stüber, H. Hartmann, T. Unruh, T. Hansen, A. Meyer, Structure and dynamics of liquid Ni36Zr64 studied by neutron scattering, Physical Review B, 79 (2009) 064204.

[26] A. Meyer, S. Stüber, D. Holland-Moritz, O. Heinen, T. Unruh, Determination of self-diffusion coefficients by quasielastic neutron scattering measurements of levitated Ni droplets, Physical Review B, 77 (2008) 092201.

[27] A. Meyer, Self-diffusion in liquid copper as seen by quasielastic neutron scattering, Physical Review B, 81 (2010).

[28] S.W. Basuki, A. Bartsch, F. Yang, K. Rätzke, A. Meyer, F. Faupel, Decoupling of Component Diffusion in a Glass-Forming Zr46.75Ti8.25Cu7.5Ni10Be27.5 Melt Far above the Liquidus Temperature, Physical Review Letters, 113 (2014) 165901.

[29] F. Kargl, H. Weis, T. Unruh, A. Meyer, Self diffusion in liquid aluminium, Journal of Physics: Conference Series, 340 (2012) 012077.

[30] S. Szabó, Z. Evenson, Self-diffusion in liquid Al-Ge investigated with quasi-elastic neutron scattering, Applied Physics Letters, 110 (2017) 161903.

[31] Neutron scattering lengths and cross sections, https://www.ncnr.nist.gov/resources/n-lengths/.

[32] J.-P. Hansen, I.R. McDonald, Theory of simple liquids: with applications to soft matter, Academic Press2013.

[33] T. Iwashita, D.M. Nicholson, T. Egami, Elementary Excitations and Crossover Phenomenon in Liquids, Physical Review Letters, 110 (2013) 205504.

[34] T. Iwashita, T. Egami, Local energy landscape in a simple liquid, Physical Review E, 90 (2014) 052307.

[35] L. Van Hove, Correlations in Space and Time and Born Approximation Scattering in Systems of Interacting Particles, Physical Review, 95 (1954) 249-262.

[36] T. Egami, Real-Space Description of Dynamics of Liquids, Quantum Beam Science, 2 (2018).

[37] T. Egami, Local Dynamics in Liquids and Glassy Materials, Journal of the Physical Society of Japan, 88 (2019) 081001.

[38] B.N. Brockhouse, N.K. Pope, Time-Dependent Pair Correlations in Liquid Lead, Physical Review Letters, 3 (1959) 259-262.

[39] J.R.D. Copley, J.M. Rowe, Density fluctuations in liquid rubidium. I. Neutron-scattering measurements, Physical Review A, 9 (1974) 1656-1666.

[40] U. Dahlborg, W. Gudowski, M. Davidovic, Van Hove correlation functions from coherent neutron inelastic scattering, Journal of Physics: Condensed Matter, 1 (1989) 6173.

[41] A. Rahman, Density fluctuations in liquid rubidium. II. Molecular-dynamics calculations, Physical Review A, 9 (1974) 1667-1671.

[42] A. Jaiswal, T. Egami, Y. Zhang, Atomic-scale dynamics of a model glass-forming metallic liquid: Dynamical crossover, dynamical decoupling, and dynamical clustering, Physical Review B, 91 (2015) 134204.

[43] M.H. Yang, Y. Li, J.H. Li, B.X. Liu, Atomic-scale simulation to study the dynamical properties and local structure of Cu-Zr and Ni-Zr metallic glass-forming alloys, Physical Chemistry Chemical Physics, 18 (2016) 7169-7183.

[44] Y. Shinohara, R. Matsumoto, M.W. Thompson, C.W. Ryu, W. Dmowski, T. Iwashita, D. Ishikawa, A.Q.R. Baron, P.T. Cummings, T. Egami, Identifying Water–Anion Correlated Motion in Aqueous Solutions through Van Hove Functions, The Journal of Physical Chemistry Letters, DOI 10.1021/acs.jpclett.9b02891(2019) 7119-7125.

[45] T. Egami, Y. Shinohara, Dynamics of water in real space and time, Molecular Physics, DOI 10.1080/00268976.2019.1649488(2019) 1-5.

[46] Y. Shinohara, W. Dmowski, T. Iwashita, D. Ishikawa, A.Q.R. Baron, T. Egami, Local correlated motions in aqueous solution of sodium chloride, Physical Review Materials, 3 (2019) 065604.

[47] Y. Shinohara, W. Dmowski, T. Iwashita, B. Wu, D. Ishikawa, A.Q.R. Baron, T. Egami, Viscosity and real-space molecular motion of water: Observation with inelastic x-ray scattering, Physical Review E, 98 (2018) 022604.

[48] T. Iwashita, B. Wu, W.-R. Chen, S. Tsutsui, A.Q.R. Baron, T. Egami, Seeing real-space dynamics of liquid water through inelastic x-ray scattering, Science Advances, 3 (2017).

[49] T. Kordel, D. Holland-Moritz, F. Yang, J. Peters, T. Unruh, T. Hansen, A. Meyer, Neutron scattering experiments on liquid droplets using electrostatic levitation, Physical Review B, 83 (2011) 104205.

[50] D.L. Abernathy, M.B. Stone, M.J. Loguillo, M.S. Lucas, O. Delaire, X. Tang, J.Y.Y. Lin, B. Fultz, Design and operation of the wide angular-range chopper spectrometer ARCS at the Spallation Neutron Source, Rev Sci Instrum, 83 (2012) 015114.

[51] N.A. Mauro, A.J. Vogt, K.S. Derendorf, M.L. Johnson, G.E. Rustan, D.G. Quirinale, A. Kreyssig, K.A. Lokshin, J.C. Neuefeind, K. An, X.L. Wang, A.I. Goldman, T. Egami, K.F. Kelton, Electrostatic levitation facility optimized for neutron diffraction studies of high temperature liquids at a spallation neutron source, Rev Sci Instrum, 87 (2016).

[52] R.T. Azuah, L.R. Kneller, Y. Qiu, P.L. Tregenna-Piggott, C.M. Brown, J.R. Copley, R.M. Dimeo, DAVE: A Comprehensive Software Suite for the Reduction, Visualization, and Analysis of Low Energy Neutron Spectroscopic Data, Journal of research of the National Institute of Standards and Technology, 114 (2009) 341-358.

[53] O. Arnold, J.C. Bilheux, J.M. Borreguero, A. Buts, S.I. Campbell, L. Chapon, M. Doucet, N. Draper, R. Ferraz Leal, M.A. Gigg, V.E. Lynch, A. Markvardsen, D.J. Mikkelson, R.L. Mikkelson, R. Miller, K. Palmen, P. Parker, G. Passos, T.G. Perring, P.F. Peterson, S. Ren, M.A. Reuter, A.T. Savici, J.W. Taylor, R.J. Taylor, R. Tolchenov, W. Zhou, J. Zikovsky, Mantid—Data analysis and visualization package for neutron scattering and μ SR experiments, Nuclear Instruments and Methods in Physics Research Section A: Accelerators, Spectrometers, Detectors and Associated Equipment, 764 (2014) 156-166.

[54] D.L. Abernathy, J.L. Niedziela, M.B.J.E.W.o.C. Stone, Extracting source parameters from beam monitors on a chopper spectrometer, 83 (2015) 03001.

[55] G.L. Squires, Introduction to the theory of thermal neutron scattering, Cambridge university press2012.

[56] B. Wu, T. Iwashita, T. Egami, Atomic Dynamics in Simple Liquid: de Gennes Narrowing Revisited, Physical Review Letters, 120 (2018) 135502.

[57] Y. Shinohara, W. Dmowski, T. Iwashita, D. Ishikawa, A.Q.R. Baron, T. Egami, Local self-motion of water through the Van Hove function, Physical Review E, 102 (2020) 032604.

[58] R. Ashcraft, Z. Wang, D.L. Abernathy, D.G. Quirinale, T. Egami, K.F. Kelton, Experimental determination of the temperature-dependent Van Hove function in a Zr80Pt20 liquid, The Journal of Chemical Physics, 152 (2020) 074506.

[59] H.S. Chen, Glassy metals, Reports on Progress in Physics, 43 (1980) 353.

[60] F. Spaepen, A microscopic mechanism for steady state inhomogeneous flow in metallic glasses, Acta Metallurgica, 25 (1977) 407-415.

[61] A.L. Greer, Metallic Glasses, Science, 267 (1995) 1947-1953.

[62] W.H. Wang, C. Dong, C.H. Shek, Bulk metallic glasses, Materials Science and Engineering: R: Reports, 44 (2004) 45-89.

[63] A.L. Greer, New horizons for glass formation and stability, Nat Mater, 14 (2015) 542-546.

[64] D.C. Hofmann, J.-Y. Suh, A. Wiest, G. Duan, M.-L. Lind, M.D. Demetriou, W.L. Johnson, Designing metallic glass matrix composites with high toughness and tensile ductility, Nature, 451 (2008) 1085.

[65] M. Chen, A brief overview of bulk metallic glasses, NPG Asia Mater, 3 (2011) 82-90.

[66] M.M. Trexler, N.N. Thadhani, Mechanical properties of bulk metallic glasses, Progress in Materials Science, 55 (2010) 759-839.

[67] C.A. Schuh, T.C. Hufnagel, U. Ramamurty, Mechanical behavior of amorphous alloys, Acta Materialia, 55 (2007) 4067-4109.

[68] F. Jiang, Study of mechanical behaviors and structures of bulk metallic glasses with high-energy synchrotron x-ray diffraction, 2011, pp. 1 electronic text (192 p.).

[69] S. Mridha, D.L. Jaeger, H. Singh Arora, R. Banerjee, S. Mukherjee, Evolution of atomic distribution during devitrification of bulk metallic glass investigated by atom probe microscopy, Materials Letters, 158 (2015) 99-103.

[70] N. Mattern, J. Bednarcik, M. Stoica, J. Eckert, Temperature dependence of the short-range order of Cu65Zr35 metallic glass, Intermetallics, 32 (2013) 51-56.

[71] N. Mattern, J. Bednarčik, S. Pauly, G. Wang, J. Das, J. Eckert, Structural evolution of Cu–Zr metallic glasses under tension, Acta Materialia, 57 (2009) 4133-4139.

[72] L.Q. Xing, T.C. Hufnagel, J. Eckert, W. Löser, L. Schultz, Relation between short-range order and crystallization behavior in Zr-based amorphous alloys, Applied Physics Letters, 77 (2000) 1970-1972.

[73] Y. Kawamura, T. Shibata, A. Inoue, T. Masumoto, Deformation behavior of Zr65Al10Ni10Cu15 glassy alloy with wide supercooled liquid region, Applied Physics Letters, 69 (1996) 1208-1210.

[74] U. Köster, D. Zander, R. Janlewing, Quasicrystal Formation, Phase Selection and Crystallization Kinetics in Zr-Cu-Ni-Al Based Metallic Glasses, Materials Science Forum, 386-388 (2002) 89-98.

[75] M. Lee, X. Yang, M. Kramer, D.J.P.M. Sordelet, Glass formation and crystallization in binary Zr–Pt systems, 86 (2006) 443-449.

[76] B.S. Murty, D.H. Ping, M. Ohnuma, K. Hono, Nanoquasicrystalline phase formation in binary Zr–Pd and Zr–Pt alloys, Acta Materialia, 49 (2001) 3453-3462.

[77] D.J. Sordelet, X.Y. Yang, E.A. Rozhkova, M.F. Besser, M.J. Kramer, Oxygen-stabilized glass formation in Zr80Pt20 melt-spun ribbons, Applied Physics Letters, 83 (2003) 69-71.

[78] J. Saida, M. Matsushita, A. Inoue, Structural Change from Amorphous to Nano Icosahedral Quasicrystalline Phase with Quenching Rate in Zr-Pt Binary Alloy, MATERIALS TRANSACTIONS, 42 (2001) 1103-1108.

[79] M. Lee, X. Yang, M. Kramer, D. Sordelet, Glass formation and crystallization in binary Zr–Pt systems, Philosophical Magazine, 86 (2006) 443-449.

[80] X. Qiu, J.W. Thompson, S.J.J.J.o.A.C. Billinge, PDFgetX2: a GUI-driven program to obtain the pair distribution function from X-ray powder diffraction data, 37 (2004) 678-678.

[81] S.J.J.o.c.p. Plimpton, Fast parallel algorithms for short-range molecular dynamics, 117 (1995) 1-19.

[82] A. Hirata, L. Kang, T. Fujita, B. Klumov, K. Matsue, M. Kotani, A. Yavari, M.J.S. Chen, Geometric frustration of icosahedron in metallic glasses, 341 (2013) 376-379.

[83] K.F. Kelton, Kinetic and structural fragility-a correlation between structures and dynamics in metallic liquids and glasses, J Phys-Condens Mat, 29 (2017).

[84] M. Stoica, J. Das, J. Bednarcik, H. Franz, N. Mattern, W.H. Wang, J. Eckert, Strain distribution in Zr64.13Cu15.75Ni10.12Al10 bulk metallic glass investigated by in situ tensile tests under synchrotron radiation, Journal of Applied Physics, 104 (2008) -.

[85] K.F. Kelton, G.W. Lee, A.K. Gangopadhyay, R.W. Hyers, T.J. Rathz, J.R. Rogers, M.B. Robinson, D.S. Robinson, First x-ray scattering studies on electrostatically levitated metallic

liquids: demonstrated influence of local icosahedral order on the nucleation barrier, Phys Rev Lett, 90 (2003) 195504.

[86] J. Saida, M. Matsushita, A. Inoue, Nanoscale icosahedral quasicrystalline phase formation in a rapidly solidified Zr80Pt20 binary alloy, Applied Physics Letters, 77 (2000) 73-75.

[87] K.F. Kelton, Crystallization of liquids and glasses to quasicrystals, Journal of Non-Crystalline Solids, 334–335 (2004) 253-258.

[88] Y.T. Shen, T.H. Kim, A.K. Gangopadhyay, K.F. Kelton, Icosahedral Order, Frustration, and the Glass Transition: Evidence from Time-Dependent Nucleation and Supercooled Liquid Structure Studies, Physical Review Letters, 102 (2009) 057801.

[89] S. Sachdev, D.R. Nelson, Theory of the Structure Factor of Metallic Glasses, Physical Review Letters, 53 (1984) 1947-1950.

[90] T. Faber, J.J.P.M. Ziman, A theory of the electrical properties of liquid metals: III. The resistivity of binary alloys, 11 (1965) 153-173.

Vita

Zengquan Wang was born and grew up in a beautiful village in Shandong, China. He graduated from the Harbin Institute of Technology and obtained the Bachelor's and Master's degree in Materials Science and Engineering in 2011 and 2013, respectively. He joined the department of Materials Science and Engineering at the University of Tennessee, Knoxville as a graduate student in August 2013 to purse the Doctor of Philosophy degree.